Sustainable approaches in removing emerging water pollutants with polyaniline-based porous materials

(ポリアニリン系多孔質材料を用いた水質汚染物質除去の持続的アプローチ)

Paul Kinyanjui Kimani

(ポール　キニャンジュイ　キマニ)

September 2023

Graduate School of Engineering

Gifu University

Sustainable approaches in removing emerging water pollutants with polyaniline-based porous materials

(ポリアニリン系多孔質材料を用いた水質汚染物質除去の持続的アプローチ)

Paul Kinyanjui Kimani

(ポール　キニャンジュイ　キマニ)

A dissertation submitted to the Graduate School of Engineering at Gifu University in partial fulfilment of the requirements for the degree of Doctor of Philosophy in Materials Engineering

September 2023

Declaration

I, Paul Kinyanjui Kimani hereby declare that this dissertation, entitled "*Sustainable Approaches in Removing Emerging Water Pollutants with Polyaniline-Based Porous Materials*," is entirely my original work; prepared at the Graduate School of Engineering, Gifu University under the guidance of Professor Lim Lee Wah. I affirm that it represents my ideas, research, and analysis and that I have properly acknowledged and cited all sources and contributions of others, including but not limited to text, data, and ideas. Any material borrowed from other sources is duly referenced in the bibliography and citation sections.

I further confirm that this dissertation has not been previously submitted for any other academic degree at any institution. To the best of my knowledge and belief, it does not contain any material that has been submitted by another person for academic credit.

Paul Kinyanjui Kimani

Dedication

To my beloved parents: Anthony Kimani and Mary Mukere. Thank you for your unwavering love and support throughout my academic journey. Your encouragement and guidance have been invaluable, and I couldn't have reached this milestone without you.

Acknowledgement

First, I would like to express my sincere gratitude to the Ministry of Education, Culture, Sports, Science and Technology (MEXT) for awarding me the prestigious scholarship that allowed me to pursue my graduate studies. I am also grateful for the academic and research opportunities provided to me by Gifu University, including access to state-of-the-art facilities, resources, and expertise.

I would like to thank my supervisor Prof. Lee Wah Lim for providing me with the opportunity to work in your laboratory and facilitating me in the academic journey. Not to be forgotten are the few months I had a chance to interact and learn from our previous principal investigator, Prof. Toyohide Takeuchi. Additionally, I am grateful to the Professors through whom I had the opportunity to attend their classes and use their equipment and facilities, which greatly enhanced my research. Their expertise and support were invaluable, and I am grateful for their contributions to my work.

To my laboratory colleagues, current and graduated, Ayu, Lia, Haida, Puji, Aya, Thusha, David, Esther, Eri, Ayano, Junna, Hina, Masaya etc., I appreciate the journey and time we have shared as we toil in the never-ending experiments, the joy during lab activities, and the help along the way. Mahmoud,—now Dr with whom we started this journey from Abu Dhabi International Airport—thank you very much for the constant encouragement, help and friendship.

As the old saying goes, "There’s no word yet for old friends who’ve just met," and this sentiment captures my connection with my dear friend, Danielle—mtoto wa geti kali. I want to express my heartfelt gratitude for the unwavering support, shared laughter, and mutual encouragement that sustained us through the challenging period of the COVID era while we pursued our studies.

I would also like to extend my appreciation to a remarkable group of individuals who have been an integral part of this journey. My friends in Japan: Yurika, the Okirias—Emmanuel and Shigeno, Jimmy, Mike, Sam, Sossou, Welma, Samson, Koffi, Robert, David, Dr Sam, Dr Joseph, Dr Paul, Dr Esther, Dr David, Dr Cornelius, and Dr Titus, and those back in my home country, Arnold, Rodger, Peter, Mulama, Sheshe, Jomo, Kevin Mosigisi, Miriam, Njeri, Mary Gitau, Raphael, and John Nderitu, you have all made this academic adventure both memorable and enriching. Your phone calls, spontaneous fun and memorable adventures, and unwavering encouragement have been instrumental in making my journey enjoyable and worthwhile.

To those whose friendships transcended the boundaries of mere companionship, Vethma Withana alias Mini, I want to express my profound gratitude for the meaningful moments we've shared and for your unceasing love and support, even when the odds were not in my favour. Your belief in me has been a constant source of inspiration; the adventures along the way have made my stay in Japan super special— ādaravan.

Finally, I want to thank you for the constant encouragement and phone calls to check up on me. I owe the spirit to give my best to you all: Mum, Dad, Erick, Mercy, Mumbi, Muthoni; my extended family Ndungi, Paul Kibuu, Cornelius, Wanjiru, Alfred, Tony, and the Gitaus.

With love and appreciation,
Paul Kinyanjui Kimani.

Abstract

Emerging contaminants are a new type of water pollutants recently recognized for their potential long-term harm to ecosystems and human health. These pollutants are not regulated, enter the environment in low concentrations undetected, and conventional wastewater treatment plants can't effectively remove them. Lab experiments are conducted yearly to develop water treatment technologies, often using adsorption, a cost-effective method. However, some experimental methods have negative environmental impacts like toxic solvents, high energy use, waste generation, and non-reusable adsorbents, hindering scalability for industry. A dilemma arises in balancing the need for effective water pollution solutions (Sustainable Development Goal 6) with minimizing environmental harm and resource inefficiencies (Sustainable Development Goal 12). Innovative approaches are needed to solve this complex problem.

In this research, we sought sustainable methods to remove these emerging pollutants, especially industrial chemicals and pharmaceutical and personal care products. Guided by green chemistry principles, we selected materials and processes that were biodegradable, non-toxic, cheap, and have a low global warming potential (GWP). We chose adsorption using the polymer, polyaniline, as our desired material because it is a versatile and attractive polymer due to its low cost, ease of modification, and environmental benignity. However, since its linear structure often results in low adsorption capacity, limiting its practical use, we addressed this limitation by oxidising aniline on the surface of an organic single crystal (sodium 1-decansulfonate), resulting in polyaniline with a villi-like morphology that we hypothesized to improve its adsorption performance. Additionally, we composted polyaniline with the biopolymer carboxymethyl cellulose (CMC) to test if it enhanced the adsorption capability. We also composted the villi-structured polyaniline with the oxidized species of CMC, known as dialdehyde carboxymethyl cellulose (DCMC) since some studies had suggested that DCMC performs better in polymer composites. Nevertheless, these studies often failed to investigate the effects of the degree of oxidation in DCMC and to compare the performance of the composites to CMC composites. We attributed this failure to the extensive experiments required for such studies. In this research, we investigated the suitability of villi-structured polyaniline (VSPANI) and its composite with carboxymethyl cellulose (CMC/PANI) as adsorbents for removing bisphenol-A (BPA). We also evaluated the performance of two different types of dialdehyde carboxymethyl cellulose (DCMC) composites, one with 35% aldehyde content (DCMC(A)/PANI) and the other with 77% aldehyde content (DCMC(B)/PANI). To ensure sustainability, we adapted a design of experiment (DOE) approach to study all four adsorbents—a categorical variable—at all factor settings: initial concentration, pH, flow rate, adsorbent amount, and sample volume. We creatively adopted a custom D-optimal screening design to study the cause and effect of the main effects at a higher power. A Definitive Screening Design (DSD) followed to thoroughly investigate the main effects, quadratic effects and quadratic effects of two of the best adsorbents from the custom design and five other factors. The DSD projected to a response surface method (RSM) in three factors: initial concentration, adsorbent amount, and sample volume. The results showed that increasing the aldehyde content of the composites favoured adsorption, but we did not observe any significant difference in performance between VSPANI and DCMC(B)/PANI. The models, successfully validated numerically and graphically, could explain 80% and 99% of the variation when used to predict removal efficiency and adsorption capacity, respectively. VSPANI and DCMC(B)/PANI exhibited potential as adsorbents for BPA removal, achieving 85% removal efficiency and 129 mg/g adsorption capacity.

We further evaluated BPA adsorption onto VSPANI using breakthrough curves to understand the adsorption mechanism. Common models used in simulating breakthrough curves, such as Bohart-Adams, Thomas, Clark, modified dose-response, and Yoon-Nelson, typically assume symmetric S-shaped curves at 50% breakthrough, leading to inaccurate results for asymmetric curves, which are common. We compared log-modified, fractal-like modified, and probability distribution function models for simulating asymmetric breakthrough curves with different degrees of tailing. We varied the bed depth (6 mm, 9 mm, and 12 mm) in a glass microcolumn with 10 mg/L bisphenol-A and villi-structured polyaniline at a constant flow rate of 1 mL/min. Log-Bohart-Adams and fractal-like Clark and Bohart-Adams models fit the curves well, but log-Bohart-Adams performed less effectively with increased tailing. Among the probability distribution curves, normal and Gompertz functions failed to adapt to curve asymmetry due to fixed inflection points. Log-Gompertz function, with floating inflection points, provided a satisfactory fit regardless of symmetry. We recommend using log-Bohart-Adams, fractal-like-Bohart-Adams, or fractal-like-Clark models among the semi-mechanistic models, while log-Gompertz and log-normal models are suitable for accurate breakthrough and saturation time estimation without adsorption-dependent parameters.

To further improve polyaniline's adsorption capacity sustainably and introduce additional photocatalytic functionality, we hypothesized that a metal-organic framework (MOF) would work best as a composite material. MOFs are promising functional materials in environmental remediation applications because of their high crystallinity, large porosity, and high specific surface area. However, powdered materials are challenging to use in environmental remediation: their nano sizes may lead to blocking, synthetic methods involve toxic chemicals and use high energy—global warming potential, and scaling to large-scale industrial applications is a challenge. In a quest to utilise MOFs to remediate emerging micropollutants from water while overcoming the challenges associated with their production, we engineered an environmentally friendly approach for the synthesis of Cu-BDC MOF on the surface of carboxymethyl cellulose microbeads at room temperature, employing solely water-based solvents. By introducing aniline oxidation during the synthetic process, we strategically engineered surface folds on the microbeads, leading to a remarkable increase in their surface area and, consequently, their adsorption capacity. The resulting microbeads contained folds which were patterned with rice-like crystals proved to be Cu-BDC MOF from their XRD patterns. These microbeads (10 mg) were capable of degrading 10 mL of 10 mg/L diclofenac sodium and sulfamethoxazole solutions in the presence of direct sunlight within 4 hrs. Our innovative synthetic method not only yielded high-performance Cu-BDC microbeads but also offered practical advantages by facilitating ease of handling and separation from solution, thus making them an attractive option for industrial applications. Importantly, the complete elimination of toxic solvents in our approach not only aligns with sustainable principles but also reduces potential health risks associated with traditional MOF synthesis practices. This research represented a significant advancement in the field of sustainable materials synthesis, with promising implications for a wide range of applications, most notably in the removal of emerging water pollutants.

In summary, our research shows that seeking sustainable, green, and data-driven methods for removing water pollutants, especially emerging ones, is not just a responsible choice; it is a necessity for safeguarding our environment, health, and the well-being of future generations. By embracing these approaches, we can address the challenges posed by water pollution while building a more resilient and sustainable world.

Table of Contents

Declaration ii

Dedication iii

Acknowledgement iv

Abstract ii

Table of Contents iv

List of Tables viii

List of Figures iii

List of Appendices vi

List of Acronyms vii

Nomenclature viii

Chapter 1: Introduction 1

1.1 Background of the Study 1

1.2 Statement of the problem 4

1.3 Dissertation structure 6

1.4 Research hypothesis 6

1.5 Objectives 7

1.5.1 General objective 7

1.5.2 Specific objectives 7

Chapter 2: Literature Review 8

2.1 Emerging contaminants (ECs) 8

2.1.1 Bisphenol-A 10

2.1.2 Diclofenac 11

2.1.3 Sulfamethoxazole 12

2.2 Remediation techniques for emerging contaminants 13

2.3 Photocatalysis 14

2.4 Adsorption....15
2.4.1 Polyaniline-based adsorbents....15
2.4.2 Adsorption process....17
2.4.2.1 Optimisation techniques....18
2.4.2.2 Batch experiments....19
2.4.2.3 Column experiments....20
2.4.3 Fixed-bed adsorption modelling....20
2.4.3.1 Bohart-Adams model....23
2.4.3.2 Thomas model....23
2.5 Design of experiment (DOE)....24
2.5.1 Screening designs....25
2.5.2 Response surface methodology....27
Chapter 3: Bisphenol-A Adsorption onto Villi-Structured Polyaniline, and its Carboxymethyl and Dialdehyde Carboxymethyl Cellulose Composites: A Customised and Definitive Screening Designed Experiments Approach....29
3.1 Introduction....29
3.2 Methodology....31
3.2.1 Materials....31
3.2.2 Preparation of dialdehyde carboxymethyl cellulose....31
3.2.2.1 Determination of the degree of oxidation of DCMC....31
3.2.3 Preparation of aniline hydrochloride....32
3.2.4 Preparation of villi-structured polyaniline and carboxymethyl cellulose composites....32
3.2.5 Characterisation....33
3.2.6 Fixed-bed adsorption procedure....33
3.2.7 Adsorbate preparation and analytical analysis....33
3.2.8 Design of experiments....34
3.2.8.1 Custom screening design....34

3.2.8.2 Definitive screening design and response surface method 34
3.2.8.3 Model fitting and data validation 35
3.3 Results and Discussion 37
3.3.1 Characterisation 37
3.3.1.1 Synthesis of dialdehyde carboxymethyl cellulose 37
3.3.2 Screening 42
3.3.2.1 Custom main effects screening design 42
3.3.2.2 Type of adsorbent (effect of aldehyde content) 44
3.3.2.3 Effect of initial concentration 45
3.3.2.4 Effect of pH 45
3.3.2.5 Effect of rate 45
3.3.2.6 Effect of the amount of adsorbent 45
3.3.2.7 Definitive screening design 46
3.3.3 Response surface modelling and optimisation 48
3.4 Conclusion 53
Chapter 4: Adsorption of Bisphenol-A onto Villi-Structured Polyaniline: Fixed-Bed Breakthrough Curve Modelling Approach via Log-Modified, Fractal-Like, and Probability Distribution Function Models 55
4.1 Introduction 55
4.2 Methodology 57
4.2.1 Fixed-bed adsorption experiments and column characteristics 57
4.2.2 Mathematical modelling of breakthrough curves 57
4.2.2.1 Bohart-Adams model 57
4.2.2.2 Bed depth service time model 58
4.2.2.3 Thomas model 58
4.2.2.4 Yoon-Nelson model 59
4.2.2.5 Modified dose-response model 59
4.2.2.6 Clark model 60

4.2.2.7 Probability distribution function models 60
4.2.3 Data analyses and nonlinear least square regression 61
4.3 Results and Discussion 63
4.3.1 Experimental breakthrough curves 63
4.3.2 Bohart-Adams model 64
4.3.2.1 Log-modified Bohart Adams model 64
4.3.2.2 Fractal-like Bohart-Adams model 65
4.3.3 Misconceptions 66
4.3.4 Modified dose-response model 70
4.3.5 Clarks model 71
4.3.6 Probability distribution function models 72
4.4 Conclusion 77
Chapter 5: A Trojan Horse Approach for the Synthesis of Scalable Cu-BDC Patterned Polyaniline/Cu-Carboxymethyl Cellulose Microbeads for the Degradation of Diclofenac and Sulfamethoxazole 79
5.1 Introduction 79
5.2 Methodology 80
5.2.1 Materials 80
5.2.2 Synthesis of Cu-BDC/PANI/Cu-CMC microbeads 80
5.2.3 Characterisation 81
5.3 Results and Discussion 82
5.3.1 Characterisation of adsorbents 82
5.3.2 Degradation experiments 89
5.4 Conclusion 91
Chapter 6: Conclusion and Future Perspectives 92
Appendices 95
References 100

List of Tables

Table 3.1: Custom and definitive Screening design factors, coding, levels and responses. ...35
Table 3.2: Oxidation and protonation states for VSPANI and its CMC-based composites. ..41
Table 3.3: Experimental designs evaluation on optimal efficiency and power 43
Table 3.4: Effects summary and optimal settings for individual and combined responses. ...44
Table 3.5: Cohen's d effect size for the type of adsorbent factor.....46
Table 3.6: Definitive screening design effects summary.....47
Table 3.7: Response surface multi-response-model effects summary.....49
Table 3.8: Numerical adequacy checks for the response surface model 49
Table 3.9: Differences between predicted and test-experimental values.....53
Table 3.10: Adsorption capacities of BPA on various adsorbents.....53
Table 4.1: Comparison of parameters and statistical validation for Bohart-Adams, log-Bohart-Adams, and fractal-like Bohart-Adams model 66
Table 4.2: Parameters and statistical validation for simplistic Thomas and Yoon-Nelson models, log-modified Thomas and Yoon-Nelson models, and fractal-like Thomas and Yoon-Nelson models 68
Table 4.3: Parameters obtained from the modified dose-response model 70
Table 4.4: Parameters and statistical analyses for Clarks and fractal-like Clarks model 71
Table 4.5: Probability distribution function parameters and the model's statistical validation 74

List of Figures

Figure 1.1: The 12 principles of green chemistry 3
Figure 1.2: Bar graphs showing publications over the years: (a) polyaniline-based adsorbents; (b) research on adsorption utilising design of experiments (source lens.org) 4
Figure 2.1: Micropollutant subgroups with highest priority levels (RQ >1) in different areas identified through RQ method case studies in the past decade (Yang et al., 2022)..... 9
Figure 2.2: List of micropollutants with relatively high priority based on the RQ method prioritization results reported between 2010 and 2021 (Yang et al., 2022)..... 9
Figure 2.3: Chemical structures of bisphenols (ChemDraw20, Perkin Elmer, MA, USA).... 10
Figure 2.4: Chemical structure of diclofenac (ChemDraw20, Perkin Elmer, MA, USA)..... 11
Figure 2.5: Chemical structure of sulfamethoxazole (ChemDraw20, Perkin Elmer, USA)... 12
Figure 2.6: Photocatalytic mechanism (using TiO2 as an example). 14
Figure 2.7: Various polyaniline structures (ChemDraw20, Perkin Elmer, MA, USA)..... 16
Figure 2.8: The process of adsorption, absorption, and sorption..... 17
Figure 2.9: Setup for batch (a) and column (b) adsorption experiments. 19
Figure 2.10: Mass transfer zone and curve-broadening processes taking place on porous adsorbents (Qili, 2019)..... 21
Figure 2.11: Graphical representation of thr number of experiments and the design space... 25
Figure 2.12: Projection property of fractional factorial designs 26
Figure 2.13: Central composite designs, axial points and the rotatability property. 27
Figure 3.1: Reaction scheme showing polyaniline synthesis on an organic single crystal. ... 33
Figure 3.2: CMC, DCMC(A) and DCMC(B) FTIR-ATR spectra. 37
Figure 3.3: FTIR spectra and size distribution histograms for CMC (a-c), DCMC(A) (d-f), and DCMC(B) (g-i)..... 38
Figure 3.4: FTIR-ATR spectra for VSPANI, CMC/PANI, DCMC(A)/PANI and DCMC(B)/PANI. 39
Figure 3.5: Hydrogen bonding interaction between CMC and PANI backbone. 39
Figure 3.6: SEM micrographs at 100 µm and 5µm scale with particle size histograms embedded with normal distributions for VSPANI: a, e, and j; CMC/PANI: b, f, and k; DCMC/PANI: c, g, and l; and DCMC(B)/PANI: d, h, and m 40
Figure 3.7: UV-Vis absorption spectra for VSPANI and its CMC-based composites 41
Figure 3.8: Molecular structure of PANI showing the polaron lattice, protonation state (x parameter) and the oxidation state (y parameter) where $0 \leq y$ and $x \leq 1.0$ (Wan, 1992) 41

Figure 3.9: XRD patterns of VSPANI, PANI/CMC, PANI/DCMC(A) and PANI/DCMC(B) 42
Figure 3.10: Coloured correlation maps for the main effects and interaction terms 43
Figure 3.11: Prediction profiler for the custom design with desirability maximised. 44
Figure 3.12: Definitive screening results for removal efficiency and log adsorption capacity represented as box plots for the type of adsorbent, and line graphs for the continuous factors with an additional smoother to show curvature for the factors. 47
Figure 3.13: Prediction profilers from definitive screening for removal efficiency and adsorption capacity. 48
Figure 3.14: Adsorption Capacity Box-Cox Transformation 48
Figure 3.15: Box plots showing linear (A), and log-transformed adsorption capacity (B) 48
Figure 3.16: Response surface models' graphical adequacy checks for removal efficiency on the left and adsorption capacity on the right. 51
Figure 3.17: A multi-response prediction profiler for the response surface model with maximised desirability (shaded region shows the prediction range). 52
Figure 3.18: Response surface model surface plots with embedded contour plots showing the factor settings for maximum removal efficiency and adsorption capacity. 52
Figure 4.1: Breakthrough curves from experimental data with the bed depth varied: 6 mm, 9 mm. and 12 mm. 63
Figure 4.2: Breakthrough curves with the bed depth varied and the accompanying residual plots for each: 6mm (A&D), 9 mm (B&E), 13 mm (C&F). 65
Figure 4.3: Bead Depth Service Time (BDST) plots for simplistic, log-modified, and fractal-like modified Bohart-Adams model using 10 mg L^{-1} concentration 66
Figure 4.4: Comparison between Bohart-Adams, Thomas, and Yoon-Nelson models: (i) Simplistic models, (ii) log-modified models, and (iii) fractal-like models.....68
Figure 4.5: "Adam-Boharts" model fit for initial breakthrough data 69
Figure 4.6: Comparison of fitting quality of modified dose-response model and log-Bohart-Adams models with varied bed depth 70
Figure 4.7: Clarks vs fractal-like Clarks model fitted to the adsorption data with varied bed depth.....71
Figure 4.8: Comparison between various probability distribution function models 73
Figure 5.1: Showing paddle-wheel building block for Cu-BDC frameworks in different views. Copper, oxygen, carbon, and hydrogen atoms are shown in blue, red, grey, and white, respectively 79

Figure 5.2: Boxplots with associated normal distribution plots showing the size distribution of the microbeads prepared from acetate (a) and nitrate (n) copper-ion sources.....82
Figure 5.3: Photographs showing the acetate (a) and nitrate (n) copper sources prepared microbeads 82
Figure 5.4: FTIR spectra for CMC and acetate prepared Cu-CMC(a), PANI/Cu-CMC(a), Cu-BDC/Cu-CMC(a), and Cu-BDC/PANI/Cu-BDC(a) microbeads 83
Figure 5.5: FTIR spectra for CMC and nitrate prepared Cu-CMC(n), PANI/Cu-CMC(n), Cu-BDC/Cu-CMC(n), and Cu-BDC/PANI/Cu-BDC(n) microbeads.....84
Figure 5.6: Size distribution of acetate prepared (a) and nitrate (n) prepared Cu-BDC on the surface of PANI/Cu-CMC microbeads.....85
Figure 5.7: Surface SEM micrographs for acetate prepared Cu-CMC (p), PANI/CMC (q), Cu-BDC/CMC (r), and Cu-BDC/PANI/CMC (s) at various magnifications 85
Figure 5.8: Surface SEM micrographs of nitrate prepared Cu-CMC (t_c), PANI/CMC (u_c), Cu-BDC/CMC (v_c), and Cu-BDC/PANI/CMC (w_c) at various magnifications.....86
Figure 5.9: Cross-section SEM micrographs for acetate prepared Cu-CMC (p_c), PANI/CMC (q_c), Cu-BDC/CMC (r_c), and Cu-BDC/PANI/CMC (s_c) at various magnifications 86
Figure 5.10: Cross-section SEM micrographs of nitrate prepared Cu-CMC (t), PANI/CMC (u), Cu-BDC/CMC (v), and Cu-BDC/PANI/CMC (w) at various magnifications.....87
Figure 5.11: XRD diffraction peaks for acetate (a), and nitrate (n) prepared Cu-BDC/PANI/CMC adsorbents cross compared to simulated and prepared Cu-BDC, Cu-CMC, and PANI/CMC.....88
Figure 5.12: Photocatalytic degradation UV/Vis spectra for diclofenac and sulfamethoxazole solutions using the acetate (a) and nitrate (a) prepared microbeads 89
Figure 5.13: Photodegradation pathways of diclofenac showing degradation products (Salgado et al., 2013). 90
Figure 5.14: Photodegradation pathways of sulfamethoxazole showing degradation products (Trovó et al., 2009) 90

List of Appendices

Appendix I: Table showing Custom design matrix table experimental and predicted data ..95

Appendix II: Table showing DSD matrix table with the experimental and predicted data ..96

Appendix III: Figure showing villi-like structures on the surface of VSPANI 96

Appendix IV: Table Showing Analysis of Variance (ANOVA *P=0.05*) for the diameters of the prepared microbeads 97

Appendix V: Table showing a Tukey HSD Post Hoc analysis from ANOVA of the prepared microbeads 97

Appendix VI: Figure showing a close-up of the rice-like crystals on the surface of acetate-prepared microbeads (A) and spherical nanomaterials on nitrate-prepared microbeads (N). 99

Appendix VII: Figure showing urchin-like spherical particles located inside the Cu-BDC/PANI/Cu-CMC(n) microbeads. 99

List of Acronyms

AIC	Akaike information Criterion
ANOVA	Analysis of Variance
AOPs	Advanced Oxidation Processes
BDC	Benzene Dicarboxylate
BIC	Bayesian Information Criterion
CC	Command and Control
CMC	Carboxymethyl Cellulose
CNTs	Carbon Nanotubes
DCMC	Dialdehyde Carboxymethyl Cellulose
DOE	Design of Experiment
DSD	Definitive Screening Design
DWEL	Drinking Water Equivalent Level
ECs	Emerging Contaminants
EDCs	Endocrine Disrupting Compounds
EFSA	European Food Safety Authority
EU	European Union
GAC	Granular Activated Carbon
GWP	Global Warming Potential
HOMO	Highest Occupied Molecular Orbital
HSD	Honest Significant Test
ICSU	International Council for Science
ISSC	International Social Science Council
IUPAC	International Union of Pure and Applied Chemistry
LUMO	Lowest Unoccupied Molecular Orbital
MEC	Measured Environmental Concentration
MIPs	Molecularly Imprinted Polymers
MOF	Metal-Organic Framework
PAC	Powdered Activated Carbon
PANI	Polyaniline
PES	Payment of Ecosystem Services
PNEC	Predicted No-Effect Concentration
PPCPs	Pharmaceutical and Personal Care Products
RMSE	Root Mean Square Error
RQ	Risk Quotient
RSM	Response Surface Methodology
SDG	Sustainable Development Goals
SSE	Sum of Square Error
TDI	Total Daily Intake
UNICEF	United Nations Children's Education Fund
VSPANI	Villi-Structured Polyaniline
WHO	World Health Organization
WWAP	World Water Assessment Program
WWTP	Wastewater Treatment Plant

Nomenclature

Symbol	Description	units
$\boldsymbol{A}$	Clark model constant	(-)
$\boldsymbol{A_0}$	Fractal-like Clark model constant	(-)
$\boldsymbol{a_1}$	Normal function mean	min^{-1}
$\boldsymbol{a_2}$	Log-Normal fitting parameter	(-)
$\boldsymbol{a_3}$	Gompertz fitting parameter	(-)
$\boldsymbol{a_4}$	Log-Gompertz fitting parameter	(-)
$\boldsymbol{a_5}$	$a_5 > 0$ Weibull rate parameter	min^{-1}
$\boldsymbol{b_1}$	Normal function standard deviation	(-)
$\boldsymbol{b_2}$	Log-Normal fitting parameter	(-)
$\boldsymbol{b_3}$	Gompertz fitting parameter	min^{-1}
$\boldsymbol{b_4}$	Log-Gompertz fitting parameter	min^{-1}
$\boldsymbol{b_5}$	$a_5 > 0$ Weibull rate parameter	(-)
$\boldsymbol{a_{Yan}}$	Modified dose-response (Yan) model constant	(-)
$\boldsymbol{C_O}$	Initial concentration of adsorbate (influent)	mg L^{-1}
$\boldsymbol{C_{t(0)}}$	Concentration in flowing liquid phase at time = 0	mg L^{-1}
$\boldsymbol{C}$	Concentration in flowing liquid phase (effluent)	mg L^{-1}
$\boldsymbol{\varepsilon}$	Voidage of packed bed	(-)
$\boldsymbol{f}$	Degrees of freedom	(-)
$\boldsymbol{h}$	Fractal-like component	(-)
$\boldsymbol{k}$	Observed rate constant	(-)
$\boldsymbol{k_0}$	Fractal-like rate constant	(-)
$\boldsymbol{k_{BA}}$	Bohart-Adams rate constant	L min^{-1} mg^{-1}
$\boldsymbol{k_{BA,0}}$	Fractal-like Bohart-Adams rate constant	L min^{-1} $mg^{-(1-h)}$
$\boldsymbol{k_L}$	Langmuir Constant	cm^3g^{-1}
$\boldsymbol{k_T}$	Thomas rate constant	L min^{-1} mg^{-1}
$\boldsymbol{k_{T,0}}$	Fractal-like Thomas rate constant	L min^{-1} $mg^{-(1-h)}$
$\boldsymbol{k_{YN}}$	Yoon-Nelson rate constant	min^{-1}
$\boldsymbol{k_{YN,0}}$	Fractal-like Yoon-Nelson rate constant	$min^{-(1-h)}$
$\boldsymbol{m}$	Mass of adsorbent	g
$\boldsymbol{n}$	Number of data points (observations)	(-)
$\boldsymbol{n_{BA}}$	Number of transfer units	(-)
$\boldsymbol{n_f}$	Freundlich constant	(-)
$\boldsymbol{N_O}$	Sorption capacity per unit volume of fixed-bed	mg L^{-1}
$\boldsymbol{p}$	Number of parameters in the model	(-)
$\boldsymbol{\rho_\rho}$	Particle density	g cm^{-3}
$\boldsymbol{Q}$	Flow rate	L min^{-1}
$\boldsymbol{q_0}$	Adsorption capacity per unit mass of adsorbent	mg g^{-1}
$\boldsymbol{\bar{q}}$	Adsorbed phase concentration averaged over particle volume	mg g^{-1}
$\boldsymbol{q^*}$	Adsorbed phase concentration in equil., with liquid phase	mg g^{-1}
$\boldsymbol{q_s}$	Horizontal part of irreversible equilibrium	mg g^{-1}
$\boldsymbol{r}$	Clark model coefficient	min^{-1}
$\boldsymbol{R^2_{adj}}$	Adjusted coefficient of determination	(-)
$\boldsymbol{S}$	Cross-sectional area of fixed-bed	cm^2
$\boldsymbol{t}$	Time	min
$\boldsymbol{t_{break}}$	Breakthrough time	min

t_{sat}	Saturation time	min
τ	Time for 50% adsorbate breakthrough	min
U	Superficial velocity	cm min^{-1}
V	Volume of solution	cm^3
χ^2	Chi-square coefficient	(-)
y_c	Predicted data	(-)
y_e	Experimental data	(-)
$\overline{y_e}$	Average of experimental data	(-)
Z	Bed depth	cm
Z_0	Critical-bed depth	cm

Chapter 1: Introduction

1.1 Background of the Study

Water is a vital need for every living thing, and yet access to clean water and its availability in some cases is not promised to most people in the world. It is estimated that about 1.1 billion people lack access to clean water leading to about 2.2 billion fatalities yearly from waterborne diseases as this quota of individuals would rather utilise and drink unpotable water than have none (World Health Organization (WHO) & United Nations Children's Education Fund (UNICEF), 2000). About 0.3% of freshwater is available for human and animal use a total of 2.5 % of the freshwater in the world: 96.8% as groundwater, 0.02% from rivers, and 3.18% in lakes (Alsharhan & Rizk, 2020; WWAP (United Nations World Water Assessment Program), 2015). This small quota shrinks every passing year due to population increase and increasing human-based activities that pollute the water exacerbating the available low quantities. Whereas this scenario is worse in developing countries (Kairigo et al., 2020; Kimani et al., 2016), developed countries still face such issues related to water pollution (Parris, 2011).

These water pollutants can be categorised as conventional: fluoride, nitrates, phosphates, and heavy metals among others; emerging pollutants: steroids, hormones, endocrine disrupting compounds (EDCs), pharmaceutical and personal care products (PPCPs), industrial chemicals, surfactants etc., (Ahamad et al., 2020). The lack of requirements to monitor, report, and regulate these emerging pollutants poses a mix of known and unknown threats to human, animal, and aquatic life; hence, the worldwide outcry to address the challenge water pollutants pose to health and provide quality water for all.

The quest for better water quality for a better world led the United Nations in 2015 to coin the sustainable development goals (SDGs) as part of their 2030 agenda for sustainable development. The sixth sustainable development goal (SDG 6) aimed to ensure the availability and sustainable management of water and sanitation for all by the year 2030. It calls for the improvement of water quality, the increase of water-use efficiency, and the protection and restoration of freshwater ecosystems (ICSU & ISSC, 2015). A transformation required to achieve this goal—regarded as transformation number 3 by Sachs *et al*., is to ensure that water pollution is reduced (Sachs et al., 2019).

Globally there have been a variety of efforts to realise transformation 3 required for SDG 6: curbing water pollutants from the source through command and control (CCs) and payment of ecosystem services strategies (PES) (Kimani et al., 2020); removing pollutants from already

polluted water, which is mainly applied in wastewater treatment plants (WWTPs). These WWTPs make use of technologies such as coagulation, filtration, adsorption, UV treatment, and disinfection using chlorine-based compounds (Crini & Lichtfouse, 2019).

Since conventional WWTPs were not adapted to dealing with emerging pollutants, on a lab scale, research is conducted yearly in the improvement of already existing technology or in the creation of better technology to address the issue of water pollution—especially from these emerging pollutants. These methods include membrane-filtration (Ahmed et al., 2022), utilising micro-algae (Li et al., 2019), catalysis and ozonation (Nguyen et al., 2022; Wang & Chen, 2020), and adsorption (Ali, 2012). Adsorption remains the universal, more cost-friendly, fast, simple, and economically effective process of water treatment (Ali & Gupta, 2007a; Singh et al., 2018). Yearly, there are many studies conducted on the syntheses of adsorbents that are more efficient compared to the current commercial adsorbents in use.

However, as these studies are being conducted and new adsorbent materials churned yearly, we must ask ourselves whether our experimentation methods are leading to more harm than good. Excessively large experiments are conducted to test various adsorbents using the pollutants as the model analytes—which is inevitable. Some experimentation strategies utilise toxic solvents, require high energy costs to produce, generate large wastes, and the adsorbents prepared are usually not reusable; it is no wonder that once published it becomes hard to scale these materials for industrial use—they just die at the lab-scale phase. As discussed by Huesemann, the conservation of mass principle, second law of thermodynamics, and Barry's Commoner's second law of Ecology: "*Everything Must Go Somewhere*", serve to tell us that the negative environmental impact of these experiments can never be zero (Commoner, 1972; Huesemann, 2001). However, we can, we must, and we should try to reduce the negative impact of our solutions to water pollution as the current trends only perpetuate the scientists' stereotype as put by George Bernard Shaw: "*science never solves a problem without creating ten more*."

Sustainable goal number 12 (SDG12) calls for sustainable consumption and production patterns. One of the questions it raises is what cost-effective and toxic-chemical-free methods can be used to prevent and reduce pollution in relation to production and consumption activities (ICSU & ISSC, 2015). Clearly, there exists a link between finding solutions to achieve SDG6 while observing SDG12: by promoting resource efficiency, reducing waste generation, and minimising the negative environmental impacts of our experimentation methods. If not addressed, our quest to find better adsorbents as solutions to achieving SDG6, the solutions

would be adding to environmental degradation and climate change. Fonseca *et al.,* outline strong significant correlations between SDG6 and SDG12 (Fonseca et al., 2020) suggesting that the trade-offs while trying to achieve the two should be minimised and synergies promoted.

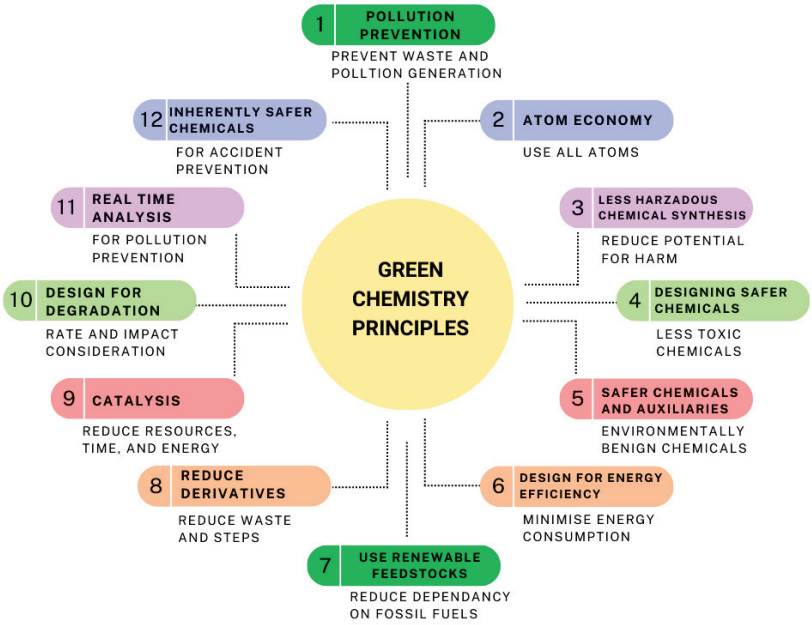

Figure 1.1: The 12 principles of green chemistry

Green chemistry can guide the approach used to finding solutions to achieve SDG6 while keeping SDG12 in mind: it promotes the design of environmentally benign products and processes guided by twelve principles summarised in Figure 1.1. In summary, the design aspect of green chemistry carries a larger load because it is a human intervention and cannot be accidental (Anastas & Eghbali, 2009). Therefore, adsorbents used for the removal of water pollutants should be synthesised, developed, and applied using processes and reagents that reduce or eliminate the use of hazardous substances, use renewable feedstocks, and through energy-efficient processes. Statistical approaches are encouraged in designing for a green chemistry future (Zimmerman et al., 2020) which makes design of experiment (DOE) a method of interest regarding sustainability in experiments related to water pollutants removal using adsorbents.

Design of experiment (DOE) is a useful statistical tool in developing chemical products and processes that align with green chemistry principles. Though DOE faced obstacles to put to practice two decades ago as argued and outlined by Lendrem *et al*., (Lendrem et al., 2001), in the recent decade there has been immense growth in the use of DOE in scientific research—resulting from the tremendous developments in software in the last two decades (Durakovic, 2017).

The number of publications related to the use of DOE in finding adsorbents for removing water pollutants has shown a significant increase over the last decade (Figure 1.2b). A keen look at most of these studies shows the use of classical DOE techniques, which when dealing with multiple adsorbents (categorical variable) and a large number of factors, can lead to large unsustainable experiments. Definitive screening designs (DSDs), which are a new class three-level optimal designs fashioned in 2013, creatively combine screening and optimisation resulting in few experiments for a multiple number of factors (Jones & Nachtsheim, 2013). However, DSD is still incapable of handling multiple categorical factors—such as type of adsorbent in this case—without trading off with reduced accuracy; also, the design is limited by only two levels per factor during the initial design meaning that it can only handle two adsorbents for one particular study.

Polyaniline is a polymeric organic material with the potential for use as a green material: it is easily prepared, versatile, environmentally stable, and cheap material that has been used as an adsorbent in removing heavy metals, emerging pollutants, dyes, among many other water pollutants (Samadi et al., 2021a). The interest in the use of polyaniline as an adsorbent has attracted attention over the last decade as shown by the trend in publications over the years (Fig. 1.2a). Polyaniline by itself is a linear polymer with a limited low specific surface area requiring modification to improve its potential as an adsorbent.

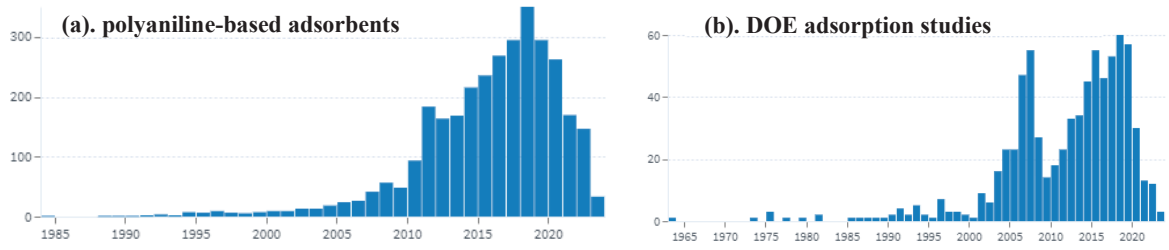

Figure 1.2: Bar graphs showing publications over the years: (a) polyaniline-based adsorbents; (b) research on adsorption utilising design of experiments (source lens.org)

1.2 Statement of the problem

Water is a fundamental necessity for all living organisms, yet access to clean water remains a challenge for a significant portion of the global population. Despite efforts to address accessibility issues, water pollution exacerbates the available water sources and continues to threaten human, animal, and aquatic life worldwide. Increasing population growth has led to

an increase in human and industrial activities that contribute to an additional category of water pollutants: emerging pollutants. Most of the pollutants in this class lack regulations, are introduced to the environment in low concentrations bypassing detection, and design of conventional wastewater treatment plants are not suited to removing these emerging pollutants.

Lab-scale research is conducted annually to develop new technologies and adsorbents for water treatment, with adsorption being a widely used and cost-effective process. However, many experimentation methods utilised in these studies may have negative environmental impacts, such as the use of toxic solvents, high energy requirements, generation of large wastes, and non-reusability of adsorbents, which may hinder their scalability for industrial use. Furthermore, the need to achieve Sustainable Development Goal 6 (SDG 6) of ensuring the availability and sustainable management of water and sanitation for all by 2030, while also adhering to SDG 12 of promoting sustainable consumption and production patterns, presents a challenging dilemma. Balancing the need for effective water pollution solutions with the imperative to minimise environmental harm and resource inefficiencies is a complex problem that requires innovative approaches.

Design of experiment (DOE) is a valuable statistical tool in developing chemical products and processes aligned with green chemistry sustainable principles. Despite obstacles faced in the past, recent advancements in software have led to significant growth in the use of DOE in scientific research. However, classical DOE techniques may lead to unsustainable experiments when dealing with multiple categorical factors, such as different adsorbents for removing water pollutants. Definitive screening designs (DSDs) have shown promise in reducing the number of experiments, but they have limitations in handling multiple categorical factors and may trade off accuracy. Polyaniline, a polymeric organic material with potential for use as a green adsorbent, has gained attention in recent years due to its versatility and low cost. However, polyaniline's limited specific surface area requires modification to enhance its adsorption potential.

Therefore, the problem statement for this thesis research is to develop cost-effective and environmentally sustainable methods for removing emerging pollutants using polyaniline-based adsorbents, while also promoting resource efficiency and waste reduction in alignment with SDG 6 and SDG 12. This research aims to address the limitations of current experimentation methods and propose solutions that minimise negative environmental impacts, thereby contributing to the advancement of sustainable water management practices at a global scale.

1.3 Dissertation structure

This study is divided into six chapters: Chapter One introduces the background of this research, states the problem, and outlines the objectives; Chapter Two reviews the literature and describes in detail the concepts of emerging water contaminants, polyaniline-based adsorbents used in the removal of emerging contaminants, fixed-bed modelling, and design of experiment approaches in adsorption studies.

Chapter Three describes the syntheses of villi-structured polyaniline and its carboxymethyl and dialdehyde carboxymethyl cellulose composites used for the removal of bisphenol-A from water. This chapter investigates whether villi-structures improve the adsorption capacity of polyaniline, and whether composting villi-structured polyaniline with carboxymethyl cellulose aids in improving its adsorption capacity; also, the influence of the aldehyde content when using dialdehyde carboxymethyl cellulose rather than carboxymethyl cellulose. Clearly, studying all these adsorbents at each of the adsorption-dependent factors would require a sustainable method and so in this chapter design of the experiment—data-driven model—is modified to study the four adsorbents, screen for active factors influencing adsorption, optimise the active factors and generate predictive models for the adsorption process.

Chapter Four investigates mechanism-driven models in the fixed-bed adsorption of bisphenol-A onto villi-structured polyaniline. Classical logistic models such as the Bohart-Adams model, their modified models, and probability distribution function models are investigated to provide insight into the most efficient models to use for asymmetrical breakthrough curve modelling.

Chapter Five studies a sustainable way through which the adsorption capacity of polyaniline can be improved using aqueous prepared copper-metal-organic-framework (Cu-BDC) infused onto carboxymethyl cellulose microbeads for ease of recycling.

Chapter Six concludes the study, provides limitations for the current work, and suggests recommendations for future work.

1.4 Research hypothesis

Implementing Design of Experiments (DOE) through Definitive Screening Designs (DSDs) in the optimisation of adsorbents for water pollution removal, modifying fixed-bed models to better suit experimental data, and using a trojan approach to grow copper-based MOF crystals onto polyaniline/carboxymethyl cellulose microbeads, will result in reduced experimental efforts, improved accuracy, and increased sustainability approaches to removing emerging water contaminants.

1.5 Objectives

1.5.1 General objective

To improve experimentation, data acquisition, data analysis, and synthesis methods in the removal of emerging water pollutants from an aquatic source using polyaniline-based adsorbents modified using renewable feedstock, and water-based solvents.

1.5.2 Specific objectives

1. To synthesise and characterise villi-structured polyaniline, its dialdehyde and carboxymethyl cellulose composites.
2. To study the removal of bisphenol-A from an aquatic source using villi-structured polyaniline and the effect of dialdehyde content in using its carboxymethyl cellulose composites.
3. To create a method through which design of experiment can screen multiple adsorbents (categorical variables) at all other factor settings in as few experiments as possible.
4. To conduct a fixed-bed breakthrough study for the removal of bisphenol-A onto villi-structured polyaniline.
5. To compare simplistic fixed models, log-modified models, fractal-like models, and probability distribution function models in the fitting of asymmetrical breakthrough curves.
6. To use a trojan-horse approach in infusing polyaniline with aqua-prepared Cu-BDC MOF supported on carboxymethyl cellulose microbeads complexed in a copper solution.
7. To study the photocatalytic degradation of diclofenac and sulfamethoxazole solutions with the use of Cu-BDC/PANI/CMC microbeads under direct sunlight.

Chapter 2: Literature Review

2.1 Emerging contaminants (ECs)

In contrast to conventional water contaminants that are well known such as heavy metals, nitrates, phosphates, and chlorides among many others, emerging contaminants (ECs) represent a new breed of pollutants which occur in low concentration bypassing detection; hence, their regulations are yet to be formulated for their presence to be monitored in our water supply and wastewater, and publicly reported (Morin-Crini et al., 2022). These ECs include pharmaceutical and personal care products (PPCPs), endocrine disrupting compounds (EDCs), hormones, perfluorinated compounds, artificial sweeteners, licit and illicit drugs, sunscreens and UV filters, dioxanes, siloxanes, pesticides, benzotriazoles among many others captured in the following reviews (T. H. Y. Lee et al., 2022; Morin-Crini et al., 2022; Richardson, 2010).

Emerging contaminants occur in surface water, drinking water, and wastewater in a non-discriminative phenomenon irrespective of a nation's developed status. However, occurrence is not directly related to risk meaning that not all ECs are considered a threat. A contaminant needs to have a high occurrence and high toxicity to raise concern as described by the risk quotient's (RQ) criteria defined by Eqs (2.1) and (2.2) where MEC is the measured environmental concentration, PNEC is the predicted no-effect concentration, and DWEL is the drinking water equivalent level (Tang et al., 2019; Yang et al., 2022). ECs with RQ values $\leq$ 0.1 indicate low-level risk; the values between 0.1 and 1 indicate moderate risk, while ECs with RQ values higher than 1 are a high-risk potential and much attention should be towards their removal (Hernando et al., 2006; Z. Yan et al., 2018). Figure 2.1 shows the global occurrence of high-risk (RQ>1) emerging contaminants summarised in Figure 2.2 that require intervention with the highest priority.

$$RQ = \frac{MEC}{PNEC} \tag{2.1}$$

$$RQ = \frac{MEC}{DWEL} \tag{2.2}$$

Though there exist gaps in proper understanding and mapping of the fate, behaviours, and health effects of these micropollutants, some of the health and toxic effects have been studied (Gogoi et al., 2018; Saquib et al., 2021): antibiotic resistance from pharmaceuticals such as penicillin and sulphonamides (Daughton, 2001); roxithromycin, tylosin, and clarithromycin inhibiting algae growth; caffeine disrupting the endocrine system of goldfish; cancerous, estrogenic, and hormonal effects from bisphenol-A exposure.

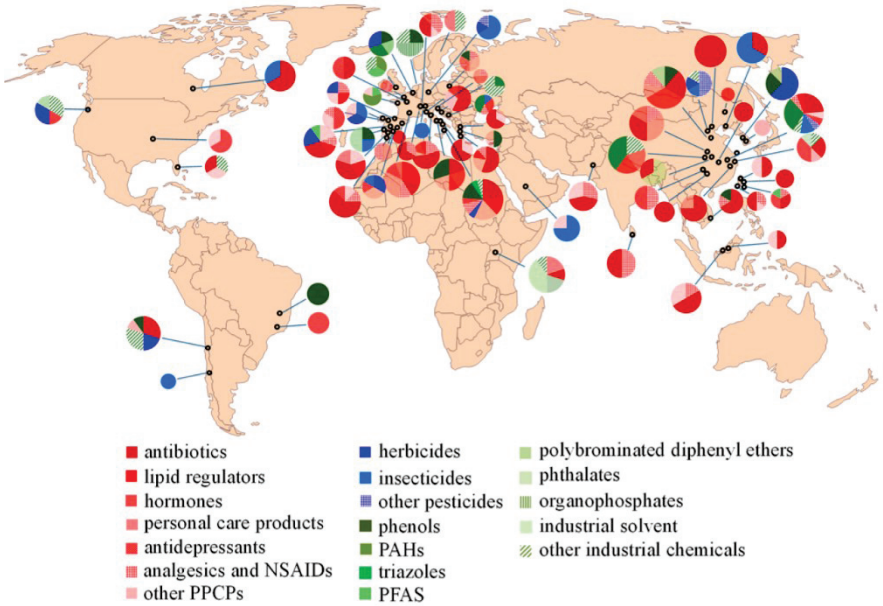

Figure 2.1: Micropollutant subgroups with highest priority levels (RQ >1) in different areas identified through RQ method case studies in the past decade (Yang et al., 2022).

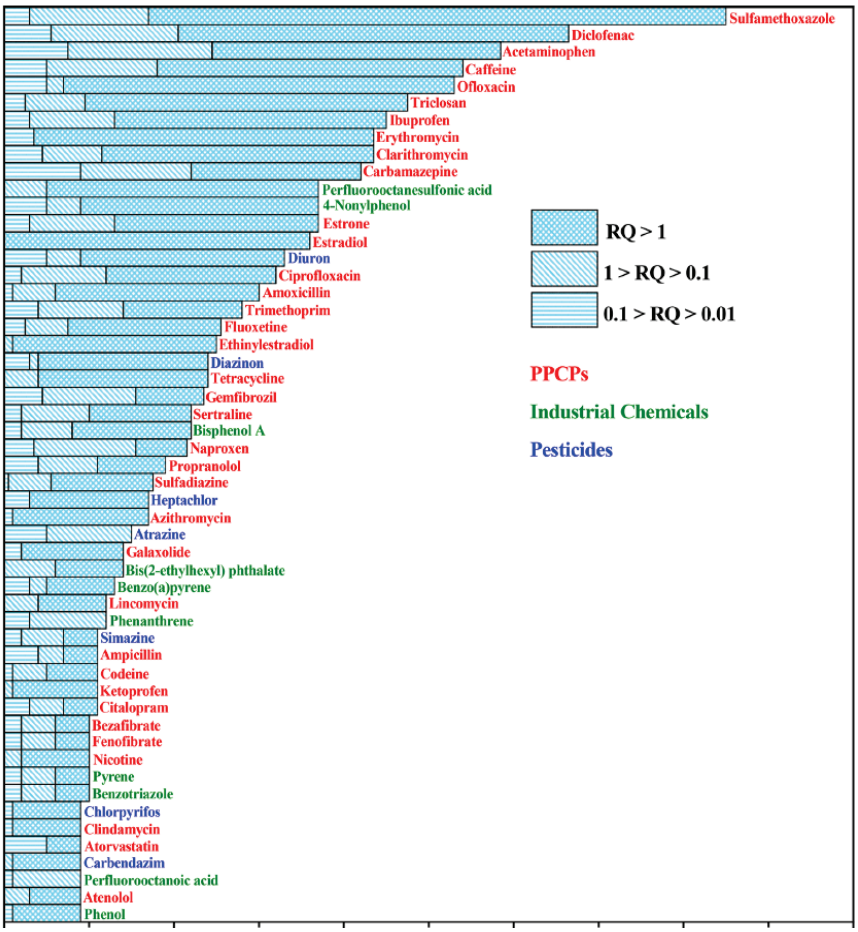

Figure 2.2: List of micropollutants with relatively high priority based on the RQ method prioritization results reported between 2010 and 2021 (Yang et al., 2022).

It should be straightforward that there needs to be more comprehensive monitoring of emerging contaminants in all environmental components (Petrie et al., 2015), but these ECs occur in low concentrations to be detected, and current technology in wastewater treatment plants are inefficient in eliminating ECs (Bolong et al., 2009; Gomes et al., 2020). In addition to improving detection methods, means of removing these contaminants should be of the highest priority.

2.1.1 Bisphenol-A

2,2-bis(4-hydroxyphenyl)propane, commonly known as bisphenol-A—from a group of bisphenols (Figure 2.3) B, C, F, S, and AF—is a chemical compound commonly used in the production of polycarbonate and epoxy resin plastics, including water bottles, food containers, and other consumer goods (Kim et al., 2019). However, BPA has raised significant health concerns due to its potential to leach into water sources and contaminate drinking water.

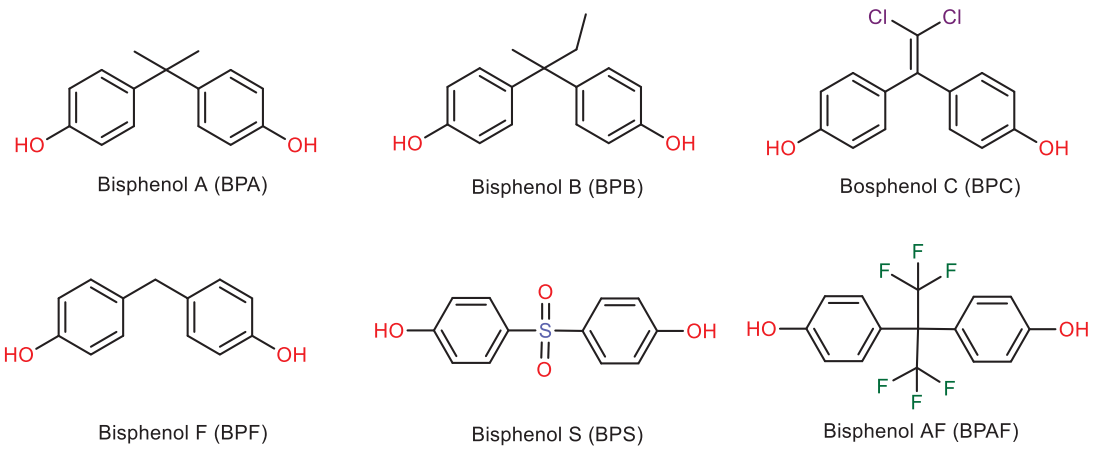

Figure 2.3: Chemical structures of bisphenols (ChemDraw20, Perkin Elmer, MA, USA).

Research has shown that BPA acts as an endocrine disruptor, can mimic the effects of estrogen in the body, and has been linked to a wide range of health issues (Zaborowska et al., 2021). Other studies have associated BPA exposure with hormonal imbalances, reproductive problems, developmental delays, increased risk of certain cancers, and adverse effects on the cardiovascular system and metabolism (Gao et al., 2015). Vulnerable populations such as pregnant women, infants, and children may be particularly susceptible to the health risks associated with BPA exposure.

Health experts and environmental organisations advocate for stricter regulations on the use of BPA in consumer products to protect public health and reduce the potential for BPA contamination in water sources. European Union (EU) and the America Food and Drug Administration have set certain regulations such as restricting its use in baby bottles and infant

food packaging and recently, the European Food Safety Authority (EFSA) has lowered the tolerable daily intake (TDI) for BPA in foodstuffs to 0.04 ng/kg body weight per day based on recent evidence on BPA toxicity (Hahladakis et al., 2023).

Despite regulations, BPA is still highly present in lakes, wastewater, and river water from countries such as Japan, S. Korea, India, China etc. (J. Liu et al., 2021; Yamazaki et al., 2015). Biological degradation and adsorption are preferred methods to remove BPA from water (Tarafdar et al., 2022) because oxidation and chlorination methods form oxidised and chlorinated derivatives (ClxBPA) which pose the same toxicity if not worse (Plattard et al., 2021).

2.1.2 Diclofenac

Diclofenac (Figure 2.4) with the IUPAC name ((2-[(2,6-dichlorophenyl)amino]benzeneacetic acid)) is a nonsteroidal anti-inflammatory drug (NSAID) that is commonly used to reduce pain, inflammation, and fever. It belongs to a class of medications known as NSAIDs, and it is available both as a prescription and over-the-counter medication in various forms, including tablets, capsules, gels, and creams. Diclofenac works by inhibiting the production of prostaglandins, which are substances in the body that cause inflammation and pain(Kantor, 1986; Sallmann, 1986).

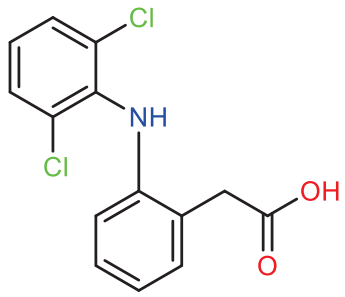

Figure 2.4: Chemical structure of diclofenac (ChemDraw20, Perkin Elmer, MA, USA).

The issue with diclofenac as an emerging pollutant primarily arises from its presence in the environment and its potential negative effects on aquatic ecosystems (Vieno & Sillanpää, 2014). When people take diclofenac for pain relief or other medical reasons, the drug can enter their bodies and be excreted in its original form or as metabolites. These pharmaceutical residues can then find their way into wastewater treatment plants (Buser et al., 1998; Lonappan et al., 2016).

Diclofenac is a concern because it is persistent: relatively stable and does not easily break down in the environment; toxicity to aquatic life and birds by disrupting the endocrine systems of

fish leading to reproductive and developmental abnormalities in these species; bioaccumulates: it accumulates in the tissues of aquatic organisms over time, leading to potential biomagnification in food chains (Acuña et al., 2015).

Diclofenac has been detected in the environment in various countries, primarily due to its presence in wastewater and its potential harm to wildlife. In India and Nepal in the early 2000s, diclofenac was linked to significant declines in vulture populations, leading to bans on its veterinary use in these countries (Galligan et al., 2021; Green et al., 2004). Despite these bans, ongoing monitoring efforts have revealed its presence in the environment in regions like Europe (Sathishkumar et al., 2020), Africa (Waleng & Nomngongo, 2022), and South America (Roveri et al., 2022) raising concerns about its impact on aquatic ecosystems. Some European countries have implemented regulatory measures to restrict diclofenac's use and improve its management in wastewater treatment systems. Monitoring and regulatory actions continue worldwide to address diclofenac as an emerging environmental pollutant.

2.1.3 Sulfamethoxazole

Sulfamethoxazole (SMX, Figure 2.5) is an antibiotic medication launched first in combination with trimethoprim in 1969 by F. Hoffman-La Roche. It is commonly used to treat bacterial infections in humans. It belongs to a class of drugs known as sulphonamides, and it works by inhibiting the growth of bacteria by interfering with the synthesis of folic acid, which is essential for the production of DNA and RNA in bacteria (Straub et al., 2016).

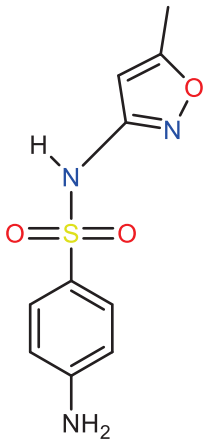

Figure 2.5: Chemical structure of sulfamethoxazole (ChemDraw20, Perkin Elmer, USA).

Sulfamethoxazole has emerged as a significant environmental pollutant due to its widespread presence in ecosystems. This pollutant enters the environment through various pathways, including human and animal excretion, wastewater treatment plant effluents, and improper pharmaceutical disposal. Its chemical stability allows it to persist in the environment, posing a

threat to aquatic ecosystems. SMX can disrupt aquatic life, including algae, phytoplankton, and aquatic plants, which can cascade through the food web, leading to changes in species composition and reduced biodiversity (Larcher & Yargeau, 2012). Furthermore, SMX's presence in the environment contributes to antibiotic resistance, a pressing public health concern, as bacteria can develop resistance, potentially rendering antibiotics less effective in treating infections. While levels in drinking water are typically low, long-term exposure to trace amounts of SMX raises potential health risks, emphasizing the need for stricter regulations, improved wastewater treatment, responsible medication disposal practices, and public awareness to address this emerging pollutant's impact on ecosystems and public health (Sanusi et al., 2023; Straub et al., 2016).

2.2 Remediation techniques for emerging contaminants

Remediation strategies for emerging contaminants can be grouped into natural attenuation, conventional, and advanced treatment processes. Natural attenuation processes such as dilution, volatilisation, biodegradation, photolysis, and sorption are simple and cheap, but slow and inefficient (Barbosa et al., 2016).

Conventional treatments such as membrane filtration and adsorption onto powdered or granular activated carbon adsorption (PAC and GAC respectively) are more effective than natural attenuation in removing ECs. Membrane filtration requires high energy to operate, and it is challenging to dispose the concentrate by-product (Rizzo et al., 2019). Activated carbon is less toxic, does not lead to ozone depletion, and is renewable; however, even though it requires less energy to operate, the main concern is its high impact on global warming potential (GWP) in producing and regenerating it after use (Pesqueira et al., 2020).

Advanced treatment technologies include advanced oxidation processes (AOPs), constructed wetlands, bioelectrical systems, and enzymatic treatment etc. (Rout et al., 2021). Advanced oxidation processes rely on producing hydroxy radical ($\cdot OH$) or sulphate radical ($SO_4^{\cdot -}$) to degrade and remove water contaminants. The hydroxyl radicals are most common and reactive in water treatment and are generated from ozone treatment, UV/H_2O_2 treatment using oxidants or catalysts,— TiO_2 is common—photocatalysts, electrochemical oxidation, and Fenton process using metals that are capable of activating (H_2O_2) where iron (Fe^{2+}) is the most common (Deng & Zhao, 2015; Madivoli et al., 2020). Though highly promising, some of these technologies such as bioelectrical and enzyme bioreactors are still new and face numerous challenges such as stability and reusability (Al-Maqdi et al., 2021). Collectively, these advanced technologies are expensive, require complex equipment, and require high energy to

produce and operate; in addition, AOPs especially ozonation, catalysis, and photocatalysis result in the formation of unknown by-products that may be more toxic, requiring additional steps to remove them (M'Arimi et al., 2020; Wilkinson et al., 2017).

2.3 Photocatalysis

Photocatalysis as an AOP in the treatment of emerging pollutants pivots on the utilisation of semiconductor photocatalysts, typically metal oxides like titanium dioxide (TiO_2) and zinc oxide (ZnO), which possess the ability to absorb photons and generate electron-hole pairs when exposed to solar or artificial light (Sambaza et al., 2020; Zheng et al., 2022). These generated electron-hole pairs can subsequently initiate catalytic reactions on the surface of the photocatalyst (Figure 2.6), leading to the degradation or transformation of a wide range of organic and inorganic pollutants.

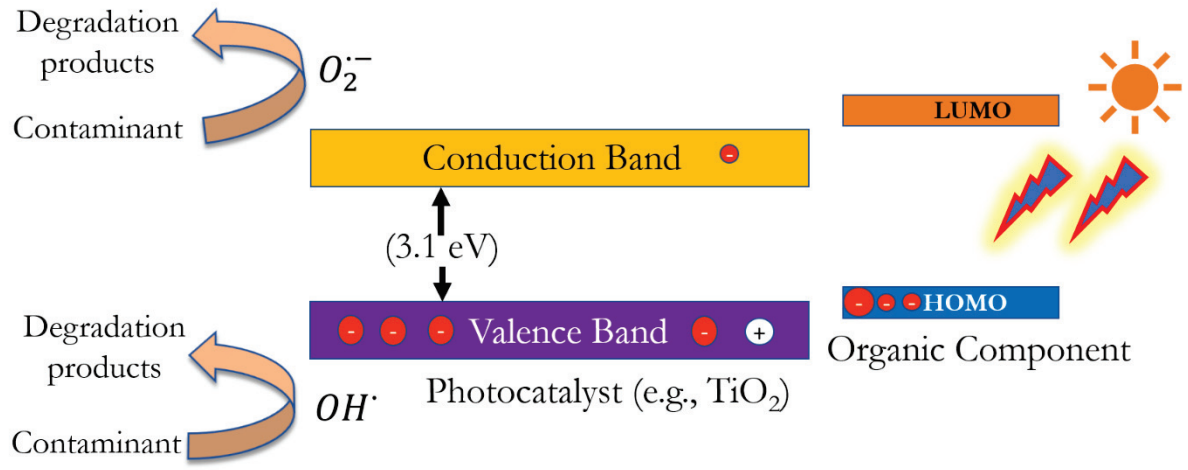

Figure 2.6: Photocatalytic mechanism (using TiO2 as an example).
HOMO = Highest Occupied Molecular Orbital) and LUMO = Lowest Unoccupied Molecular Orbital)

Photocatalysis has several advantages, including its environmental friendliness as it relies on renewable solar energy, its effectiveness in breaking down a wide range of pollutants, and the potential to mineralise them into less harmful end products. However, there are limitations, such as the need for specific photocatalysts and light sources, potential catalyst deactivation due to fouling or poisoning, and the generation of byproducts that may require further treatment (Gokulakrishnan et al., 2021). Moreover, the efficiency of the process can be influenced by factors like the concentration of pollutants, pH, and the presence of other substances in the environment, which may affect its overall applicability and cost-effectiveness (Ahmed et al., 2021).

2.4 Adsorption

As covered in section 2.4, adsorption—especially using activated carbon—remains the most efficient, affordable, flexible to modification, and simplest conventional method through which ECs can be remediated from water (Rathi & Kumar, 2021). Activated carbon is the go-to adsorbent for WWTPs, but it is limited by the high production and regeneration cost to be used on a large scale. Other effective adsorbents that can be used include biochar, carbon nanotubes (CNTs), clay minerals, zeolites, pumice, graphene oxide, metal oxides, molecularly imprinted polymers (MIPs), etc. whose advantages and disadvantages have been reviewed extensively (Basheer, 2018; Rodriguez-Narvaez et al., 2017; Sophia A. & Lima, 2018; Yadav, Bagotia, et al., 2021). The disadvantages of these adsorbents are the high production cost, recyclability issues, and stability, and most are non-biodegradable.

2.4.1 Polyaniline-based adsorbents

Polyaniline—commonly abbreviated as PANI or PAni—is a conductive homopolymer whose history can be traced to a report of a "blue substance" when Dr Henry Letheby electro-lysed aniline sulphate in 1862 (Rasmussen, 2018). Polyaniline is commonly prepared by oxidising aniline into various polymeric structures (Figure 2.7) each possessing a different colour and characteristics.

The molecular structure of polyaniline contains either benzenoid (B), quinonoid (Q) or both states in different proportions (Figure 2.7). The redox state of polyaniline is dependent on the ratio of benzenoid to quinonoid state, i.e., m:n, which should be ideally 1:1 for the emeraldine base, but this can be tuned depending on synthesis and extent of doping (Bhandari, 2018).

Doping and dedoping yield different structures with varying electrochemical properties: doping in acidic media improves while dedoping with bases deteriorates the electroactive behaviour. These dopants linger near the polymer backbone and do not chemically react with the polyaniline chain or form any bonds. They lower the bandgap of polyaniline enhancing its electrochemical properties and they can be categorised into two: p-type dopants donate positive charge (holes) to the polyaniline chain; n-type which are electron-rich agents such as I_2, Br_2 etc., including organic and inorganic acids (Bhandari, 2018).

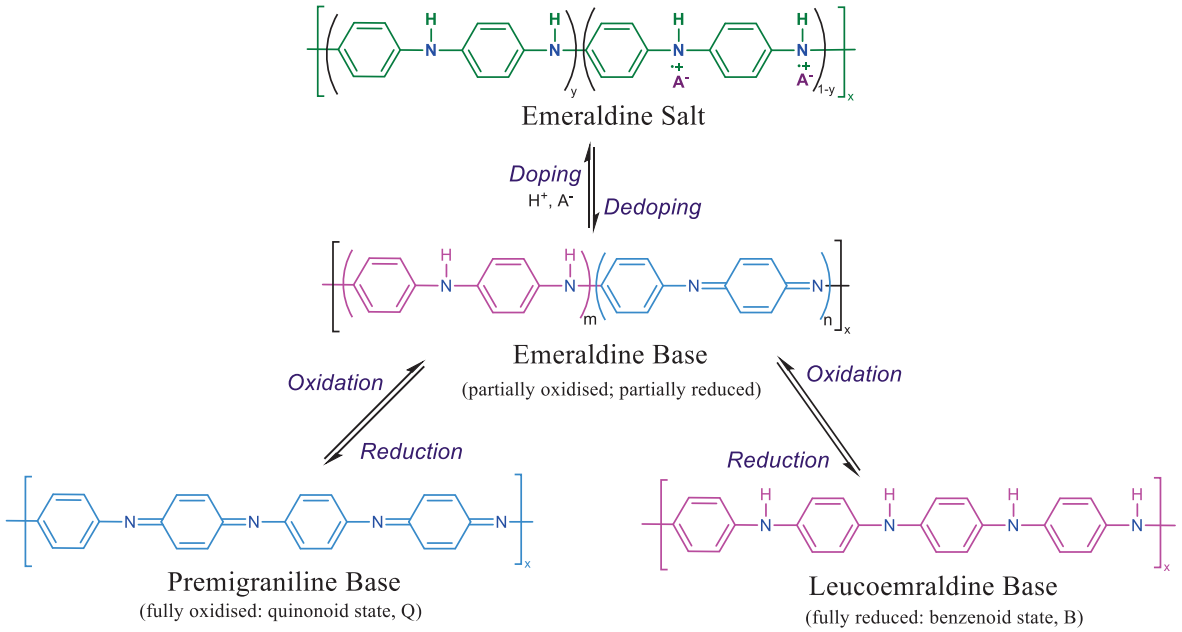

Figure 2.7: Various polyaniline structures (ChemDraw20, Perkin Elmer, MA, USA)

(A^- is an arbitrary anion; m and n are the ratios of quinonoid and benzenoid state; y is the oxidation state)

Polyaniline-based adsorbents are effective due to the unique properties they possess over other adsorbents: they have excellent environmental stability; the cost of the monomer and oxidants is cheap; the synthetic procedure has a low global warming potential (GWP), requires no toxic chemicals, and is simple; the properties of the adsorbent can be easily tuned—hence the famous "*there are as many polyanilines as the number of people who make them*"—depending on the synthetic procedure, dopant, or additive used (Samadi et al., 2021b). They have been successfully used in removing heavy metals from water (Eskandari et al., 2020), dyes (Nasar & Mashkoor, 2019), and emerging pollutants (Ekande & Kumar, 2023; Park & Jhung, 2021) mainly through adsorption and in some instances to enhance catalytic properties metal nanocomposites for degrading the pollutants through photocatalysis (Yadav, Kumar, et al., 2021).

Polyaniline being a linear polymer has a low specific surface area varying between $15 - and\ 42\ S_{BET}(m^2/g)$ as determined by Cai et al., by changing the oxidant to monomer ratio, time, and temperature (Cai et al., 2018). As an adsorbent, this is not desirable and hence polyaniline adsorbents are mostly synthesised as a copolymer, composted with other organic or inorganic material, crosslinked with other polymers, or applied as a core-shell with metal oxides or metal-organic frameworks. Composting polyaniline with biopolymers such as cellulose, carboxymethyl cellulose, starch, cyclodextrin, glucose, chitosan etc., is more

desirable to keep the green and sustainable attractiveness of polyaniline as an adsorbent (Anisimov et al., 2021).

2.4.2 Adsorption process

Adsorption is defined as the increase of concentration of a component at the surface of the interface between two phases. The term 'adsorption' was first used by McBain in 1909 to describe the uptake of hydrogen by carbon (McBain, 1909). The term 'sorption' is easily confused with adsorption, but it refers to both adsorption and absorption (Figure 2.8). Adsorbate is the component in the bulk phase that adheres to the solid or liquid surface of an adsorbent. The adsorption process occurs when adsorbates in a liquid or gas phase interact with adsorbents in solid or liquid phase interact with one another physically (physisorption), which is reversible or chemically (chemisorption), which is stronger, specific but often irreversible (Ali & Gupta, 2007b). The adsorbents should ideally have a high specific surface area and a strong affinity towards the adsorbate of interest to be effective.

The initial stage of the adsorption process involves the adsorbate molecules transferring from the bulk phase (mass transfer) to the surface of the adsorbent through diffusion or convection. At the adsorbent surface, the adsorbate interacts with the functional groups through various forces such as hydrogen bonding, electrostatic interactions, chemical, π-π stacking, or Van der Waals forces (Kecili & Hussain, 2018). The adsorbate accumulates on the surface of the adsorbent forming a monolayer or multilayer depending on the adsorbent and adsorbate characteristics; chemisorption can only occur through a monolayer (Dąbrowski, 2001).

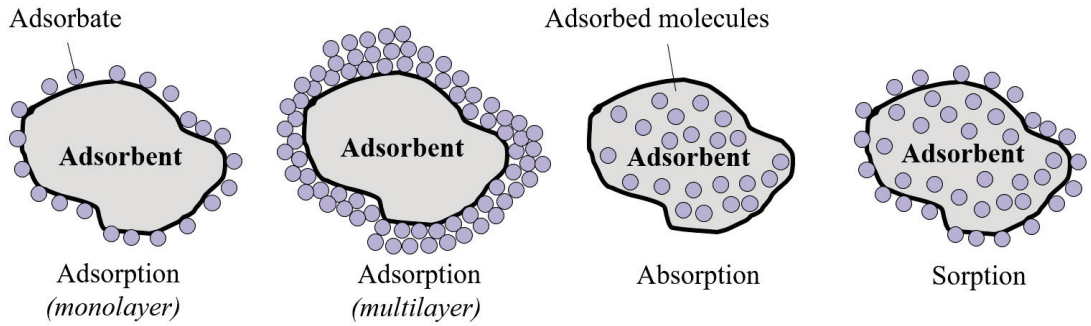

Figure 2.8: The process of adsorption, absorption, and sorption.

Adsorbates continuously accumulate on the surface of the adsorbent until an equilibrium is reached, where the rate of adsorption and desorption—leaving the adsorbent surface back to the gas or liquid media—is balanced. At this point, the adsorbent is considered saturated and the adsorption capacity, which is the amount of adsorbate taken up per unit mass (or volume) of the adsorbent, is maximum (Dąbrowski, 2001).

Several models are used to evaluate the adsorbent by measuring and describing the adsorption phenomenon: equilibrium at a constant temperature is described using isotherms and isothermal curves such as those by Langmuir, Henry, Freundlich, Temkin, Sips etc., (Al-Ghouti & Da'ana, 2020); kinetic and thermodynamic models describe the adsorption reaction and diffusion processes such as pseudo-first-order rate equation, pseudo-second-order rate equation, second-order rate equation, intraparticle diffusion etc., (Qiu et al., 2009).

Factors affecting adsorption include pH, temperature, matrix effects, characteristics of adsorbent and adsorbate, contact time, particle size, and concentration of adsorbate (L. Wang et al., 2020). The factor settings that favour adsorption parameters such as removal efficiency and adsorption capacity are first optimised followed by investigating how the adsorbate and adsorbent interact through thermodynamics, kinetics, and equilibrium studies. These studies to evaluate the adsorbent are carried out by either batch or column processes in lab-scale experiments.

2.4.2.1 Optimisation techniques

Optimising the adsorption-dependent factors mentioned in section 2.4.2 is important for improving the efficiency of the adsorbent and maximising the interaction between the adsorbent and the adsorbate. The adsorption capacity and removal of contaminants can be maximised by finding the best operating conditions for the adsorbent.

There are three main ways through which these optimal factor settings have been investigated: Ad hoc experiments, one-factor-at-a-time technique, and data-driven methods. Ad hoc experiments—a fancy term for an educated guess—are done by picking factor and factor settings that are known to maximise the adsorption process without the need to test other factor settings. They require pre-knowledge about the adsorbents and adsorbate behaviour; they are quick but highly inefficient and unscientific.

One-factor-at-a-time (OFAT), also referred to as the engineering method is a technique where one factor is studied as the other is held constant. Once the factor setting that leads to maximum adsorption has been determined, it is held constant and used to study the other factor settings. While OFAT experiments can be simple and easy to conduct, the pitfalls of such a process cannot be more obvious: they do not study the interaction between factors which could affect the adsorption process; a single factor would require around six to eight experiments to visualise the trend in adsorption, which lead to many experiments that are time-consuming and

resource wasteful especially when numerous factors are investigated; they fail to capture non-linear responses and are limited statistically leading to poor conclusions (Czitrom, 1999).

Data-driven methods include design of experiments (DOE) and artificial neural networks (ANN). These techniques supersede the rest as they are statistically designed tend to be more accurate, require a few experiments to study a lot of factors, screen out the less important factors, determine interactions between factors, and can be used for predictive modelling (Azad et al., 2016). The two can be used independently or in supplement with the other as used by Gadekar and Ahammed to model dye adsorption onto water treatment residuals (Gadekar & Ahammed, 2019). ANN techniques are out of scope in this work and more information related to the technique is available from the following reviews (Amrita Nighojkar et al., 2023; Ghaedi & Vafaei, 2017; Taoufik et al., 2021). Design of experiment is covered broadly in section 2.5.

2.4.2.2 Batch experiments

The basic setup of batch experiments (Figure 2.9a) involves adding a known amount of the adsorbent to a known concentration of adsorbate held in a vessel for a certain duration of time. The adsorbent and adsorbate can be stirred or shaken to enhance interaction after which the adsorbent is separated from the adsorbent through filtration or centrifugation. Adsorbents with magnetic properties have the additional advantage of being separated from the adsorbate using a magnet improving efficiency (Mehta et al., 2015).

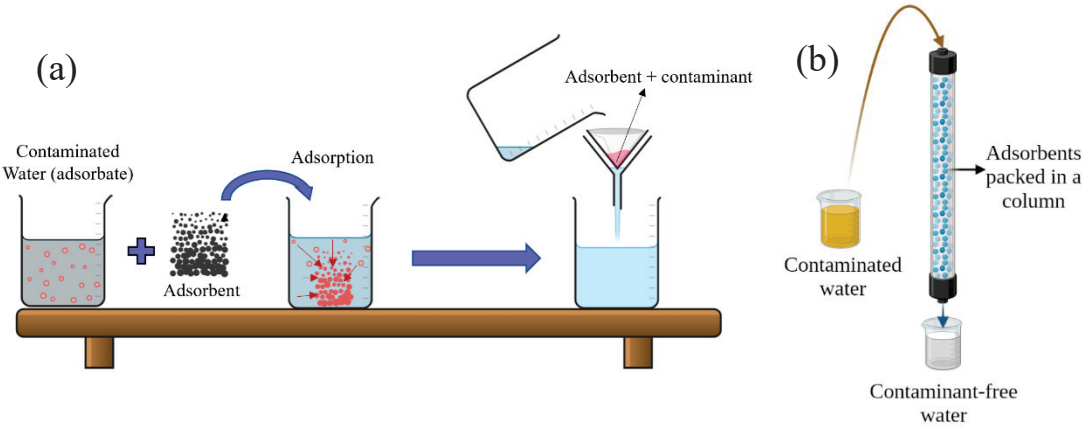

Figure 2.9: Setup for batch (a) and column (b) adsorption experiments.

Batch experiments are simple, cheap, and are often used to optimise the adsorption-dependent factors mentioned in section 2.4.2, determine adsorption parameters, and describe the kinetics and equilibria of the adsorption process. The major drawback of batch experiments is the small adsorbate volume and adsorbent quantity that can be practically applied, difficulty in retrieving and regenerating the adsorbent, limited dynamic adsorption since adsorbent behaviour is

locked in point and time over the duration of exposure, and cannot be used for desorption studies to have any practical industrial use (Patel & In, 2021)

2.4.2.3 Column experiments

The typical setup for column adsorption experiments involves passing a gas or liquid containing a known amount of the adsorbate of interest through a column packed with an adsorbent (Figure 2.9). A pump is used to pump the solution through the column at a rate that allows effective interaction between the adsorbate and adsorbent; hence, should be optimised.

This setup allows for the continuous monitoring of the adsorbent behaviour—not locked in point and time—providing more dynamic and richer information regarding adsorbent and adsorbate interaction compared to batch experiments. They simulate a more realistic scenario of an industrial application, kinetic and interaction mechanism obtained from such studies is detailed and allows for bench-scale experiments to be scaled to industrial applications using fixed-bed modelling data (Ahmed & Hameed, 2018). However, they are limited by the additional complexity of requiring a column, a pump, and piping systems; also, packing the column can be challenging and lead to uneven packing often reducing efficiency (Patel, 2019).

The column experiments can either be a fixed-bed column where the adsorbent material is held stationary inside a column or a moving-bed column where the adsorbent material is incessantly or intermittently moved through the adsorption column using a mechanical or pneumatic system (Schideman et al., 2006). Moving-bed columns are superior due to the high throughput and greater efficiency, but more expensive and complex. Fixed-bed columns are recommended for small-scale applications.

The adsorption process of a fixed-bed column is studied using breakthrough-curve—a plot of the ratio of effluent concentration to inlet concentration against time or volume—models which provide information about critical parameters such as adsorption capacity, column efficiency, breakthrough time, saturation time, and the time required for 50% breakthrough etc., (Z. Xu et al., 2013).

2.4.3 Fixed-bed adsorption modelling

Fixed-bed adsorption mentioned in section 2.4.2.3 results in breakthrough curves which are best investigated by comparing the experimental breakthrough curves to existing mathematical models. Ideally, the breakthrough curve should be rectangular, but the mechanisms mentioned in section 2.4.2 result in an S-shaped curve (sigmoidal) due to processes taking part in the mass

transfer zone (MTZ, Figure 2.10): axial dispersion, external film mass transfer, pore diffusion, and surface diffusion—also referred to as curve-broadening factors.

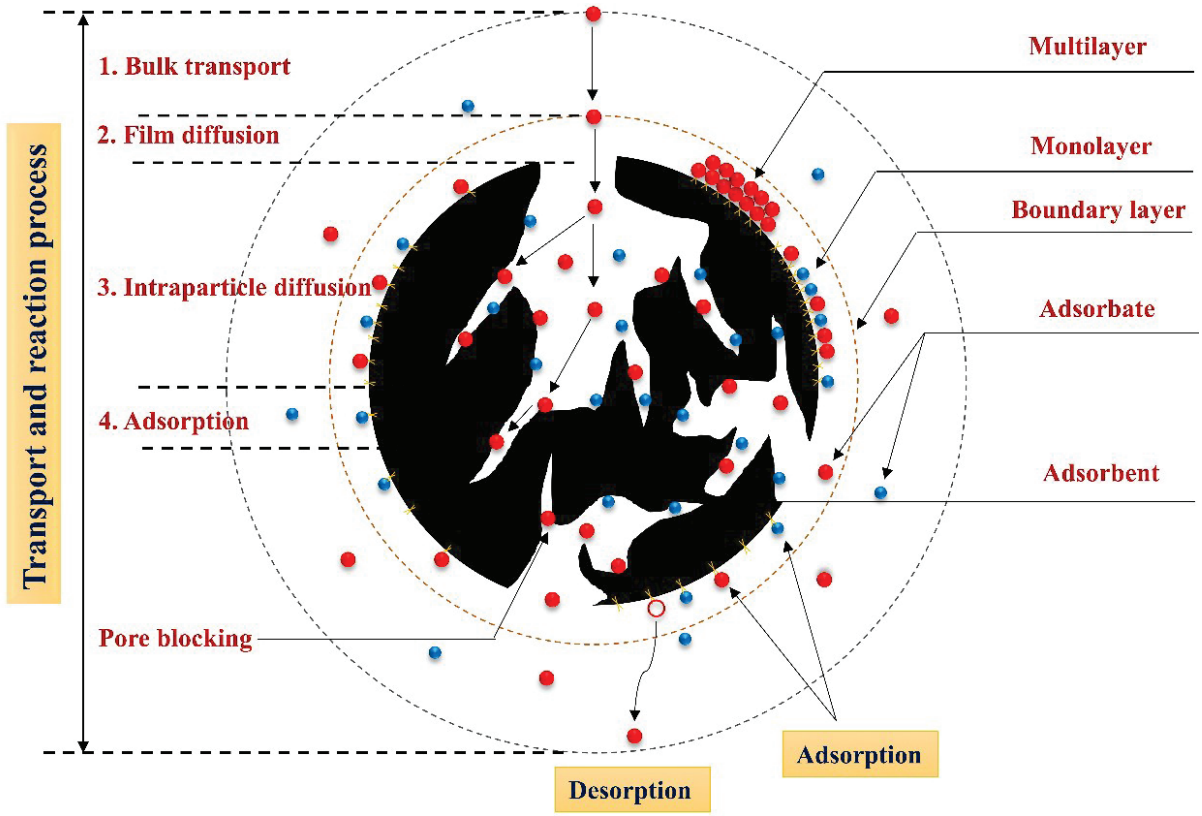

Figure 2.10: Mass transfer zone and curve-broadening processes taking place on porous adsorbents (Qili, 2019).

Various fixed-bed models grouped into three can be used to describe breakthrough curves. Data-driven models, also referred to as black-box models, such as artificial neural networks and design of experiments are the simplest as they require no understanding of the adsorption process; they are useful in optimising adsorption-dependent factors, but they can only be used within the design space and cannot be used to predict adsorbent behaviour outside this range.

Mechanism-driven models are best suited to modelling breakthrough cures because they consider conservation in mass, energy, and momentum physical principles. The differential mass balance equation (Eq. (2.3)) for the liquid phase is used to describe the adsorption process by assuming a singular adsorbate, spherical and uniform particles, constant velocity and zero dispersion (plug flow) is used to describe the adsorption process. The first term of equation (2.3), $v.\partial c/\partial z$, is the adsorbate concentration in the minus out, the second term represents the adsorbate accumulation on the liquid phase, while the third term describes the adsorbate accumulation on the adsorbent (Chu, 2022).

$$v\frac{\partial c}{\partial z}+\frac{\partial c}{\partial t}+\rho_\rho\left(\frac{1-\varepsilon}{\varepsilon}\right)\frac{\partial \bar{q}}{\partial t}=0 \tag{2.3}$$

The mass balance taking place on the adsorbent can be regarded as a function of the adsorbate concentration flowing in the influent and that adsorbed on the adsorbent and at equilibrium with the liquid phase (Eq.(2.4)). This rate expression can be rewritten as Eq. (2.5) considering a quick rate and an equilibrium existing at all points in all adsorbents in the interphase in the fixed-bed column.

$$\frac{\partial \bar{q}}{\partial t} = f(c,q^*) \tag{2.4}$$

$$\frac{\partial \bar{q}}{\partial t} = \left(\frac{\partial c}{\partial}\right)\left(\frac{dq^*}{dc}\right) \tag{2.5}$$

This equation (2.5) when substituted into the overall mass balance equation (Eq. (2.3)) results to Eq. (2.6). Rearranging and integrating and rearranging equation (2.6) yields the equation (2.7) where the axial distance (Z) is substituted with the length of the column (L) considering a breakthrough curve. Equation (2.7) is called the equilibrium non-dispersive model, which gives the time at which the effluent concentration is equal to the influent concentration: the time at which breakthrough occurs. This model is simple and only describes adsorption from a flow and thermodynamics perspective; hence, the breakthrough curve generated by this equation (Eq. (2.7)) is a step function.

$$v\frac{\partial c}{\partial z}+\frac{\partial c}{\partial t}\left[1+\rho_\rho\left(\frac{1-\varepsilon}{\varepsilon}\right)\frac{dq^*}{dc}\right]=0 \tag{2.6}$$

$$t=\frac{L}{V}\left[1+\rho_\rho\left(\frac{1-\varepsilon}{\varepsilon}\right)\frac{dq^*}{dc}\right] \tag{2.7}$$

Realistically, the equilibrium at the interphase between adsorbate molecules in the liquid phase and those on the adsorbate does not occur at all points exhaustively, neither is the rate of adsorption quick nor is adsorption purely dependent on just flow and thermodynamics. These reasons make the equilibrium nondispersive model (Eq. (2.7)) unfit to describe real breakthrough curves, which are typically S-shaped (sigmoidal) due to dispersive effects—the curve broadening factors mentioned in the first paragraph in this section.

To account for all curve-broadening factors, a list of partial differential equations based on the mass balance equation (Eq. (2.3)) needs to be solved leading to numerical solutions. Such an exercise requires complex software and expertise to solve these full mechanistic models. Considering a single curve broadening factor to represent all the others enables simple models to be generated and solved yielding analytical solutions; hence, referred to as semi-mechanistic

models. Though impractical, the equilibrium nondispersive model is useful in this case in approximating a favourable equilibrium used to find analytical solutions for the semi-mechanistic models.

Scientists have used this approach to generate breakthrough-curve models that assume a single curve-broadening factor that lumps all other dispersive factors. These scientists were Bohart and Adams famous for their Bohart-Adams model, and Thomas famous for his Thomas model.

2.4.3.1 Bohart-Adams model

As mentioned in section 2.4.3, Bohart and Adams offered the first analytical solution for the breakthrough curve when investigating chlorine adsorption onto charcoal in 1920 (Bohart & Adams, 1920). They developed a semi-mechanistic model by taking rate kinetics as the single curve broadening factor: a second-order irreversible kinetic model (Eq. (2.8)). At equilibrium, equation (2.8) reduces to an irreversible equilibrium—limiting form of a favourable equilibrium—where $\bar{q} = q_s$. Substituting equation (2.8) to the mass balance equation (2.3) led Bohart and Adams to develop an analytical solution that has been generalised by Amundson as equation (2.9).

$$\frac{\partial \bar{q}}{\partial t} = k_{BA} c (q_s - \bar{q}) \tag{2.8}$$

$$\frac{c}{c_0} = \frac{exp(\mathfrak{n}_{BA}\tau)}{exp(\mathfrak{n}_{BA}\tau) + exp(\mathfrak{n}_{BA}) - 1} \tag{2.9}$$

$$where \qquad \mathfrak{n}_{BA} = \frac{k_{BA}\rho_\rho q_s L}{v}\left(\frac{1-\varepsilon}{\varepsilon}\right) \tag{2.10}$$

$$\tau = \frac{c_0}{\rho_\rho q_s}\left(\frac{vt}{L} - 1\right)\left(\frac{1-\varepsilon}{\varepsilon}\right) \tag{2.11}$$

2.4.3.2 Thomas model

Thomas in 1944 assumed a Langmuir isotherm and a pseudo-second-order reaction rate (Eq. (2.12)) as the single curve broadening factor in deriving his solutions to explain the ion exchange taking place on zeolites in a column process. At equilibrium i.e., $\partial \bar{\mathrm{q}}/\partial \mathrm{t} = 0$, equation (2.12) corresponds to a Langmuir isotherm hence referred to as the Langmuir kinetic model.

$$\frac{\partial \bar{\mathrm{q}}}{\partial \mathrm{t}} = k_T \left[c(q_m - \bar{q}) - \frac{\bar{q}}{k_L}\right] \tag{2.12}$$

The solution to equation (2.3) considering equation (2.12) was derived by Thomas and generalised by Heister and Vermeulen as equation (2.13). This is praised as the first analytical solution for non-equilibrium conditions and non-linear isotherms.

$$\frac{c}{c_0} = \frac{1`}{1+\theta\, exp[(1-R)(\mathfrak{n}_T-\mathfrak{n}_T\tau)]} \tag{2.13}$$

$$where \qquad \mathfrak{n}_T = \frac{k_T\rho_\rho q_m L}{v}\left(\frac{1-\varepsilon}{\varepsilon}\right) \tag{2.14}$$

$$\tau = \frac{c_0}{\rho_\rho q_o}\left(\frac{vt}{L}-1\right)\left(\frac{1-\varepsilon}{\varepsilon}\right) \tag{2.15}$$

$$R = \frac{1}{1+k_L c_0} \tag{2.16}$$

$$\theta = \frac{1-J(x=\mathfrak{n}_T, y=R\mathfrak{n}_T\tau)}{J\left(x=R\mathfrak{n}_T, y=\mathfrak{n}_T\tau\right)} \tag{2.17}$$

$$and \qquad J(x,y) \cong \frac{1}{2}\left[1+erf\left(\sqrt{y}-\sqrt{x}\right)\right] \tag{2.18}$$

The J function presented as equation (2.18) is referred to as the Onsager approximation. Equation (2.13) is the real Thomas model which is superior to the Bohart-Adams model since it accounts for the Langmuir isotherm linearity; however, it is not user-friendly and cannot be used to estimate adsorption parameters using linear regression (Chu, 2010).

2.5 Design of experiment (DOE)

Design of experiment (mentioned in section 2.4.2.1) is a statistical approach to planning and analysing experiments by changing multiple factors simultaneously to investigate their effect on one or more responses. It is based on the factorial concept crafted by Fisher in the 1920s while trying to optimise wheat yield—best captured in his biography: "*The Life of a Scientist*" (Yates & Fisher, 1979). The emphasis of DOE is on the design rigour rather than analysis afterwards; hence, the famous quote by Fisher (Cox, 2017): "*To consult the statistician after an experiment is finished is often merely to ask him to conduct a postmortem examination. He can perhaps say what the experiment died of.*"

A factorial experiment is where two or more factors and all their possible combinations are investigated simultaneously. The beauty of such experiments is in the few experiments and the added advantage of studying how different factors interact with one another. Factorial experiments follow three key principles: randomising the experiments to reduce bias and spread nuances from uncontrollable factors; replicating the experiments to improve the

probability of making fewer errors; and blocking, which is simple a method to block out uncontrollable factors (J. B. Fisher, 1980).

The most common factorial experiments in optimising adsorbent-dependent factors are two-leveled. Here, each factor is set up using only two levels: the highest level (+1) and the lowest level (-1). The total number of experiments required is determined by equation (2.20) where n is the total number of factors and 2 represents the factor levels (Figure 2.11). The number of experiments can be represented visually as the corners of a square or a cube (Fig.). It is encouraged to include a wide range between the two-factor settings to completely capture the design space. Although three-leveled factorial experiments are possible and provide more accuracy, they result in very large experiments determined by 3^n, which are unsustainable owing to the little value that they add (Montgomery, 2019).

$$2^n \tag{2.19}$$

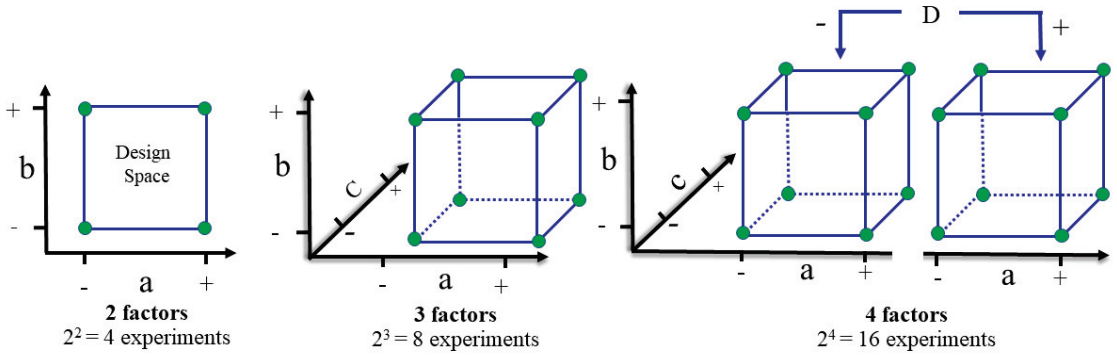

Figure 2.11: Graphical representation of thr number of experiments and the design space
(a, b, and c are factors)

Designed experiments consist of two main parts: screening designs to find the most important factors, followed by optimisation and modelling.

2.5.1 Screening designs

The first step in design of experiment is to screen for all factors that may affect your process. They generally test whether the change in a factor's setting produces a large enough effect to be considered important—active factors. Significant effects from two factors interacting with one another can also be investigated at this point. Once the active factors have been identified, a main-effects linear regression model (Eq. (2.20) is generated at this point, where β_0 is the intercept, β_i are the partial regression coefficients, x are the factors, ε is the error. In addition to the number of experiments required (Eq. (2.19), centre points, which are the midpoints between two-factor levels, are added and replicated to estimate the error (ε).

$$y = \beta_0 + \sum_{i=n}^{n} \beta_i x_i + \varepsilon \tag{2.20}$$

Screening designs can be full factorials when considering a few factors or fractional factorials to reduce the number of experiments when a lot of factors are taken into consideration. The number of experiments required for fractional factorials is determined by equation (2.21) where p represents the number of half-fractions and res indicates the resolution of the resulting design. The fractional factorials are associated with the projection property where all fractional factorials can be regarded as full factorial studies in fewer factors (Figure 2.12).

$$2_{res}^{n-p} \tag{2.21}$$

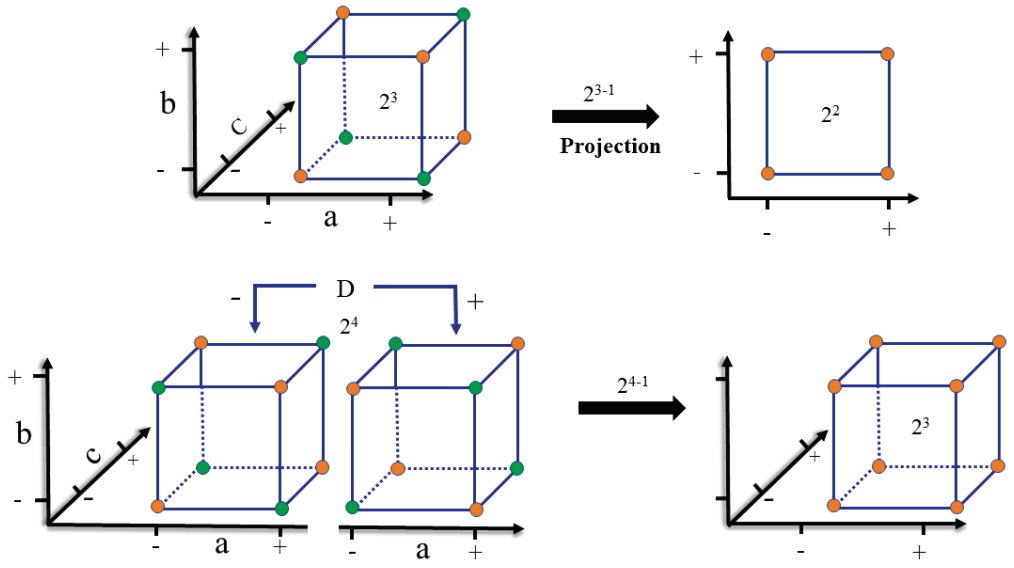

Figure 2.12: Projection property of fractional factorial designs

(a, b, and c are factors)

Since fractional factorials are a quid pro quo type of arrangement, the accuracy of the number of interactions and main effects that you can study reduces the more you take bigger fractions. This is because of the confounding of main effects and interactions when performing fractional factorials. Resolution (res) in this case helps to categorise fractional factorials and indicate the aliasing between main effects and interactions—when two effects are aliased with one another, it becomes difficult to tell them apart and determine where the effect is coming from (Montgomery, 2019).

Fractional factorials of resolution III design have main effects aliased with all two-factor interactions: resolution IV designs have two-factor (2fi) factor interactions aliased with one another, and resolution V designs have two-factor interactions aliased with one another. Resolution III and IV designs are used in screening designs, but resolution V designs are

usually too large to be practical. Placket-Burman (PB) designs are a class of resolution III designs useful in reducing the number of experiments required, but they involve complex aliasing structures hence irregular designs (Tyssedal, 2008).

2.5.2 Response surface methodology

The previous section's focus was on screening to find the most important factors. After getting the active factors, the next question is how to find the levels of these factors that get the best results: optimisation—in our case, maximising adsorption. Response Surface Methodology (RSM), whose focus is optimisation, is useful in such cases. RSM is a collection of mathematical and statistical techniques used in modelling which include either central composite designs (CCD,) or Box-Behnken designs (Montgomery, 2019).

In a situation where the optimal region was not captured in the screening design, a method of steepest ascent approach finds the factor levels that include the optimal region. The main-effects linear regression from the screening design (Eq. (2.20) is used in this approach. This is then followed by augmenting the design with centre points to estimate curvature and axial to satisfy the rotatable property of a CCD. The total number of experiments required for RSM is given by equation (2.22) where n is the number of factors and n_c is the number of centre points. Generally, a minimum of 3 centre points is suitable to give a reasonable prediction variance (Montgomery, 2019).

$$2^n + 2n + n_c \tag{2.22}$$

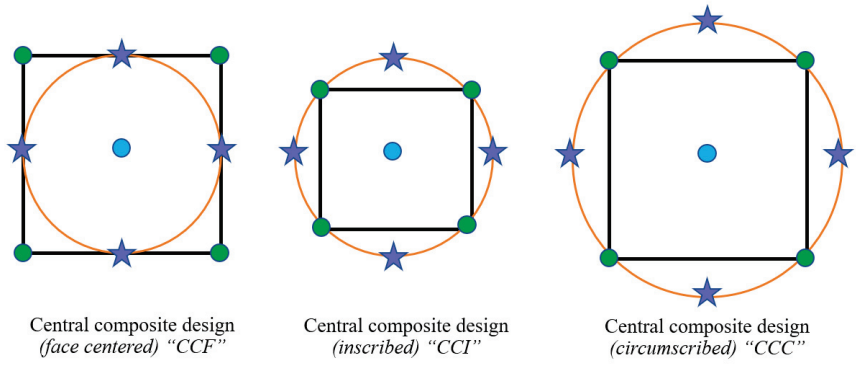

Figure 2.13: Central composite designs, axial points and the rotatability property.

In addition to equation (2.20), RSM includes the two-way interaction ($\sum\sum_{i<j}^{n} \beta_i\, x_i x_j$) and pure quadratic ($\sum_{i=n}^{n} \beta_i\, x_{ii}^2$) effects to generate a second-order model (Eq. (2.23)). This model is used for optimisation and can be satisfactorily used for prediction modelling.

$$y = \beta_0 + \sum_{i=n}^{n} \beta_i x_i + \sum \sum_{i<j}^{n} \beta_i x_i x_j + \sum_{i=n}^{n} \beta_i x_{ii}^2 + \varepsilon \quad (2.23)$$

Curvature for each factor in RSM is investigated using the interaction effects and quadratic effects. If one exists the stationery points are derived to give an idea whether the points are a maximum, minimum, or a point of inflection—saddle point. The resulting surface plots are used to find the optimum factor settings.

Chapter 3: Bisphenol-A Adsorption onto Villi-Structured Polyaniline, and its Carboxymethyl and Dialdehyde Carboxymethyl Cellulose Composites: A Customised and Definitive Screening Designed Experiments Approach

3.1 Introduction

Polyaniline-based materials are desirable adsorbents: their preparation methods are simple, cheap, and environmentally friendly; are easily modified; and their properties can be easily tailored for enhanced adsorbent-adsorbate interaction (Samadi et al., 2021c). The morphology of polyaniline can be tuned using hard, soft or template-free synthetic methods enhancing its performance for intended applications (Boeva & Sergeyev, 2014; Tran et al., 2011). Recently, Seung and their group proposed an organic single-crystal surface-induced technique to polymerise aniline which yields polyaniline sheets with surface villi-like structures (Hwang et al., 2018). Whereas the study shows how this morphology boosts the conductivity property of polyaniline, the effect on the adsorption remains unstudied.

In addition to tuning the morphology, polyaniline is applied either in its nano form, hybridised with other molecules (Chinnathambi & Alahmadi, 2021; Y. Gao et al., 2016; Hsini et al., 2021), or crosslinked to improve its sorption performance (Germain et al., 2007). However, hybridising polyaniline with other materials can negatively impact some of its properties (F. T. Liu et al., 1999). Carboxymethyl cellulose (CMC) is one environmentally friendly biopolymer that has been successfully used to improve the performance of polyaniline material (Megha et al., 2018; Olad et al., 2021). However, some studies have reported that the oxidised species of CMC, dialdehyde carboxymethyl cellulose (DCMC), performs better in hybrid adsorbent materials (Asere et al., 2019; Heydari et al., 2022; M. Huang et al., 2022; Sethi et al., 2020). Although these prior studies demonstrate that DCMC is better, they fail to investigate the effect of varying the aldehyde content of DCMC and comparing the performance to CMC. One of the reasons could be the substantial number of experiments required to study multiple adsorbents for each adsorption-dependent factor.

A solution to this would be through a design of experiment (DOE) approach discussed in section 2.5—as opposed to a one-factor-at-a-time—to get richer and more accurate cause-and-effect information from multiple factors using fewer experiments (Allouss et al., 2019; Asfaram et al., 2015; R. A. Fisher et al., 1980; Uy & Telford, 2009). Classical DOE is ideal, but its sequential nature can translate to a large study for many factors. Classical-fractional factorials or Plackett-Burman designs would reduce the number of experimental runs but confounding effects become a major issue with such designs (Lundstedt et al., 1998). Definitive

screening design (DSD), a class of three-level optimal designs, combines screening and optimisation reducing experimental runs to N=2k+1 or 2k+3 for even and odd factors (k) (Jones & Nachtsheim, 2011a). Main linear effects (MLEs) which are orthogonal and uncorrelated to unconfounded two-factor interactions (2FIs), and quadratic effects are all estimable in a single DSD experiment which can project into a response surface method (RSM) in at most three factors for a study involving at least five factors (Johnson & Jones, 2011; Jones & Nachtsheim, 2011b). However, DSDs are limited to two levels per factor during the design, which reduces the power for determining main effects when dealing with categorical variables (Jones & Nachtsheim, 2013), and the original factor settings may not capture the optimal region.

We asked whether villi-structured polyaniline (VSPANI) would be a good adsorbent using bisphenol A (BPA) as the target analyte; additionally, whether composting VSPANI with CMC or DCMC with varied aldehyde content would enhance its adsorption performance. We selected BPA as our model analyte because it is a micropollutant of great concern owing to its high occurrence in the environment and the high health risk of disrupting the endocrine system hence necessitating its removal (Corrales et al., 2015; Yang et al., 2022).

Here we investigate the cause and effect of some adsorption-dependent factors to study for the first time the adsorption capability of VSPANI and the effect of aldehyde content of its carboxymethyl cellulose-derived composites on adsorption. We customised a screening design of the D-criterion (de Aguiar et al., 1995) prior to the definitive screening design to accommodate a categorical variable in four levels, study the main effects plus one interaction at a satisfactory power, and investigate the optimum region. We further use a definitive screening design to examine the second-order effects, find the optimal factor settings, and generate predictive models for the best-performing adsorbent. This study can also serve as a guide to screening multiple adsorbents and optimising adsorption-dependent factors quickly, accurately, and efficiently before conducting a more intensive evaluation of the adsorbent.

3.2 Methodology

3.2.1 Materials

Sodium decane-1-sulphonate (SDSn, ≥98%) was purchased from Tokyo Chemical Industries. Carboxymethyl cellulose (CMC, CAS 039-01335), sodium periodate (≥99.5%), hydroxylammonium chloride (≥98%), N,N-Dimethylformamide (DMF, ≥99.5%), concentrated hydrochloride (HCl, 35%), 1.0 M sulphuric acid (H_2SO_4), methanol (≥99.7%), ethanol (≥99.5%), acetone (≥99.5%), and 1.0 M sodium hydroxide (NaOH) were purchased from Wako Chemicals. Ammonium peroxodisulphate (APS, ≥98%), aniline (≥99%), and bisphenol-A (BPA, ≥99%) were purchased from Nacalai tesque.

3.2.2 Preparation of dialdehyde carboxymethyl cellulose

DCMC(A) with an 80% theoretical degree of oxidation was prepared using a method outlined by (H. Li et al., 2011) with slight adjustments in the weights and volume. Carboxymethyl cellulose (CMC), 1.0g, was dissolved in 20 mL distilled water contained in a 50 ml conical flask and constantly stirred to a clear solution. An oxidant solution prepared by dissolving 2.2 g of sodium periodate in 20 mL distilled water was added to the CMC solution dropwise while stirring. The pH of this solution was adjusted to pH 3.0 using 1 M H_2SO_4 solution and the mixture was stirred in the dark for 4 hrs at 35 $°C$. The solution was poured into 200 mL of ethanol to precipitate the oxidised product which was recovered by vacuum filtration on a Sibata glass filter (4 - 5.5 μm) followed by washing with 50% v/v ethanol and 99.5% v/v ethanol to remove all iodic compounds.

The recovered product was dried at 37 $°C$ to a constant weight and ground to a fine powder using a mortar and pestle before storage in a desiccator. DCMC(B) with a theoretical degree of oxidation of 40% was prepared in a similar procedure using 1.1 g of sodium periodate in 20 mL of distilled water.

3.2.2.1 Determination of the degree of oxidation of DCMC

The degree of oxidation of DCMC was calculated by determining the aldehyde content converted to oxime using a Schiff's base reaction. The procedure used is as described by Jiang et al., (2016): 50 mg of DCMC was dissolved in 2.5 mL distilled water and the pH was adjusted to 5.0 using 0.1 M sodium hydroxide, 4 mL of 0.72 mol/L hydroxylamine hydrochloride at pH 5.0 was added and stirred for 4 hours in a water bath. The solution was titrated against 0.1 mol/L NaOH. A similar concentration of CMC at pH 5.0 was used as the blank. The titrations were done in triplicate and the degree of oxidation was calculated using Eq. (3.1)

$$D.O(\%) = \frac{M_{(NaOH)}{}^{(V_c - V_b)}/_2}{m/_{211}} \quad (3.1)$$

Where $M_{(NaOH)}$ = 0.1 M NaOH, V_c is the sample titre, V_b the titre for the blank, m is the dry weight of DCMC sample in g, and 211 is the average molecular weight of the repeating unit in DCMC.

3.2.3 Preparation of aniline hydrochloride

Aniline hydrochloride was prepared as per the procedures by Witten and Reid (1950): 8 mL (90.4 $mmol$) of concentrated HCl was added to 8.67 mL (90.4 $mmol$) of previously distilled aniline in an evaporating dish and heated to dryness on a hotplate. Aniline hydrochloride was heated in an oven at 120℃ prior to use.

3.2.4 Preparation of villi-structured polyaniline and carboxymethyl cellulose composites

Villi-structured polyaniline was synthesised as described by Hwang et al., (2018) with volume and mass adjustments (Figure 3.1). Sodium 1-decanesulfonate, 975 mg (4 mmol), was dissolved in 30 mL of 0.01 M HCl aqueous solution, stirred at 30℃ for 15 min then cooled down to 0℃ with vigorous stirring for 15 minutes at 900 revolutions per minute to recrystallise and stabilise it.

A monomer solution containing 520 mg (4 mmol) of aniline hydrochloride in 10 mL 0.01 M HCl was added to the stabilised SDSn solution and stirred for an hour. An oxidant solution of APS, 900 mg (4 mmol) in 10 mL of 0.01 M HCl was cooled to 0 °C then added to the solution at a rate of 10 mL/hr using a syringe pump and continuously stirred. Polymerisation was carried out for 5 hours at a constant stirring rate of 500 rpm.

The products were vacuum filtered on a 4 - 5.5 µm Sibata glass filter, washed severally using 0.01 M HCl aqueous solution, methanol, and acetone then dried in an oven for 24 hrs at 40 °C. The composites were prepared similarly, but the monomer solution was initially stirred with an additional 120 mg (ratio of 1:5 to aniline hydrochloride) of either CMC, DCMC(A) or DCMC(B) for 2 hours at room temperature, cooled to 0 °C then introduced to the SDSn solution before polymerisation. The adsorbents were designated as VSPANI, CMC/PANI, DCMC(A)/PANI and DCMC(B)/PANI.

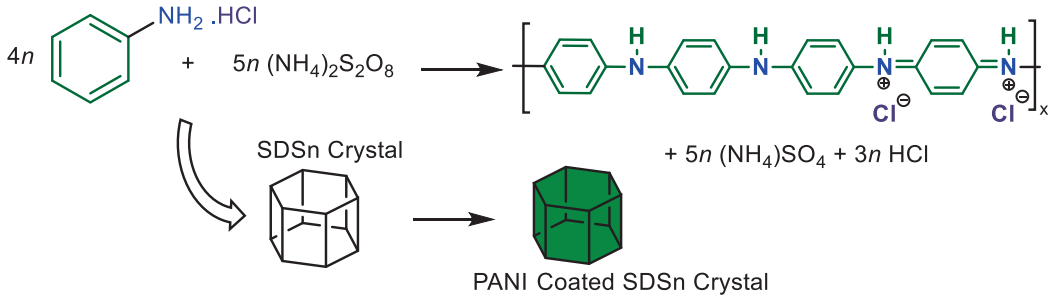

Figure 3.1: Reaction scheme showing polyaniline synthesis on an organic single crystal.

3.2.5 Characterisation

The surface morphology and particle sizes of the polymers were checked using a Hitachi scanning electron microscope (SEM) SU3500. Functional groups were studied using a Perkin Elmer Spectrum 400 Fourier Transmission Infrared spectrophotometer (FTIR) equipped with a GladiATR monolithic diamond Attenuated Total Reflectance (ATR) cell; the obtained spectra were from an average of 30 scans set at 4 cm^{-1} resolution in the range $4000 - 400\ cm^{-1}$ The cell was cleaned and dried between samples using isopropyl alcohol. Wide-angled diffraction patterns of the polymers were recorded on a Rigaku ULTIMA IV powdered X-ray diffractometer (XRD) using Cu Kα radiation (λ = 1.5418). UV spectra of the polymers suspended in DMF (5mg in 10 mL) were conducted on a Shimadzu U-4100 UV-Vis spectrophotometer.

3.2.6 Fixed-bed adsorption procedure

A fixed bed microcolumn system was used as opposed to a batch system to mimic a column system simulative of an industrial process, easy handleability, adaptability, and recyclability of the adsorbents (Albadarin et al., 2012). A known amount of the adsorbent was packed between two quartz wool of 2-6 µ fibre diameter inside a 15 cm long glass Pasteur pipette, 0.5 cm internal diameter (ID) that functioned as the column. The quartz wool was placed at a level so that the absorbent rested above the curved section of the pipette to reduce the variability arising from packing the adsorbents. The packed columns were washed with methanol and soaked overnight in deionised water to rid of the airspaces in between the particles before analysis. A syringe pump (YMC, YSP-101) was used to deliver the sample contained in a 20 mL syringe to the top of the column via a snuggly fit silicone tube of 0.3 cm ID and 0.6 mm outer diameter (OD). The snug fit was important to ensure a constant flow rate during the experiment.

3.2.7 Adsorbate preparation and analytical analysis

BPA stock solution, 1000 mg/L, was prepared by dissolving 50.51 mg of BPA in 50 mL deionised water containing 15 mL ethanol. Working standards and sample solutions were

prepared from a 100 mg/L working stock. Direct photometric determination was conducted at a wavelength of 276 nm on a Shimadzu U-4100 UV-Vis spectrophotometer.

3.2.8 Design of experiments

3.2.8.1 Custom screening design

A design of experiment method using JMP®, version 16.2 software, was adopted to study the adsorption of bisphenol-A onto the adsorbents with subsequent optimisation and modelling. A customised screening design of D-optimal criterion with 16 experimental runs was selected to conduct initial screening for the best-performing adsorbent of the four polymers (categorical variable in four levels), screen the active factors from four continuous variables affecting the adsorption of BPA onto the adsorbents (Table 3.1), and estimate the optimum region. Sample volume with a priori effect was left out in the initial screening to reduce the number of runs. Two responses, removal efficiency, and adsorption capacity calculated as per Eqs. (3.3) and (3.4) were chosen as the responses with the desirability set to maximise both. Additionally, we were interested in checking whether the change in initial concentration interacted with the change in pH.

3.2.8.2 Definitive screening design and response surface method

Two closely related adsorbents performance-wise and four active factors were taken through a definitive screening design to further screen for the active factors, check for all two-way interactions, account for curvature, find the optimal operating conditions, and generate predictive models for removal efficiency and adsorption capacity. Sample volume was added to account for the change in volume in the final model and the highest level of initial concentration was changed from 70 mg/L to 85 mg/L to move it into the optimum region for both responses (Table 3.1). The definitive screening design incorporated centre points represented as level 0 to account for curvature. A Response surface method (RSM) projected from the definitive screening design was used to determine the optimal conditions by fitting in and finding solutions to second-order regression models (Eq. (3.2)) accounting for linear, quadratic and interactions for each response.

$$y = \beta_0 + \sum_{i=2}^{6} \beta_i x_i + \sum_{i=2}^{6} \beta_{ii} x_i^2 + \sum_{i=2}^{6} \sum_{j=3}^{6\,(i<j)} \beta_{ij} x_i x_j + \varepsilon \qquad (3.2)$$

Where: x and y are the input and predicted values; β_0, β_i, β_{ii}, and β_{ij} are the regression coefficient for the intercept, linear, quadratic, and interaction terms respectively; ε is the error term also referred to as the residual term.

The experimental runs from all designs were randomised to spread out nuances from uncontrollable factors. The suitability of the two designs was evaluated through power analysis, average prediction variance, and correlation maps. The matrix tables for each design are presented in Appendix I and Appendix II.

Table 3.1: Custom and definitive Screening design factors, coding, levels and responses.

Factors	**Units**	**Coding**	**Levels**	**Natural Variables**	
				Custom Design	Definitive Screening
Adsorbent Type	—	x_1	L1	VSPANI	VSPANI
			L2	CMC/PANI	—
			L3	DCMC(A)/PANI	—
			L4	DCMC(B)PANI	DCMC(B)PANI
Initial Concentration	mg/L	x_2	$+1$	70	85
			0	—	45
			-1	5	5
pH	—	x_3	$+1$	10	10.0
			0	—	6.5
			-1	3	3.0
Rate	mL/min	x_4	$+1$	1.0	1.00
			0	—	0.58
			-1	0.2	0.16
Adsorbent Amount	mg	x_5	$+1$	15	15
			0	—	10
			-1	5	5
Sample Volume	mL	x_6	$+1$	—	20
			0	—	15
			-1	—	10
Response			**Equation**		
Removal Efficiency	%	y_1	$\frac{(C_f - C_0)}{C_0} \times 100$		(3.3)
Adsorption Capacity	mg/g	y_2	$\frac{(C_f - C_0)}{m} \times V$		(3.4)

(C_0 & C_f = concentration before and after adsorption, m = mass in grams and V = volume in Litres)

3.2.8.3 Model fitting and data validation

The custom design model was fit using a standard least square personality with an effects screening emphasis while the definitive screening design was fit using effective model selection. Being linear regression models, both graphical and numerical model adequacy checks were used to check that the residuals had a constant variance, were normally distributed, and were independent of one another over time. Graphical adequacy checks included checking the actual vs predicted plots, normal quantile plots, residual vs predicted and studentised residual plots. Numerical adequacy checks involved the use of analysis of variance (ANOVA),

coefficient of determination (R^2), adjusted coefficient of determination (R^2_{adj}), predicted residual error sum of square (PRESS), and lack of fit. The confidence level for the statistical tests was 95% (2 standard deviations) and where applicable, data are presented as mean ± SD.

3.3 Results and Discussion

3.3.1 Characterisation

3.3.1.1 Synthesis of dialdehyde carboxymethyl cellulose

This study abbreviates the oxidised species as DCMC(A) and DCMC(B) referring to an aldehyde content of $35 \pm 0.7\%$ and $77 \pm 1.3\%$ respectively. CMC was successfully oxidised as evidenced by the FTIR spectra (Figure 3.2): the peak in the region 1732 cm^{-1} attributed to the stretching vibration of a carbonyl confirmed the newly formed aldehydic carbonyl group and the peak at 891 cm^{-1} implied hemiacetal bonds forming between the aldehydic groups and neighbouring hydroxyl groups (Jiang et al., 2016).

CMC's smooth irregular long fibres of 19.35 ± 0.54 µm average diameter were converted to needle-like fibres of average diameters of 0.43 ± 0.03 μm and 0.59 ± 0.01 μm for DCMC(A) and DCMC(B) respectively (Figure 3.3).

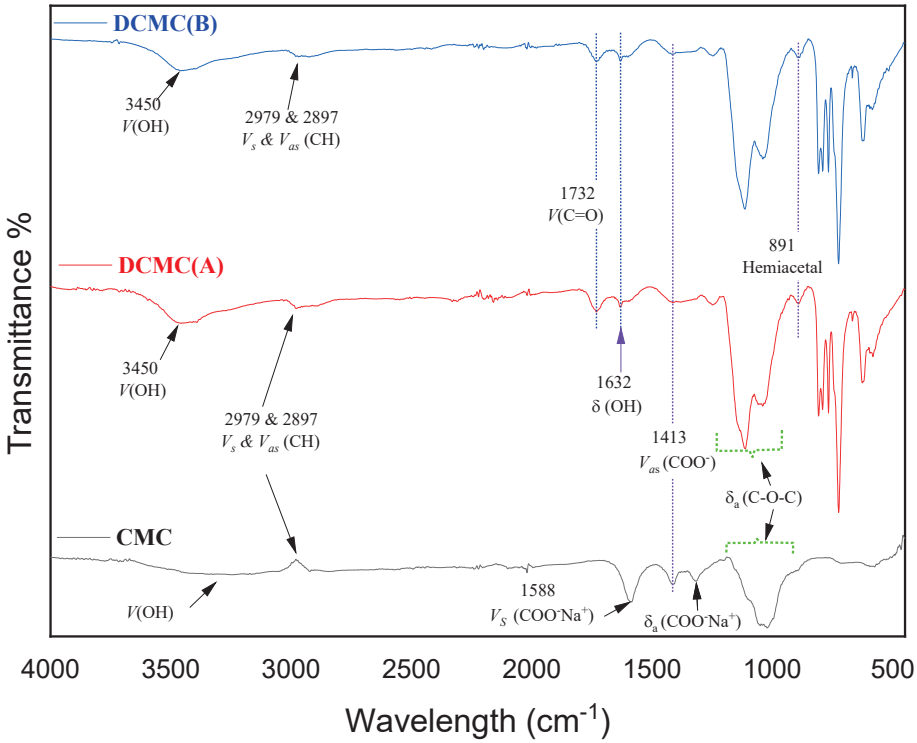

Figure 3.2: CMC, DCMC(A) and DCMC(B) FTIR-ATR spectra.
(v = stretch vibration, v_s = symmetric stretch, v_{as} = asymmetric stretch, δ = bending vibration)

VSPANI, CMC/PANI, DCMC(A)/PANI, and DCMC(B)/PANI had common FTIR peaks (Fig.1): 1565 cm^{-1} and 1481 cm^{-1} corresponding to stretching vibrations for $C = C$ of quinoid and benzenoid rings respectively; 1294 cm^{-1} and 1245 cm^{-1} representing $C - N$ and $C - H$ bending vibrations of benzenoid and quinoid rings respectively (Zhang et al., 2017). The peaks for PANI in the composites' matrices shifted to lower wavenumbers, were broadened, and had lower intensity implying that the interactions between the composites and VSPANI occurred

through bidentate or bifurcated hydrogen bonding (Figure 3.5) (Anton et al., 2020; Gorman, 1957; Moraes & Motheo, 2006). This suggests that CMC/PANI has denser hydrogen bonding networks with these network densities decreasing with an increase in the aldehyde content in the DCMC composites.

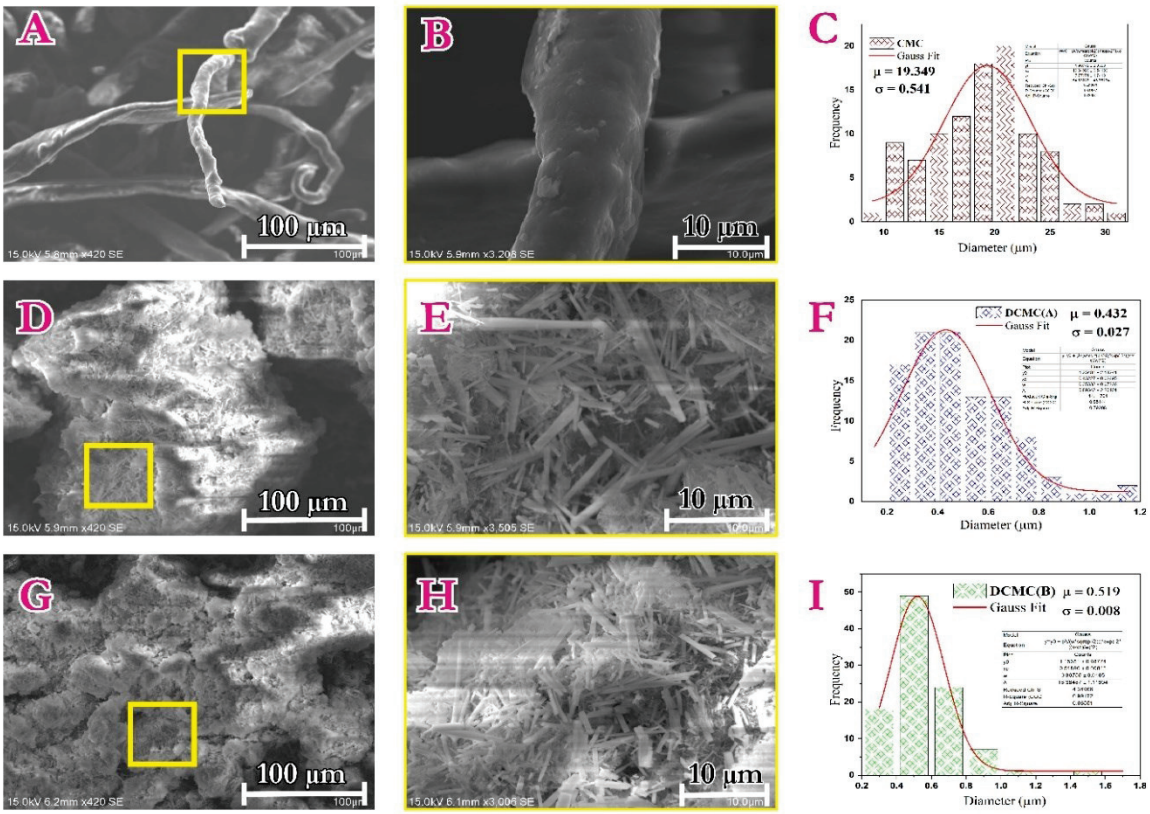

Figure 3.3: FTIR spectra and size distribution histograms for CMC (a-c), DCMC(A) (d-f), and DCMC(B) (g-i)

VSPANI and the composites had granular structures (Figure 3.6) of varying particle sizes: 11.84±0.63 µm, 29.48±0.63 µm, 52.02±1.03 µm, and 116.30±3.20 µm for VSPANI, DCMC(B)/PANI, DCMC(A)/PANI, and CMC/PANI, respectively. We related this particle size increase to the increase in hydrogen-bonding density. Villi structures were well defined on VSPANI (Appendix III); they were not observed on PANI/CMC, but less defined on the surfaces of DCMC(A)/PANI and DCMC(B)/PANI. The hydrogen bonding density influenced the formation of these villi structures by interfering with the initial interaction between the aniline monomer and the surface of the SDSn organic crystal.

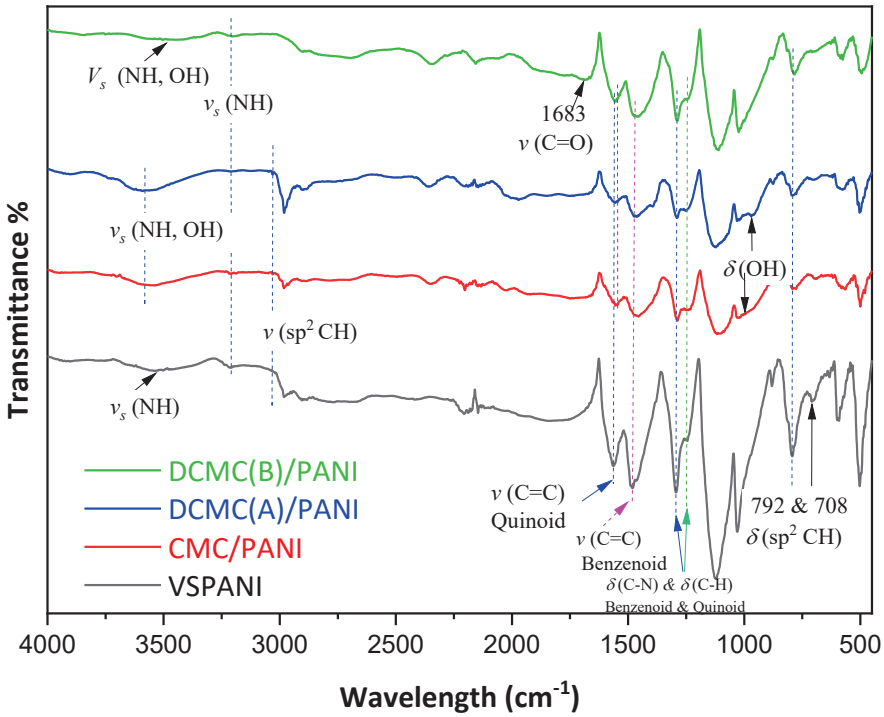

Figure 3.4: FTIR-ATR spectra for VSPANI, CMC/PANI, DCMC(A)/PANI and DCMC(B)/PANI.

(v = stretch vibration, v_s = symmetric stretch, δ = bending vibration)

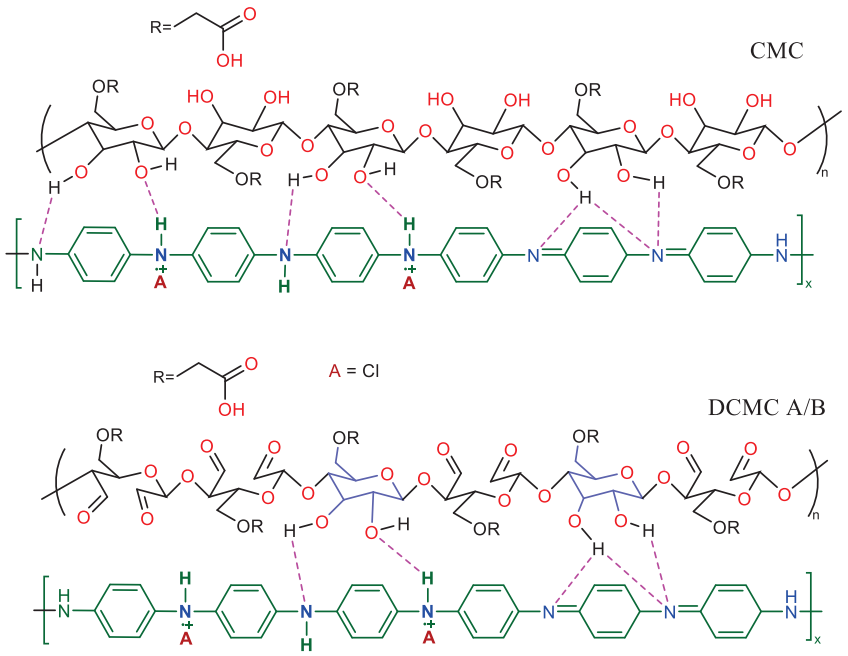

Figure 3.5: Hydrogen bonding interaction between CMC and PANI backbone.

The peaks at 295 nm and 624 nm from the UV-VIS absorption spectra (Figure 3.7) were from π–π^* and n–π^* transitions within the benzenoid and quinoid segments respectively (Yavuz et al., 2009). The peaks at 443 nm and 853 nm that appeared in the composites but were absent in VSPANI are typical of the protonated form of PANI from the formation of delocalised

polarons in mildly acidic solutions (Kizildag et al., 2014). While the appearance of the peak at 853 nm is usually associated with the disappearance of the one at 624 nm, the presence of these two together confirmed that the composites protonate the PANI base (Stejskal et al., 1993; Wan, 1992). We used the UV data to calculate the protonation and oxidation states of the polymers (Table 3.2). VSPANI had the highest oxidation state while DCMC(A)/PANI had the highest oxidation state and protonation states among the composites hence a larger character of the quinoid segment of PANI in the polymer matrix compared with the others (Figure 3.8).

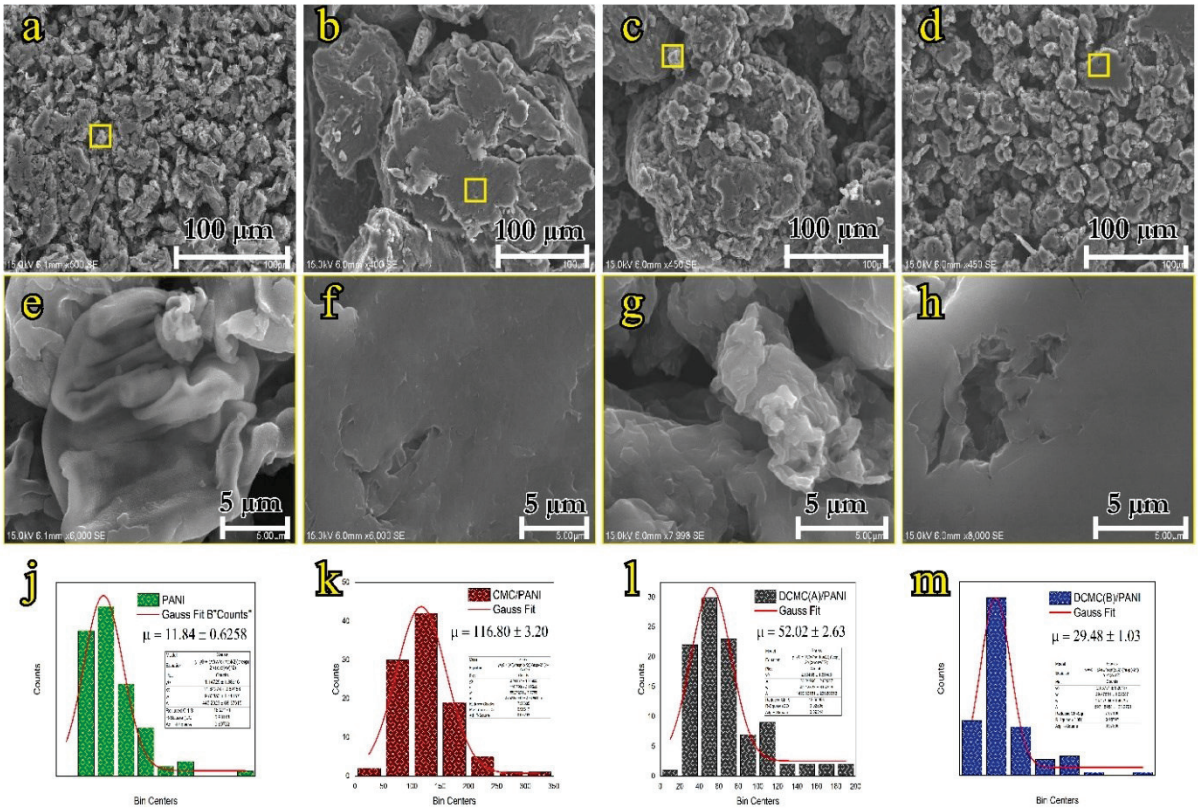

Figure 3.6: SEM micrographs at 100 µm and 5µm scale with particle size histograms embedded with normal distributions for VSPANI: a, e, and j; CMC/PANI: b, f, and k; DCMC/PANI: c, g, and l; and DCMC(B)/PANI: d, h, and m

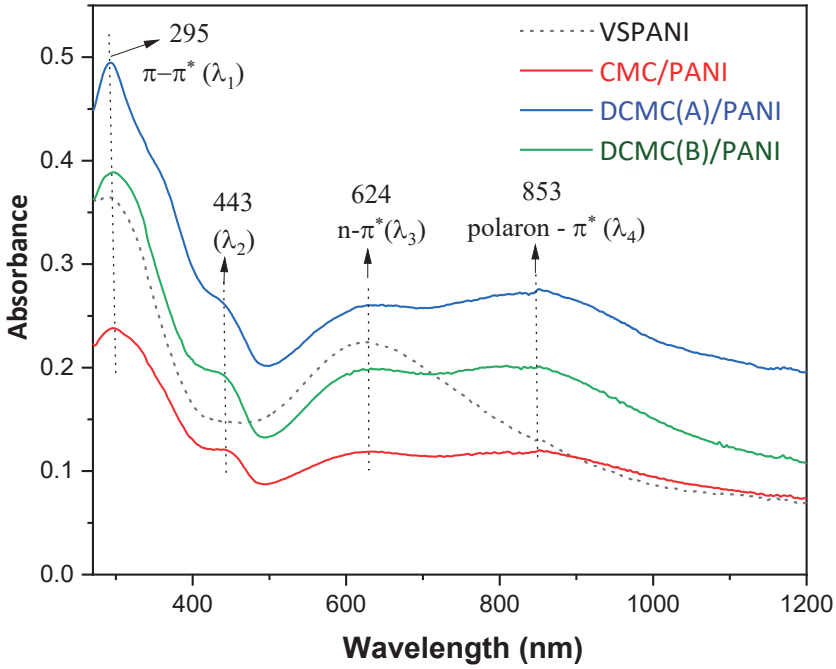

Figure 3.7: UV-Vis absorption spectra for VSPANI and its CMC-based composites

Table 3.2: Oxidation and protonation states for VSPANI and its CMC-based composites.

		VSPANI	CMC/PANI	DCMC(A)/PANI	DCMC(B)/PANI
Oxidation state (y)	$\frac{A_{\lambda_3}}{A_{\lambda_1}}$	0.615	0.497	0.525	0.508
Protonated state (x)	$\frac{A_{\lambda_4}}{A_{\lambda_3}}$	n/a	1.011	1.061	1.014

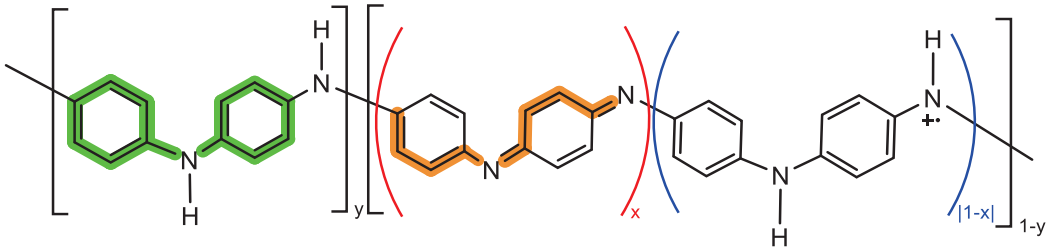

Figure 3.8: Molecular structure of PANI showing the polaron lattice, protonation state (x parameter) and the oxidation state (y parameter) where 0≤y and x≤1.0 (Wan, 1992)

VSPANI and the three composites had three diffraction peaks at $2\theta = 15°, 19° \; and \; 25°$ (Figure 3.9) similar to those for pure crystalline polyaniline indicating (011), (020) and (200) crystalline planes of the emeraldine salt form (Mitra et al., 2015; Z. Wang et al., 2019). The intensity of the peak at 15° is considered more specific to VSPANI than to conventional PANI (Hwang et al., 2018). The two peaks at $19° \; and \; 25°$ represent the alternating distance between polymer chains and the scattering from the periodicity perpendicular to PANI chains

respectively (Peng et al., 2012). None of the composites' respective diffraction peaks appeared superimposed onto VSPANI's because the contents of CMC, DCMC(A) and DCMC(B) were small and uniformly dispersed in the composite material.

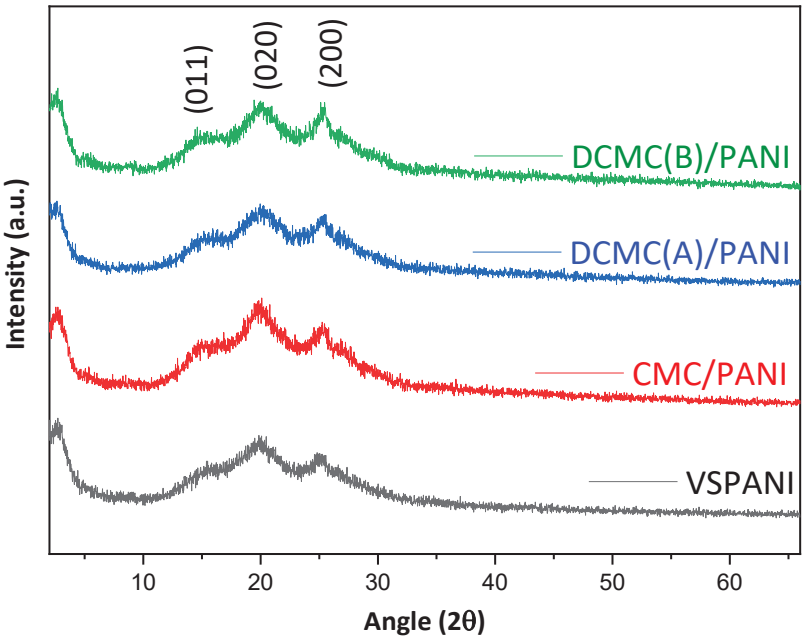

Figure 3.9: XRD patterns of VSPANI, PANI/CMC, PANI/DCMC(A) and PANI/DCMC(B)

3.3.2 Screening

3.3.2.1 Custom main effects screening design

The customised 16-experiment screening design compared with the default classical 12-experiment screening design was superior: the main effects and some interactions were uncorrelated to each other hence better accuracy in determining the active factors (Figure 3.10); optimal efficiency and average variance of prediction were also superior (Table 3.3); power (1-β), which averts type II errors (β) (Sullivan & Feinn, 2012), was also greater for the custom design. It is worth noting that adding 4 more runs to the classical design increases its power and frees some effects from correlation, but this is not straightforward, and the design remains inflexible to adjustments compared with the custom design.

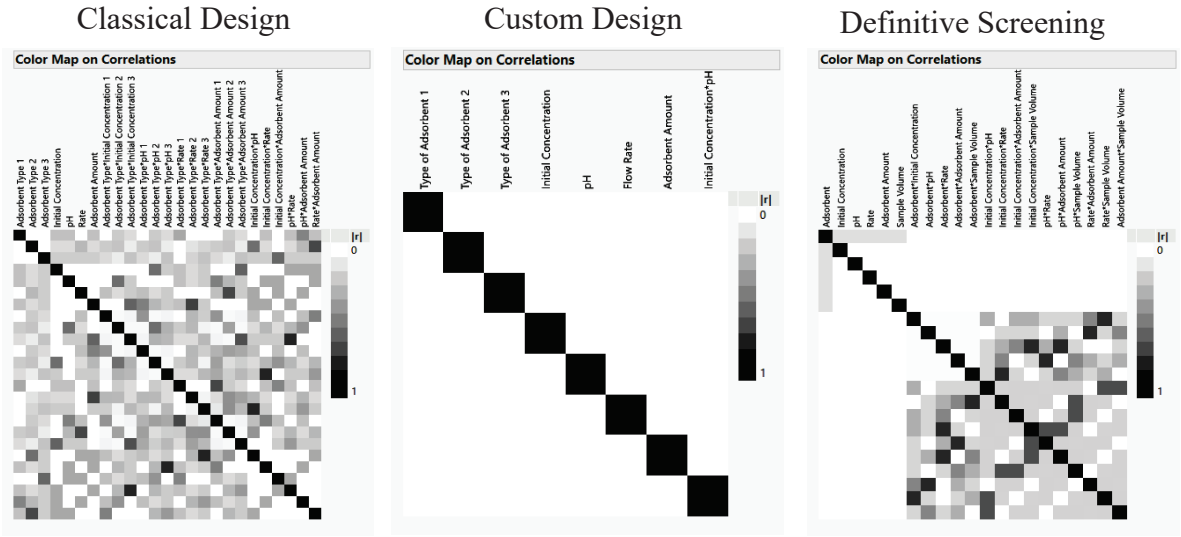

Figure 3.10: Coloured correlation maps for the main effects and interaction terms

Table 3.3: Experimental designs evaluation on optimal efficiency and power

Evaluation		Experimental Design		
		Classical	Custom	DSD
Experimental	Number of Factors	5	5	6
	Default Runs	12	16	18
Power Analysis	Intercept	0.74	0.94	0.97
	Adsorbent Type	0.29	0.53	0.96
	Initial Conc.	0.67	0.94	0.92
	pH	0.67	0.94	0.92
	Rate	0.69	0.94	0.92
	Adsorbent Amount	0.67	0.94	0.92
	Sample Volume	—	—	0.92
Alias Optimal Efficiency	D	93.67	100	82.59
	G	57.14	100	72.57
	A	86.49	100	81.15
Average Variance of Prediction		0.51	0.33	0.24

(DSD is definitive screening design, Conc.is concentration, — refers to not determined)

We fit the model based on the results in (Appendix I) and removed the interaction term between initial concentration and pH which had an insignificant effect to reduce the model (Table 3.4). The prediction profiler with maximised desirability (Figure 3.11) indicated that the use of 15 mg of villi-structured polyaniline and an initial BPA concentration of 70 mg/L at pH of 10 at a flow rate of 0.2 mL/min led to an optimal removal efficiency of 74% and an adsorption capacity of 96 mg/g (Table 3.4). The trends on the profiler show the effect of initial concentration and pH were larger for adsorption capacity with the effect of adsorbent amount larger for removal efficiency as evidenced by the *P* values. Only the type of adsorbent effect was significant across both responses while factors significant for removal efficiency were not significant for adsorption capacity and vice versa. These findings demonstrate the need to

optimise both responses simultaneously for a better picture of factor settings for maximum removal efficiency and maximum adsorption capacity.

Table 3.4: Effects summary and optimal settings for individual and combined responses.

Effect	*P*-Value		
	Removal Efficiency	*Adsorption Capacity*	*Combined Responses*
Adsorbent Amount	0.00002*	0.14462	0.00001*
Initial Concentration	0.65154	0.00005*	0.00005*
Type of Adsorbent	0.00026*	0.02217*	0.00018*
Flow Rate	0.02799*	0.62388	0.02584*
pH	0.70517	0.05260*	0.05137*
Initial Concentration*pH	0.73353	0.88727	0.73353
		Optimal Settings	
Desirability Value	0.89	0.76	0.73
Maximum Desirability	82.125%	108.679 mg/g	74.05% and 95.99 mg/g
Factor Settings	5 mg/L, pH 10, 0.2 ml/min & 15mg	70 mg/L, pH 10, 0.2 ml/min & 5mg	70 mg/L, pH 10, 0.2 ml/min & 15mg

(significant value at 95% confidence interval)*

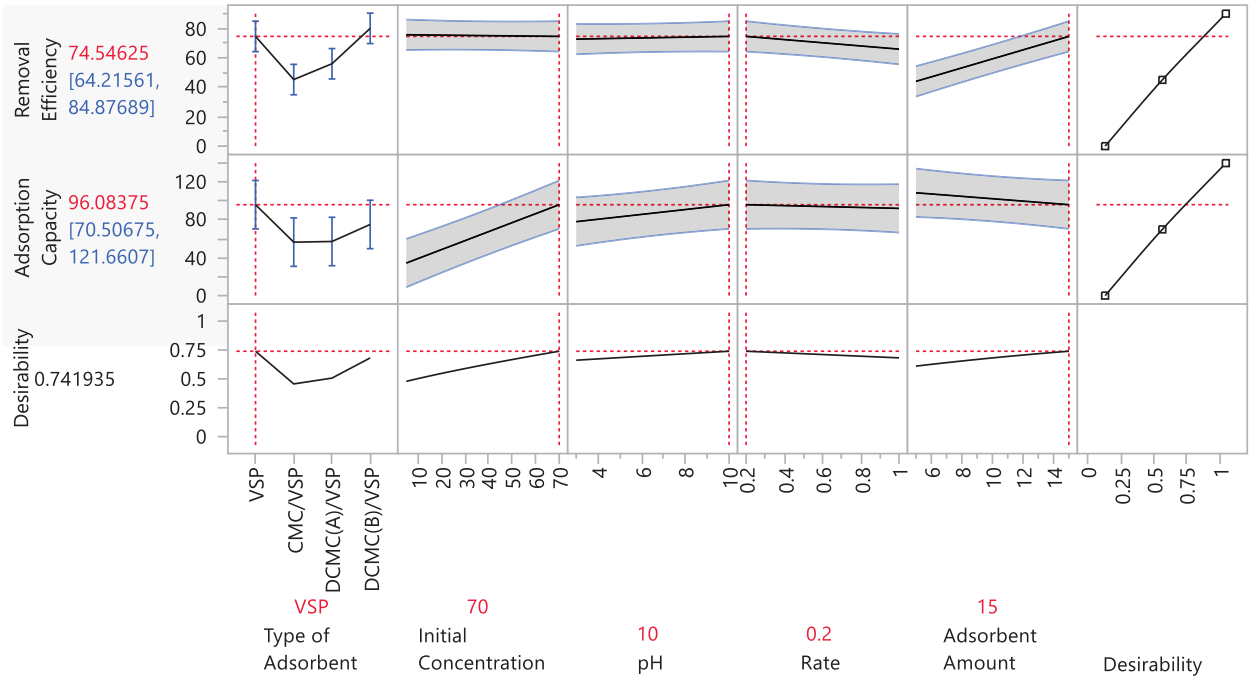

Figure 3.11: Prediction profiler for the custom design with desirability maximised.

3.3.2.2 Type of adsorbent (effect of aldehyde content)

VSPANI performed best closely followed by DCMC(B)/PANI and adsorption increased with an increase in the aldehyde content of the composites. The decrease in the hydrogen-bonding network indicates that the nitrogen species on the PANI chain plays a vital role in the adsorption of BPA rather than the additional carbonyl or hydroxyl groups which could have been in low quantities to have an effect. DCMC(B)/PANI with the least hydrogen-bonding density provided more N-H and some additional C=O, hence the highest removal efficiency—slightly

higher than VSPANI. As the villi structures become more defined in the composites, so does the adsorption capacity increase which could be because of the increased surface area that the villi structures provide.

3.3.2.3 Effect of initial concentration

At lower BPA concentrations the adsorbent's active sites were mainly unoccupied leading to higher removal rates but lower adsorption capacity. At higher concentrations, the collisions between molecules increased reducing mass transfer, and the concentration gradient between the adsorbent and adsorbate increased leading to the active sites being continuously filled hence a slight decrease in removal efficiency but an increase in adsorption capacity (Gusain et al., 2021).

3.3.2.4 Effect of pH

When the pH value of the BPA solution was below its pKa value of around 10.29, BPA adsorption on the adsorbents occurred through π-π non-electrostatic, hydrophobic, and hydrogen bonding interaction (Wang et al., 2019). As the pH increased to around BPA pKa's value, adsorption increased from the added electrostatic interactions between negatively charged ($-O^-$) on BPA and the protonated sections of polyaniline (Corrales et al., 2015; Rovani et al., 2020). These sorbents are attractive as they can maintain their properties over a wide pH range. It is worth mentioning that running the experiments at a pH higher than 11 recorded values of concentration higher than the initial concentration suggesting the possibility of PANI dissolving in highly alkaline media.

3.3.2.5 Effect of rate

Change in rate did not have a large effect on both removal efficiency and adsorption capacity, but a lower flow rate favoured both the removal efficiency and adsorption capacity due to the prolonged contact time between the adsorbents and BPA molecules. Flow rate is a major factor considered in fixed-bed adsorption (Patel, 2019); these adsorbents' attractiveness is magnified by being capable of quick equilibration—less than 20 minutes.

3.3.2.6 Effect of the amount of adsorbent

There were more available sites, higher surface area and longer interaction time when the amount of adsorbent increased leading to higher removal of BPA but reduced adsorption capacity due to these increased active sites being unoccupied (Al-Ghouti et al., 2007).

Selecting VSPANI and the five active factors for a response surface method would result in an inefficiently large number of experiments. Also, closer investigation of the differences between

VSPANI and DCMC(B)/PANI would be needed based on their small (0.3) and medium (0.6) Cohen's d effect sizes (Cohen, 1990) for removal efficiency and adsorption capacity (Table 3.5). This was the reasoning for selecting the definitive screening design after the main-effects custom design rather than heading directly to a response surface design. All the factors were included for an in-depth study of the main effects, 2-factor interactions, and quadratic effects using a definitive screening design.

Table 3.5: Cohen's d effect size for the type of adsorbent factor.

	VSPANI	**CMC/PANI**	**DCMC(A)/PANI**	**DCMC(B)/PANI**	
VSPANI	**0**	1.8	2.0	0.6	Adsorption Capacity
CMC/PANI	1.6	**0**	0.03	0.53	
DCMC(A)/PANI	0.9	0.5	**0**	0.5	
DCMC(B)PANI	0.3	1.8	1.3	**0**	
	Removal Efficiency				

3.3.2.7 Definitive screening design

We added 4 runs to the default 14-run definitive screening design to raise the power and improve its estimate for the main-linear and second-order quadratic effects. The experimental results (Appendix II) were fit on the definitive screening design using an effective model selection in two stages. The first stage identified the active main linear effects, and the second stage identified the second-order terms that only contained the active main effects (Table 3.6) —observing strong heredity (Jones & Nachtsheim, 2017). The statistically insignificant even-order terms for removal efficiency were included in the second stage since RMSE for stage 2 was larger than RMSE for stage 1 leading to a ratio that exceeded our specified threshold of one (SAS Institute Inc, 2017).

There lacked compelling evidence to suggest that the use of either VSPANI or DCMC(B)/PANI had a significant difference (P = 0.66); additionally, their Cohen's d-term effect sizes of 0.3 and 0.2 for removal and adsorption capacity were small (Cohen, 1990; Sullivan & Feinn, 2012). This confirmed our earlier hypothesis that the two adsorbents performed similarly (Fig. 7). As previously observed, a lower rate and a higher pH favoured the removal efficiency and adsorption capacity, but with increased sample size and power, the effect of varying the two was insignificant for both responses and adsorbents. Increasing the initial concentration, reducing the adsorbent amount, and increasing the sample volume significantly led to higher adsorption capacity while the inverse of these factor settings significantly led to higher removal efficiencies (Figure 3.12 and Table 3.6).

Table 3.6: Definitive screening design effects summary.

Effects Summary	Term	Removal Efficiency Prob>|t|	Adsorption Capacity Prob>|t|
Main Effects	x_2	0.0003*	<0.0001*
	x_5	<0.0001*	0.0003*
	x_6	0.0113*	0.0008*
	RMSE	3.6264	6.1673
Even-Order Effects	*Intercept*	0.0045*	<.0001*
	$x_2 \times x_5$	0.6936	0.0008*
	$x_2 \times x_6$	0.4226	0.0017*
	$x_5 \times x_6$	0.7699	0.0556
	$x_2 \times x_2$	0.2739	—
	$x_5 \times x_5$	0.1458	—
	$x_6 \times x_6$	0.8962	—
	RMSE	6.9036	4.7592

(significant values at a 95% confidence level; RMSE = Root Mean Square Error Prob>|t|= p-values)*

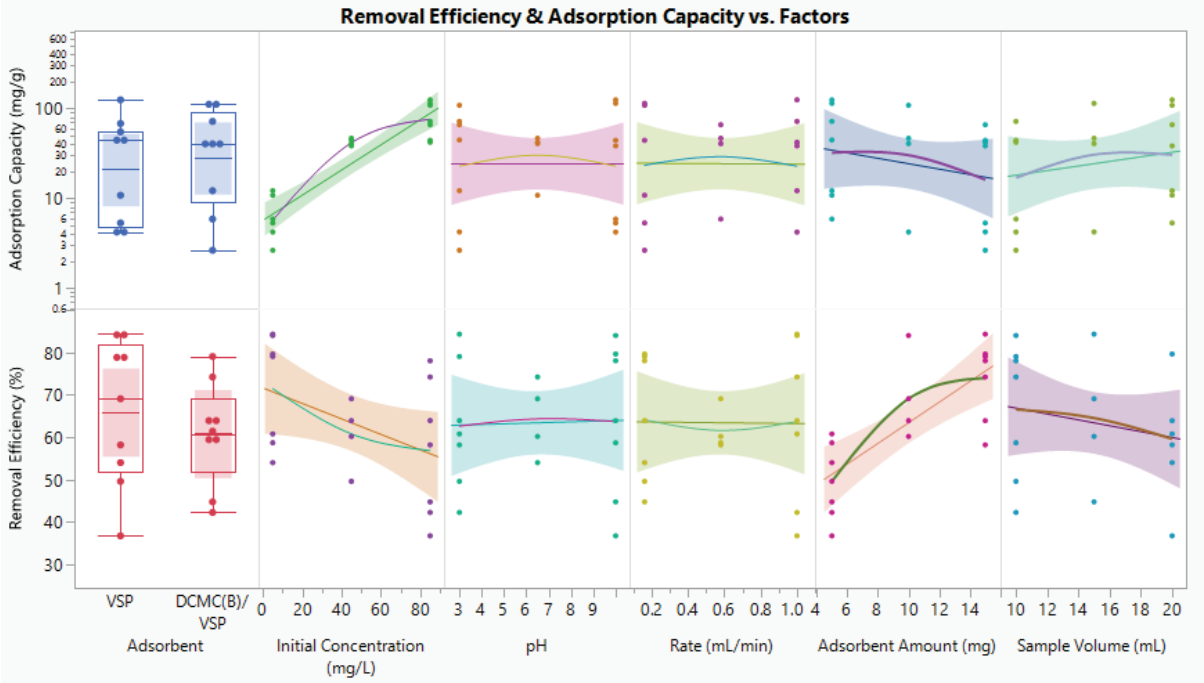

Figure 3.12: Definitive screening results for removal efficiency and log adsorption capacity represented as box plots for the type of adsorbent, and line graphs for the continuous factors with an additional smoother to show curvature for the factors.

The maximised desirability values for removal efficiency and adsorption capacity were 85.34% and 129.14 mg/g respectively when fit separately (Figure 3.13). DSD was able to account for curvature in initial concentration, adsorbent amount, and sample volume for removal efficiency specifying the need for a response surface model to optimise and fit in a second-order model. There was no need to augment the design with more runs as only three factors were active (Dougherty et al., 2014); therefore, we collapsed the definitive screening design to a response surface model to optimise the active factors and generate models for the two responses.

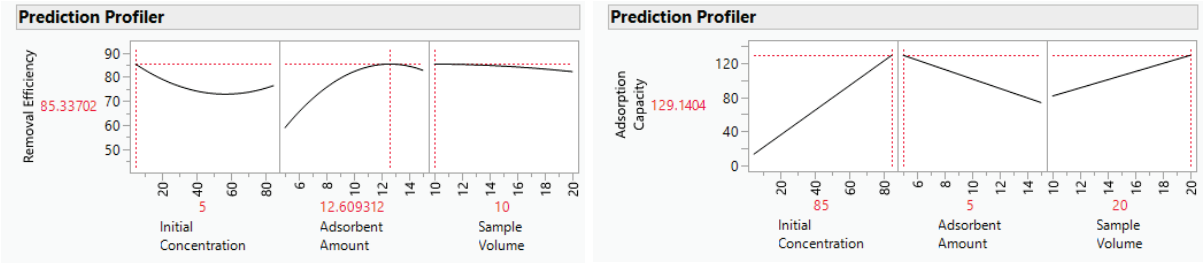

Figure 3.13: Prediction profilers from definitive screening for removal efficiency and adsorption capacity.

3.3.3 Response surface modelling and optimisation

We first log-transformed adsorption capacity guided by a Box-Cox transformation (Figure 3.14) to stabilise the variance for adsorption capacity. The observations were changing over a large order of magnitude (Figure 3.15) which would violate assumptions related to normality, homoscedasticity, and homogeneity of errors (Osborne, 2019).

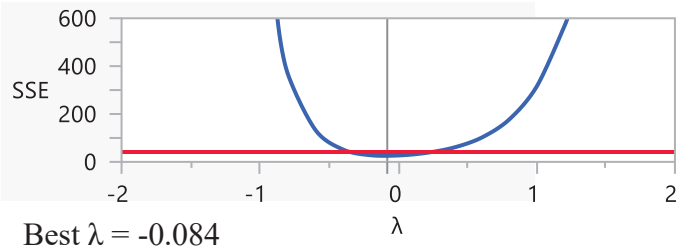

Figure 3.14: Adsorption Capacity Box-Cox Transformation

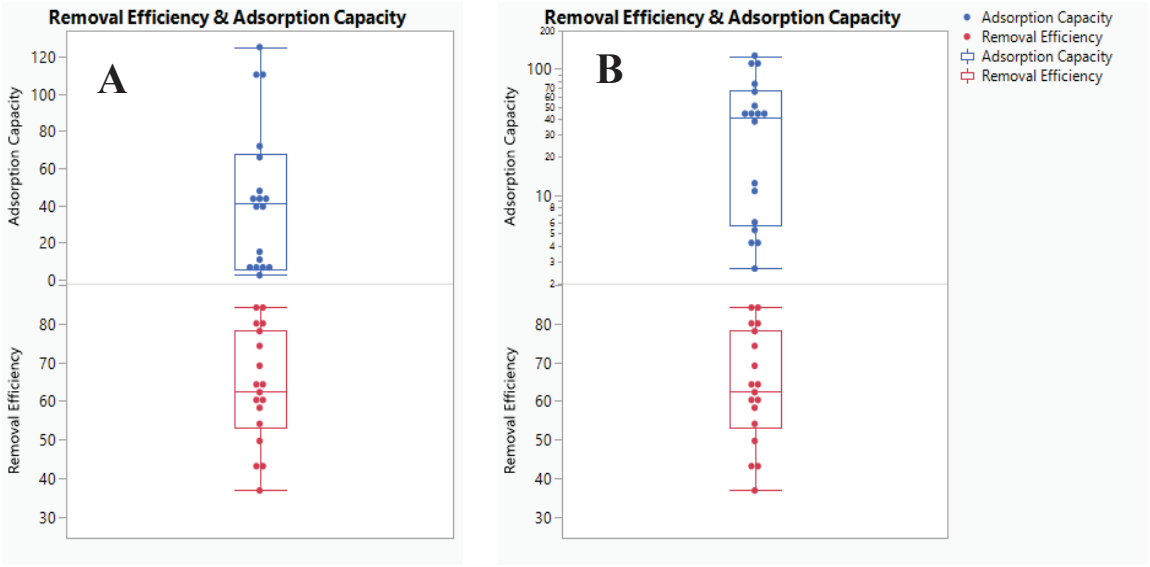

Figure 3.15: Box plots showing linear (A), and log-transformed adsorption capacity (B)

Only the adsorbent amount and sample volume interaction term from the three possible interactions with a large *P* value ($P = 0.61880$) and the smallest effect were dropped to reduce the model, avoid overfitting, and improve prediction (Hawkins, 2004). We maintained the

interactions and quadratic effects shown in Table 3.7 that had *P* values greater than 0.05—weak evidence against the null hypothesis (Goodman, 1999)—to avoid underfitting the models (Kvalheim et al., 2019); also, removing these insignificant second-order terms from the model did not improve the models any further.

Table 3.7: Response surface multi-response-model effects summary

Source	Effects	Parameter Estimate					
	Combined	Removal Efficiency			Log Adsorption Capacity		
	P value	β	Std error	Prob > |t|	β	Std error	Prob > |t|
Intercept	—	66.92	2.86	<.0001*	3.81	0.04	<.0001*
Initial Concentration (Conc.)	0.00000*	-7.37	1.19	0.0002*	1.29	0.01	<.0001*
Adsorbent (Ads) Amount	0.00000*	12.23	1.19	<.0001*	-0.34	0.01	<.0001*
Sample Volume (Vol)	0.00000*	-3.47	1.19	0.0175*	0.29	0.01	<.0001*
Initial Conc. × Initial Conc.	0.00000*	7.87	1.42	0.0217*	-0.67	0.04	<.0001*
Ads amount × Ads amount	0.00399*	-11.78	3.07	0.0040*	-0.05	0.05	0.2965
Sample Vol. × Sample Vol.	0.16399	-0.66	3.07	0.8350	-0.07	0.05	0.1640
Initial Conc. × Ads Amount.	0.08172	1.21	1.42	0.4186	0.04	0.02	0.0817
Initial Conc. × Sample Vol.	0.10604	-2.46	1.42	0.1188	-0.04	0.02	0.1060

(significant values at a 95% confidence level, β = regression coefficient)*

The model for adsorption capacity was a better fit based on the numerical adequacy checks (Table 3.8): RMSE was low and R^2_{adj} was comparable to R^2 (Kruger & Lewis-Beck, 2007). Both models were a good fit with the ability to explain 95% and 99% of the variation from the data used to fit the models as well as 80% and 95% of the variation in predicting removal efficiency and adsorption capacity respectively. The regression coefficients (β) in Table 3.7 were used to develop the simplified predictive models for removal efficiency (%RE, Eq. (3.5)) and adsorption capacity (q_{eq}, Eq. (3.6)).

Table 3.8: Numerical adequacy checks for the response surface model

	Components	Removal Efficiency	Log (Adsorption Capacity)
Summary of Fit	R^2	0.95	0.99
	R^2_{adj}	0.91	0.99
	RMSE	4.47	0.07
	PRESS R^2	0.80	0.99
Lack of Fit	F ratio	0.79	0.78
	Prod > F	0.63	0.63
ANOVA	F ratio	21.45	683.41
	Prob > F	<.0001*	< .0001*

*(*significant values at p=0.05, β = regression coefficient, R = Coefficient of determination, RMSE = Root Mean Square Error, PRESS = Predicted residual error sum of squares, ANOVA = Analysis of Variance)*

$$\%RE = 12.49 - 0.50x_2 + 11.60x_5 + 0.65x_6 + 0.005x_2^2 - 0.47x_5^2 - 0.03x_6^2 + 0.006x_2x_5 - 0.01x_2x_6 \quad (3.5)$$

$$q_{eq} = \exp\ (0.39 + 0.07x_2 - 0.04x_5 + 0.16x_6 + 0.0004x_2^2 - 0.002x_5^2 - 0.003x_6^2 + 0.0002x_2x_5 - 0.0002x_2x_6) \quad (3.6)$$

There were no violations related to assumptions related to linearity, equality of variance, and independence of errors as demonstrated in Figure 3.16: the residual followed close to a straight line in the normal quantile plots; the observations were randomly scattered around the centre line of zero in the residual plots with no obvious pattern, indicating equality of variance and independence over time; studentised residual plots showed lack of outliers since no data points were beyond the red lines (Montgomery, 2019).

The conditions for the simultaneous optimisation of both removal efficiency and adsorption capacity were 16.67 mL of 85 ppm BPA solution using an adsorbent amount of 10.65 mg resulting in 66.67% removal with an adsorption capacity of 87.16 mg/g (Figure 3.17). The surface plots (Figure 3.18) visualise the individual maximums considering two factors at a time: 85% removal efficiency using 11 mL of 5 mg/L BPA solution and 12 mg of adsorbent; 129 mg/g adsorption capacity using 20 mL of 80 mg/L BPA solution and 5 mg of adsorbent. The overall solutions to the equations defining the surface plots were a saddle point for removal efficiency and a maximum for adsorption capacity.

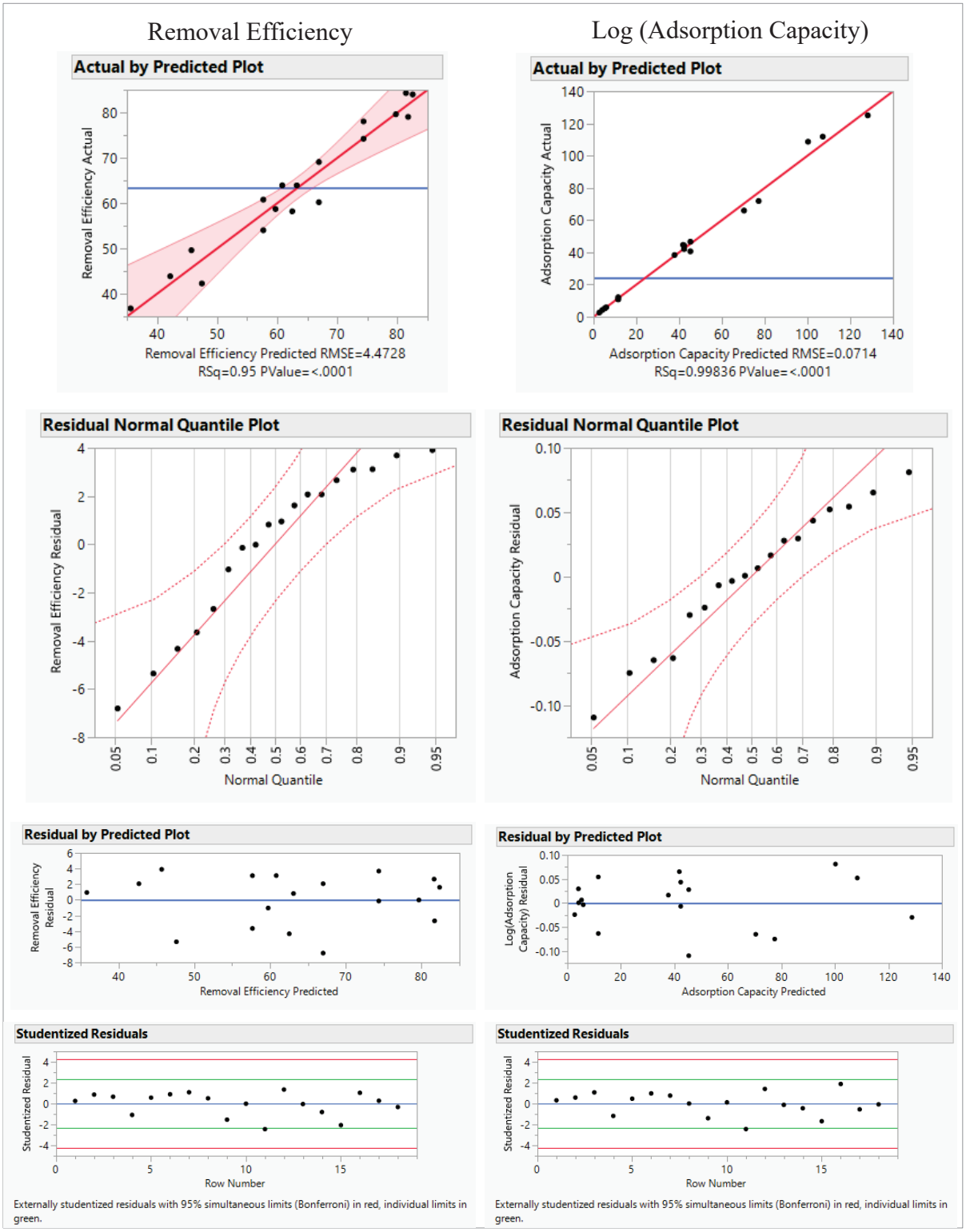

Figure 3.16: Response surface models' graphical adequacy checks for removal efficiency on the left and adsorption capacity on the right.

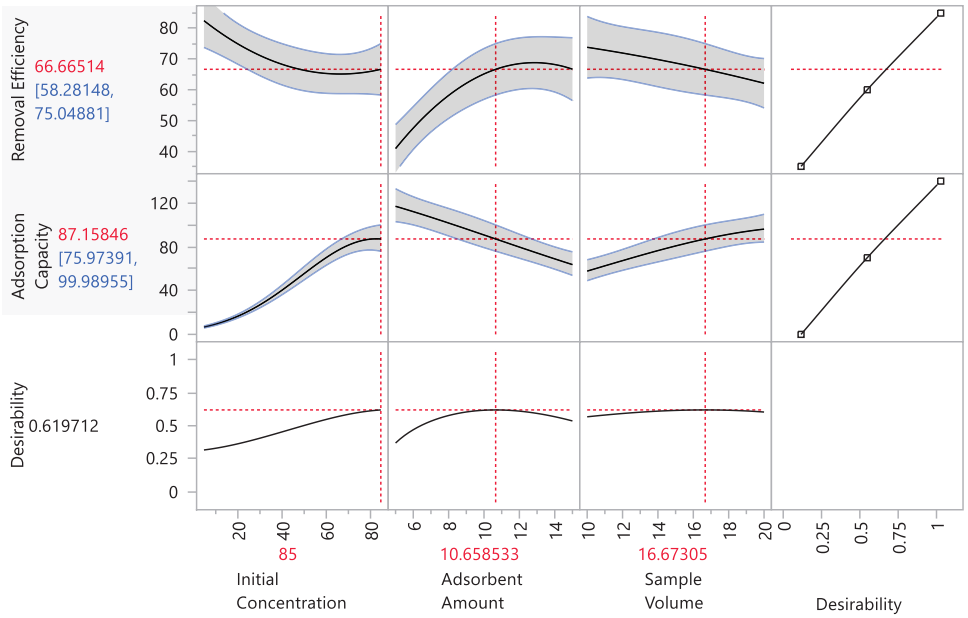

Figure 3.17: A multi-response prediction profiler for the response surface model with maximised desirability (shaded region shows the prediction range).

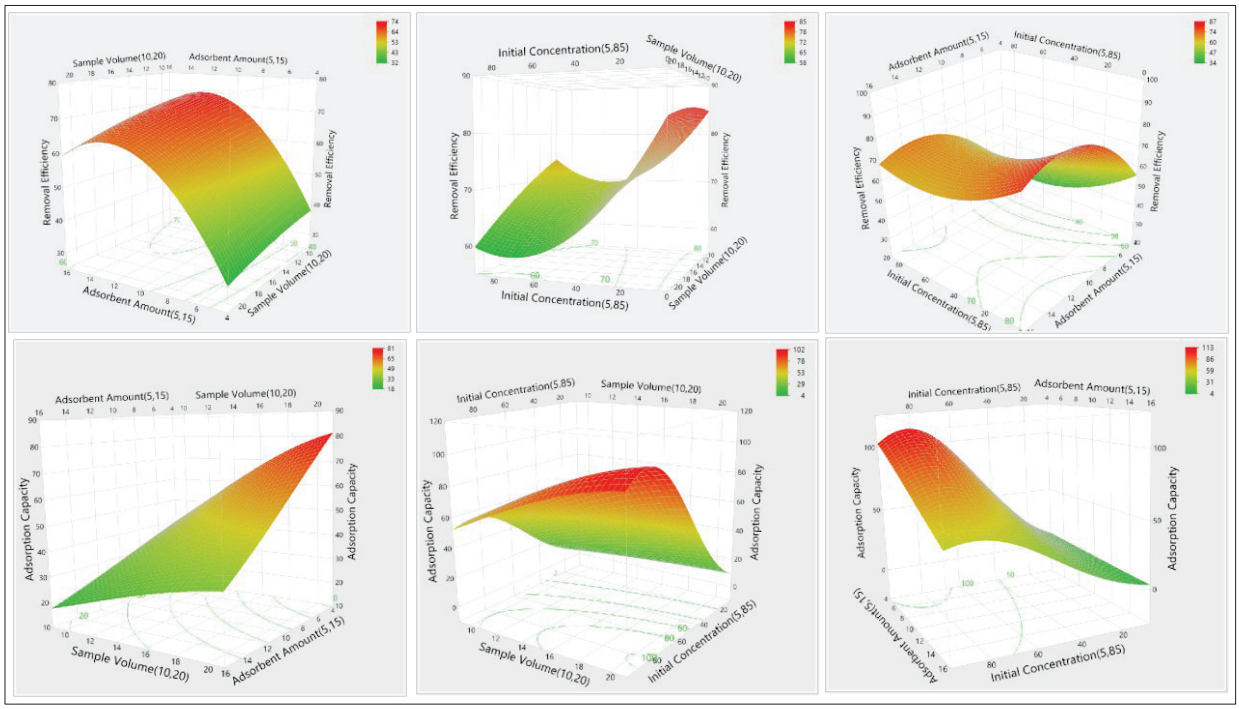

Figure 3.18: Response surface model surface plots with embedded contour plots showing the factor settings for maximum removal efficiency and adsorption capacity.

There were minimal variations between the predicted and experimental values for both responses from two validation experiments exemplifying the accuracy of the models (Table 3.9). Compared to other PANI-based adsorbents from literature (Table 3.10) and conventional polyaniline with a reported maximum removal efficiency of 40% and adsorption capacity of

22 mg/g for BPA (Hlekelele et al., 2019; Ouis et al., 2022), villi-structured polyaniline and DCMC(B)/PANI show remarkable adsorption performance.

Table 3.9: Differences between predicted and test-experimental values

Initial Concentration	Adsorbent Amount	Sample Volume	Removal Efficiency %		Adsorption Capacity mg/g	
x_2	x_5	x_6	Exp.	Pred. range	Exp.	Pred. range
25	10	10	63.51 ±10.97	66.93-81.39	15.87 ± 2.74	12.10-15.25
70	15	20	41.69 ± 2.96	54.11-67.75	116.73 ± 8.29	110.32-137.31

(Exp. = Experimental data as mean ± standard deviation where n = 2, pred. range = predicted range)

Table 3.10: Adsorption capacities of BPA on various adsorbents.

Adsorbent	q_{eq} (mg/g)	Reference
Conventional PANI	22.93	(Ouis et al., 2022)
Kieselguhr reinforce PANI (PANI@KG)	56.81	(Ouis et al., 2022)
Fe3O4@polyaniline core-shell	9.13	(Zhou et al., 2016)
Graphene oxide incorporated Fe_3O_4@polyaniline	14.43	(Zhou et al., 2017)
Fe_3O_4@SiO_2@polyaniline graphene oxide	454.56	(Zeeshan et al., 2021)
Villi-structured PANI	129	(This work)
DCMC(B)/PANI	129	(This work)

3.4 Conclusion

This chapter has described a sustainable method of experimentation where a total of six factors including a categorical variable in four levels—four adsorbents—were investigated using a customised and definitive screening design. This study used a total of 34 experimental runs to screen out initial concentration, adsorbent amount, and sample volume as the active factors. Changes in flow rate and pH had a small insignificant effect on removal efficiency and adsorption capacity. VSPANI performed remarkably well as an adsorbent for BPA with a high adsorption capacity (129 mg/g) compared to conventional PANI. The increase in aldehyde content favoured adsorption on the CMC-based composites, but there was no evidence to suggest that VSPANI differed in performance from DCMC(B)/PANI which had the highest aldehyde content.

We found that simultaneously optimising the responses was more practical due to the inverse and direct relationship of the factors towards either response. The models related to each response were graphically and numerically proven adequate with successful validation between

experimental and predicted values. We plan to use the optimal settings for the next chapter on studying the mass transfer properties from breakthrough curve analyses. One limitation of this study is that we only used one adsorbate, bisphenol A, to generalise the effect of aldehyde content. While other analytes might interact differently with these adsorbents, our study results still show that when using carboxymethyl cellulose as a composite or crosslinker for polymers, its oxidised species—dialdehyde carboxymethyl cellulose—and the aldehyde content should be considered.

Chapter 4: Adsorption of Bisphenol-A onto Villi-Structured Polyaniline: Fixed-Bed Breakthrough Curve Modelling Approach via Log-Modified, Fractal-Like, and Probability Distribution Function Models

4.1 Introduction

Fixed-bed adsorption is a popular method for the removal of water contaminants offering various advantages to batch reactors: it is relatively simple to develop with the capacity to regenerate the adsorbent; cost and time-effective; and by being a small-scale representation of real industrial fixed-bed reactors, it can be used for scaling and predictability purposes (Dichiara et al., 2015; Patel & In, 2021). The bulk of research in this area is focused on the synthesis of new and effective adsorbents whose adsorption behaviours are investigated through experimental breakthrough data from these bench-scale columns. The breakthrough curves are correlated to existing models to extract parameters such as rate constants, adsorption capacity, critical bed depth, breakthrough times and saturation times which are important for scaling to an industrial process.

Among these models: mechanism-driven models are the best but they require complex software and analytical skill to compute; data-driven models such as design of experiments—discussed in the 2nd chapter—or artificial neural network models have gained attention lately, but they are constrained by the experimental range used and cannot be used for prediction; the go-to models have been simple phenomenological or semi-mechanistic models such as the classic Bohart-Adams model (Bohart & Adams, 1920), Thomas model (Thomas, 1944), and Yoon-Nelson model which is purely empirical (Yoon & Nelson, 1984).

These simplified classical models are logistic functions assumed by an irreversible equilibrium and simple reaction kinetics. The time-independent reaction rate is assumed as the single curve-broadening factor that lumps together all other curve-broadening factors accounting for all mass transport properties. These models perform exceptionally well when modelling experimental breakthrough curves that are asymptotic, symmetrically S-shaped, and with a centrosymmetric point at 50% breakthrough (Chu, 2022). Alternatively, these models fail with asymmetric breakthrough curves from experiments where adsorption is diffusion-limited and on heterogeneous surfaces (Balsamo & Montagnaro, 2015). Given that models extract precise information only when they closely resemble the experimental data (Harter, 1984), there is a need for better models when it comes to modelling asymmetric breakthrough curves.

Though studies in the improvement of fixed-bed models remain lacking compared to studies in the synthesis of new adsorbents, some studies have modified these simple models to improve their fitting capabilities to asymmetrical data. Apiratikul and Chu logarithmically modified the simplified Bohart-Adams, Thomas, and Yoon-Nelson models and successfully tested these new models on breakthrough curves of varying symmetry (Apiratikul & Chu, 2021). Hu *et al* used fractal kinetics which regards the rate mechanism as a time-dependent factor to derive fractal-like modified models (Hu et al., 2019). Probability distribution functions whose cumulative distributions resemble breakthrough curves have also found use in breakthrough curve modelling. They have the advantage of flexible inflection points, which makes them suitable for simulating asymmetrical curves (Chu, 2021b). The functions include normal distribution (Chu & Hashim, 2022), Gompertz (Smith et al., 2012), and Weibull function (Chu, 2021a).

This chapter investigates and compares the trends of how these simplified, modified, and probability distribution models compare in fitting asymmetrical breakthrough curves whose degree of asymmetry is varied. The skewed breakthrough data were generated by varying the bed depth in the adsorption of bisphenol-A onto villi-structured polyaniline. In addition, the chapter discusses some modelling mistakes observed in recent publications such as using the same model expressed in different forms and using a variation of a model that erroneously deviates from the original—an issue also observed by other researchers (Chu, 2010, 2022; C. G. Lee et al., 2014). The conclusion and data from this study can be used in guiding fellow researchers in this field by providing information on which model would perform overall best in modelling breakthrough curves regardless of symmetry. To the best of our knowledge, there exists no study that puts together, investigates and compares the fitting performance of all these modified and probability distribution function models in the same study.

4.2 Methodology

4.2.1 Fixed-bed adsorption experiments and column characteristics

This experiment picks up from the previous chapter on the optimisation of adsorption-dependent factors using data-driven models—design of experiments. Here, the prepared villi-structured polyaniline was packed using a tap-fill method into glass microcolumns of 100 mm length, 6.7 mm outer diameter, and 5.5 mm inner diameter. The adsorbent was held between two quartz wool of 2-6 μ fibre diameter and glass beads used to fill in the space in the column after packing. The bed depth of the adsorbent was varied using different amounts of adsorbent: 6 mm (60 mg), 9 mm (90 mg), and 12 mm (120 mg) to get breakthrough curves with different shape characteristics for rich model comparisons. A peristaltic pump set at a constant flow rate of 1 mL/min was used to deliver 10 mg/mL bisphenol-A (BPA, ≥99% purchased from Nacalai tesque) as the influent and fractions of the effluent collected at a constant time interval for concentration analysis using a Shimadzu U-4100 UV-Vis spectrophotometer set at 276 nm. All the experiments were done at a constant room temperature of 25°C and a constant solution pH of 6.5.

4.2.2 Mathematical modelling of breakthrough curves

This study applies semi-mechanistic and empirical models to determine which breakthrough model best fits the experimental data with varying symmetry characteristics. We used popular simple models to correlate the data from fixed-bed studies: Bohart-Adams, Thomas, Yoon-Nelson, modified dose-response and Clark models. The logarithm and fractal kinetics modified models: log-Bohart-Adams, log-Thomas, log-Yoon-Nelson, fractal-like-Bohart-Adams, fractal-like-Thomas, fractal-like-Yoon-Nelson, and fractal-like-Clark were also fit to the same data and fitting capabilities compared with the unmodified versions. The strengths and weaknesses of probability distribution functions in correlating asymmetrical breakthrough curves were also investigated. To reduce clutter, all model parameters, symbol, variables, and their units are described in the nomenclature section.

4.2.2.1 Bohart-Adams model

This model was proposed by Bohart and Adams (Bohart & Adams, 1920) to describe the adsorption of chlorine on charcoal with the assumption of the rate of adsorption being proportional to the adsorbent's capacity. The simplified version of this model (Eq. (4.1)), derived by Amundson (Amundson, 1948; Chu, 2020c), was used to fit the breakthrough curves.

$$\frac{C}{C_0} = \frac{1}{1+\exp\left(k_{BA}\frac{N_0 Z}{U} - k_{BA}C_o t\right)} \tag{4.1}$$

The Log-Bohart-Adams model equation (Eq. (4.2)) was compared with the simplified Bohart-Adams model. It was derived by Apiratikul and Chu (Apiratikul & Chu, 2021) by defining a new set of parameters and variables equal to unity and reintroducing them into the Bohart-Adams model to make them logarithmic terms.

$$\frac{C}{C_0} = \frac{1}{1+\exp\left(k_{BA}\ln\left(\frac{N_0 Z}{U}\right)-k_{BA}\ln(C_0 t)\right)} \tag{4.2}$$

Fractal-like Bohart-Adams equation's (Eq. (4.3)) fitting capability was also compared with Bohart-Adams and log-modified Bohart-Adams model. Hu et al (Hu et al., 2019) derived this equation by making use of fractal kinetics (Eq. (4.4)) which regards the rate as a time-dependent factor using the fractal-like component (*h*).

$$\frac{C}{C_0} = \frac{1}{1+\exp\left(k_{BA,0}t^{-h}C_0\left(\frac{N_0 Z}{UC_0}-t\right)\right)} \tag{4.3}$$

$$k = k_0 t^{-h}\ (0 \le h \le 1) \tag{4.4}$$

4.2.2.2 Bed depth service time model

Bed Depth Service Time equations (BDST, Eqs. (4.5), (4.6) and (4.7)), derived by linearising and rearranging the simplistic Bohart-Adams (Eq. (4.1)), Log-Bohart-Adams (Eq. (4.2)), and Fractal-like-Bohart-Adams (Eq. (4.3)) models respectively. These BDST models were used to calculate the breakthrough time: defined as the time when the effluent concentration is at 5% of the influent concentration; and saturation time defined as the time when the effluent concentration is at 95% of the influent concentration (Saatci & Oulman, 1980).

$$t = \frac{N_0}{C_0 U}Z - \frac{1}{k_{BA}C_0}\ln\left(\frac{C_0}{C}-1\right) \tag{4.5}$$

$$t = \frac{N_0 Z}{C_0 U\left(\frac{C_0}{C}-1\right)^{\frac{1}{k_{BA}}}} \tag{4.6}$$

$$t = \frac{N_0}{C_0 U}Z - \frac{1}{kC_0}\ln\left(\frac{C_0}{C}-1\right) \tag{4.7}$$

4.2.2.3 Thomas model

This model proposed by Thomas model is based on a Langmuir equilibrium with the assumption of plug flow (Thomas, 1944). The simplified Thomas model (Eq. (4.8)); the log-modified model (Eq. (4.9)), derived by Apiratikul and Chu (Apiratikul & Chu, 2021) in a

similar way to the log-Bohart-Adams model; and the fractal-like modified Thomas model derived by (Hu et al., 2019) using the fractal-like kinetics (Eq. (4.4)) were fit to the experimental breakthrough curves and their fitting capabilities compared.

$$\frac{C}{C_0} = \frac{1}{1+\exp\left(k_T\frac{q_0M}{Q}-k_TC_ot\right)} \tag{4.8}$$

$$\frac{C}{C_0} = \frac{1}{1+\exp\left(k_T\ln\left(\frac{q_0M}{Q}\right)-k_T\ln(C_ot)\right)} \tag{4.9}$$

$$\frac{C}{C_0} = \frac{1}{1+\exp\left(k_{T,0}t^{-h}C_0\left(\frac{q_0M}{QC_0}-t\right)\right)} \tag{4.10}$$

4.2.2.4 Yoon-Nelson model

Yoon and Nelson proposed their model (Eq. (4.11)) by assuming a direct proportionality between the probability of a decrease in the rate of adsorbate adsorption to the probability of adsorbate adsorption and adsorbate breakthrough (Yoon & Nelson, 1984). Apiratikul and Chu derived the log-modified Yoon-Nelson model (Eq. (4.12)) in a comparable way to the log-Bohart-Adams model and Hu *et al* applied the fractal-like kinetics (Eq. (4.4)) to derive the fractal-like Yoon-Nelson model (Eq. (4.13)) (Apiratikul & Chu, 2021; Hu et al., 2019). These three models were fit to the experimental breakthrough data and their fitting capabilities were compared.

$$\frac{C}{C_0} = \frac{1}{1+\exp\left(k_{YN}(\tau-t)\right)} \tag{4.11}$$

$$\frac{C}{C_0} = \frac{1}{1+\exp(k_{YN}\ln\tau-k_{YN}\ln t)} \tag{4.12}$$

$$\frac{C}{C_0} = \frac{1}{1+\exp\left(\frac{k_{YN,0}}{1-h}\left(\tau^{(1-h)}-t^{(1-h)}\right)\right)} \tag{4.13}$$

4.2.2.5 Modified dose-response model

This model (Eq. (4.14)) was proposed by Yan *et al* who borrowed it from the Hill equation and adapted it to the Thomas model (Hill, 1910; G. Yan et al., 2016). This model was fit to the experimental data and its fitting capability compared to the log-modified Bohart-Adams model.

$$\frac{C}{C_0} = 1 - \frac{1}{1+\left(\frac{C_0Qt}{q_oM}\right)^{a_{Yan}}} \tag{4.14}$$

4.2.2.6 Clark model

Clark proposed this model (Eq. (4.15)) based on the Freundlich equilibrium while testing the adsorption performance of granular activated carbon in the removal of total organic carbon from water (Clark, 1987). Hu et al derived the fractal-like Clark model by introducing the fractal kinetics (Eq. (4.4)) which assumes a time-dependent mass coefficient factor (Hu et al., 2020). These two models were fit to the experimental data and their fitting characteristics were compared.

$$\frac{C}{C_0} = \left(\frac{1}{1+A\exp(-rt)}\right)^{\frac{1}{n_f-1}} \tag{4.15}$$

$$\frac{C}{C_0} = \left(\frac{1}{1+A_O\exp\left(-\frac{r}{1-h}t^{(1-h)}\right)}\right)^{\frac{1}{n_f-1}} \tag{4.16}$$

4.2.2.7 Probability distribution function models

As mentioned, since the probability distribution function models have characteristic sigmoidal shapes, here we investigate the fitting capabilities of the normal (Eq. (4.17)), Gompertz (Eq. (4.19)), and Weibull (Eq. (4.21)) functions to simulate experimental breakthrough curves of varying symmetrical characteristics. Also, the logarithm modified normal (Eq. (4.18)) and Gompertz function (Eq. (4.20)) were fit to the experimental breakthrough curves, compared with their unmodified versions and to the other probability distribution functions.

4.2.2.7.1 Normal and log-normal functions

The cumulative distribution function for the normal distribution, $F(x)$, is comparable to the quantity C/C_o (also ranging between 0 and 1), which enables the normal distribution to be rewritten as Eq. (4.17) where time is taken as the continuous variable regarding fixed-bed modelling (Chu & Hashim, 2022; Dima et al., 2020). Chu and Hashim derived the log-normal distribution Eq. 18 by first converting the variable t to a dimensionless quantity and introducing its distinctive fitting parameters a_2 and b_2 (Chu & Hashim, 2022). The normal and log-normal distribution functions were used to fit the experimental data and their fitting capabilities were compared with each other and with other probability distribution functions.

$$\frac{C}{C_0} = \frac{1}{2}\left[1+\operatorname{erf}\left(\frac{t-a_1}{b_1\sqrt{2}}\right)\right] \tag{4.17}$$

$$\frac{C}{C_0} = \frac{1}{2}\left[1+\operatorname{erf}\left(\frac{\ln(t)-a_2}{b_2\sqrt{2}}\right)\right] \tag{4.18}$$

4.2.2.7.2 Gompertz and Log-Gompertz function

The Gompertz model, proposed by Benjamin Gompertz (Gompertz, 1825) to correlate human mortality curves, was used in its commonly used form (Eq. (4.19)) to fit the experimental breakthrough curves. The log-modified version, Eq. (4.20), of this Gompertz model mentioned by Chu (Chu, 2020b) was also fit to the experimental data and the fitting capability compared to the unmodified model and other probability function models.

$$\frac{C}{C_0} = \exp[-\exp(a_3 - b_3 t)] \tag{4.19}$$

$$\frac{C}{C_0} = \exp[-\exp(a_4 - b_4 \ln(t))] \tag{4.20}$$

4.2.2.7.3 Weibull function

The Weibull function (Eq. (4.21)), discussed by Weibull as having the ability to fit asymmetrical frequency curves (Weibull, 1951), was also fit to the experimental breakthrough curves and fitting capability compared to other probability distribution function models.

$$\frac{C}{C_0} = 1 - \exp\left[-\left(\frac{t}{a_5}\right)^{b_5}\right] \tag{4.21}$$

4.2.3 Data analyses and nonlinear least square regression

All model fitting and parameter estimation were conducted using OriginPro 2021 software (OriginLab Corporation, Northampton, MA, USA). Nonlinear least square regression was applied to all models to approximate the parameters as linearisation of these equations leads to violations in regression assumptions and inaccurate parameter estimation (González-López et al., 2021; C. G. Lee et al., 2014). Method validation was measured through the adjusted coefficient of determination (Eq. (4.22)), root mean square error (RMSE, Eq. (4.23)), and reduced chi-square (χ^2, Eq. (4.24)). The goodness-of-fit was gauged by checking for larger R^2_{adj}, smaller RMSE and smaller $Reduced\ \chi^2$values.

$$R^2_{adj} = \left[1 - \left[1 - \left(\frac{\sum_{i=1}^{n}(y_e - \bar{y}_e)^2 - \sum_{i=1}^{n}(y_e - y_c)^2}{\sum_{i=1}^{n}(y_e - \bar{y}_e)^2}\right)\left(\frac{n-1}{n-p}\right)\right]\right] \tag{4.22}$$

$$RMSE = \sqrt{\frac{\sum_{i=1}^{n}(y_e - y_c)^2}{n}} \tag{4.23}$$

$$Reduced\ \chi^2 = \frac{1}{f}\sum_{i=1}^{n}\frac{(y_e - y_c)^2}{y_c} \tag{4.24}$$

Bayesian information criterion (BIC, Eq. (4.25)) was used for a fair comparison of models that had different numbers of fitting parameters (Schwarz, 1978). We chose the BIC criterion over

Akaike information criterion (AIC) because it harshly penalises a model with more parameters. The model with lower BIC values was considered a better model.

$$BIC = n \ln\left(\frac{SSE}{n}\right) + p \ln n + n \ln(2\pi) + n \tag{4.25}$$

4.3 Results and Discussion

4.3.1 Experimental breakthrough curves

The breakthrough curves from experimental data (Figure 4.1) were characterised by an immediate breakthrough of bisphenol A, a sharp rise in the concentration, and a slow approach to saturation. The breakthrough time increases with an increase in bed height because the total amount of the adsorbent present in the column increases resulting in a longer distance for adsorption to occur. The curves are all asymmetrical characterised by a tailing shape—a slow approach of c/c_0 towards unity. This slow approach to saturation and broadening of the curves at the onset of breakthrough suggests an inadequate utilisation of the column capacity as bed depth increases.

The asymmetry of the breakthrough curves results from a broad sorption zone consequence of the heterogeneous particle size distribution, axial dispersion, reduced adsorption rate from steric blocking at a high adsorbent surface coverage, slow intraparticle diffusion, and slow diffusion on the surface: a feature contrast to particle-mass-transfer or external mass-transfer-resistance controlled systems (Chu, 2004; Cooney, 1991; Ernest et al., 1997; Jin et al., 1994). The low adsorption capacity and the heterogenous surface of villi-structured polyaniline—demonstrated in the previous chapter—coupled with data in this study, suggests that the intraparticle diffusion flux would be lower than the pore diffusion flux hence a tailed curve with an early breakthrough. This is mainly because the surface concentration gradient has

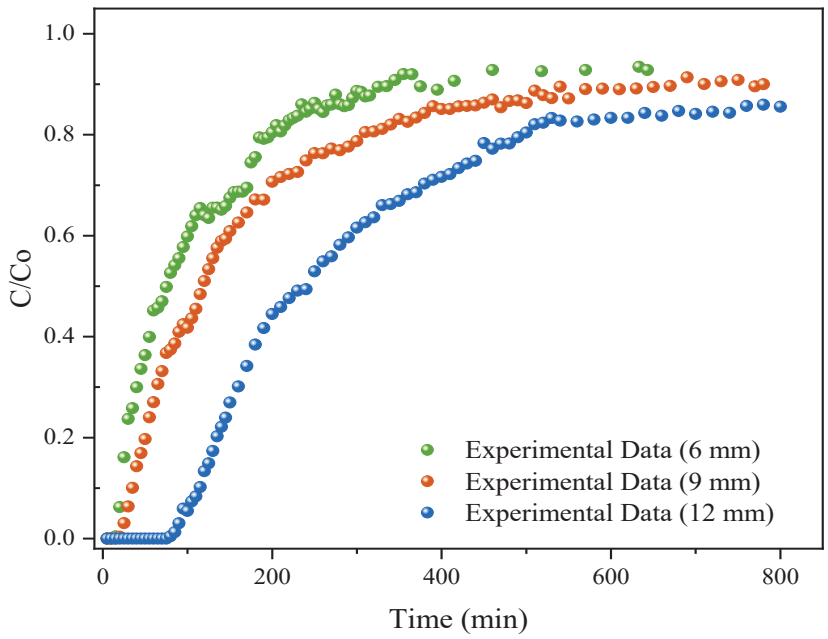

Figure 4.1: Breakthrough curves from experimental data with the bed depth varied: 6 mm, 9 mm, and 12 mm.

already reached its limit during the progressive occupation of the active sites in the nonlinear isotherm region because of the limited adsorption capacity of the adsorbent (Ma et al., 1996). Simple semi-mechanical models such as the Bohart-Adams and Thomas model that lump together all mass-transfer parameters into one time-independent rate factor would perform poorly and give erroneous parameter estimates in correlating such asymmetrical breakthrough curves.

4.3.2 Bohart-Adams model

The findings confirm the hypothesis of the simple Bohart-Adams model's underperformance in trying to simulate the experimental breakthrough data with a degree of tailing (Figure 4.2): it overestimates both saturation and breakthrough times, estimates erroneous parameters, and reports a nonzero effluent concentration ($C_{t(0)}$) at t = 0 which is illogical (Table 1). The residuals also suggest that the simple Bohart-Adams model violates regression assumptions of equality and independence of variance.

4.3.2.1 Log-modified Bohart Adams model

Applying the log-modified Bohart-Adams model improved the fitting capability of the model compared to the simplistic model: adjusted coefficients of determination values were higher; values for reduced chi-square values and RMSE were lower, and the models reported zero effluent concentration at t = 0 for all bed depths (Figure 4.2 and Table 4.1). The saturation and breakthrough times, defined by Eq. (4.6), were comparable with the experimental data, but the log-Bohart-Adams models tend to deviate from the experimental breakthrough curves as the extent of tailing increases. The success of this log-modified model is based on its inflection point's dependency on the rate coefficient (k_{BA}) defined by Eq. (4.26) (Apiratikul & Chu, 2021); conversely, this relationship is also the reason this model fails in adapting to asymmetry as tailing increases. The calculated inflection points were 0.14, 0.15, and 0.25 for the 6 mm, 9 mm, and 12 mm bed depth, respectively. As the rate coefficient value increases with increased tailing, the position of the inflection point shifts toward $C/C_0 = 0.5$, which explains the observed strain in simulating the asymmetry of strongly tailed data.

$$\frac{C}{C_0} = \frac{k_{BA}-1}{2k_{BA}} \tag{4.26}$$

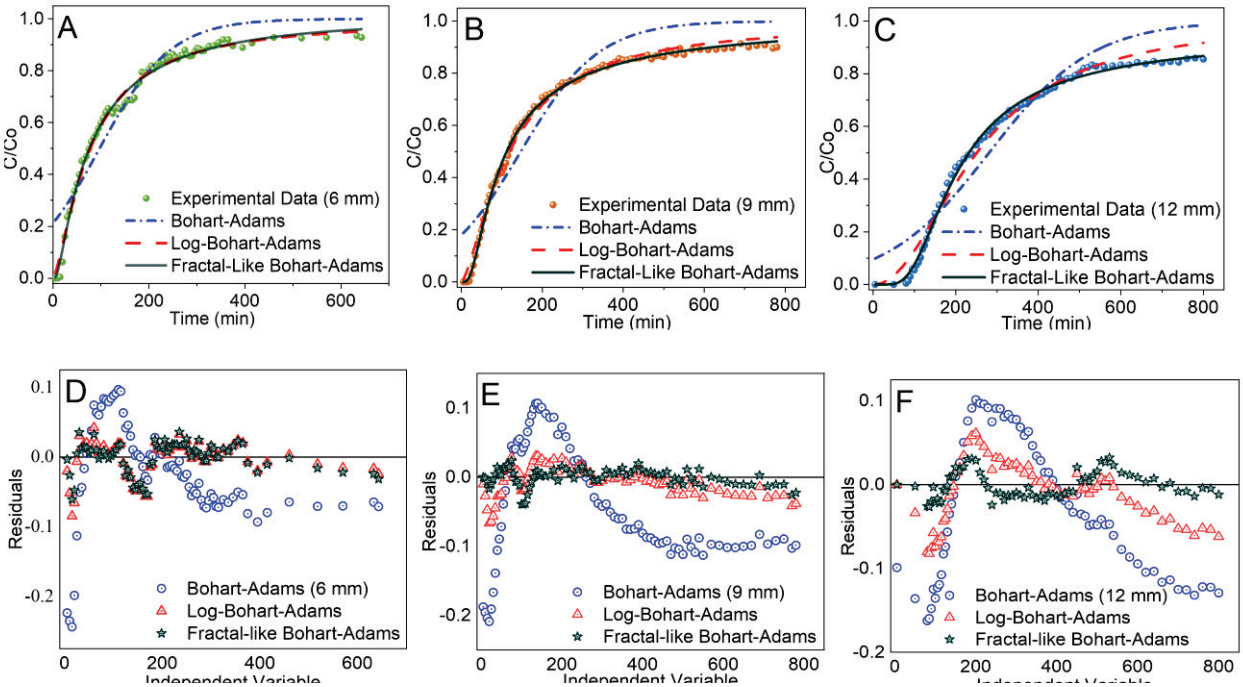

Figure 4.2: Breakthrough curves with the bed depth varied and the accompanying residual plots for each: 6mm (A&D), 9 mm (B&E), 13 mm (C&F).

4.3.2.2 Fractal-like Bohart-Adams model

The fractal-like modified Bohart-Adams model was best overall in simulating the breakthrough data regardless of asymmetry (Figure 4.2). The adjusted coefficients of determination were the highest while, reduced chi-square and RMSE values were the lowest (Table 4.1). Also, even though the model includes an additional fitting parameter, its BIC values were the lowest suggesting an appropriate model. Unlike the log-Bohart-Adams model, the fractal-like model fitting was unaffected with increased tailing. The breakthrough and saturation times, size of the mass transfer zone (MTZ), critical bed depth, and other parameters estimated by this fractal-like-Bohart-Adams model reflect the actual experimental data. The fitting performance of this fractal-like model is related to the introduction of the adjustable parameter (h), which also served as an indicator of asymmetry from a diffusion-limited process when $h \neq 0$ (Hu et al., 2021); the greater the deviation of h towards unity, the more the asymmetry (Table 3.1).

The size of the mass transfer zone (MTZ, Eq. (4.27)), defined as the length of bed required for sorption (Crittenden et al., 1986), increases with an increase in bed depth (Table 3.1). Being that the shape of the breakthrough curve is determined by the size of MTZ, the observed broadening of the sorption zone with the increase in bed depth suggests a diffusion-limited

process (Nijhawan et al., 2020). We extrapolated the critical bed depth values (Z_0)—defined as the minimum bed depth required to get a breakthrough—from the breakthrough time against the bed-depth plot in the supplementary information (Figure 4.3). As expected, the Bohart-Adams model underestimates Z_0 due to its inability to correlate asymmetrical data. The fractal-like Bohart-Adams model estimates a more accurate critical bed depth of 5.65 mm.

$$MTZ = Z \times \left(1 - \frac{t_{break}}{t_{saturation}}\right) \tag{4.27}$$

Table 4.1: Comparison of parameters and statistical validation for Bohart-Adams, log-Bohart-Adams, and fractal-like Bohart-Adams model

Model	**Bohart-Adams**			**Log-Bohart-Adams**			**Fractal-like Bohart-Adams**		
Z (mm)	6	9	12	6	9	12	6	9	12
$R^2_{adj.}$	0.906	0.888	0.911	0.989	0.993	0.982	0.991	0.998	0.997
Reduced $\boldsymbol{\chi^2}$	0.006	0.009	0.007	0.0007	0.0005	0.0014	0.0005	0.0001	0.0002
RMSE	0.075	0.093	0.085	0.025	0.022	0.037	0.023	0.013	0.016
BIC	-148	-486	-114	-313	-716	-228	-324	-806	-345
$\boldsymbol{k_{BA}}$ *(L mg^{-1}min^{-1})*	0.0013	0.0010	0.0008	1.415	1.448	2.079	0.019*	0.031*	0.091*
h	0	0	0	0	0	0	0.547	0.663	0.840
$\boldsymbol{N_0}$ *(mg L^{-1})*	8254	8306	11919	6592	6731	10665	6442	6336	9848
$\boldsymbol{q_0}$ *(mg g^{-1})*	16.17	16.31	23.40	12.94	13.21	20.94	12.64	12.44	19.34
$\boldsymbol{\tau}$ *(min)*	97	146	281	77	119	251	75	112	232
$C_{t(0)}$ *(mg L^{-1})*	2.1	0	0	1.8	0	0	1.0	0	0
t_{break} (min)	16	24	54	10	16	61	13	26	90
$t_{saturation}$ (min)	315	432	604	367	442	602	366	488	554
MTZ (cm)	0.57	0.85	1.09	0.58	0.87	1.08	0.58	0.85	1.00
Z_0 (mm)	4.05			5.59			5.65		

(* units for $k_{BA,0}$ (*L mg^{-1}min$^{-(1-h,)}$* $C_{t(0)}$ = concentration at time zero, MTZ = Mass Transfer Zone)

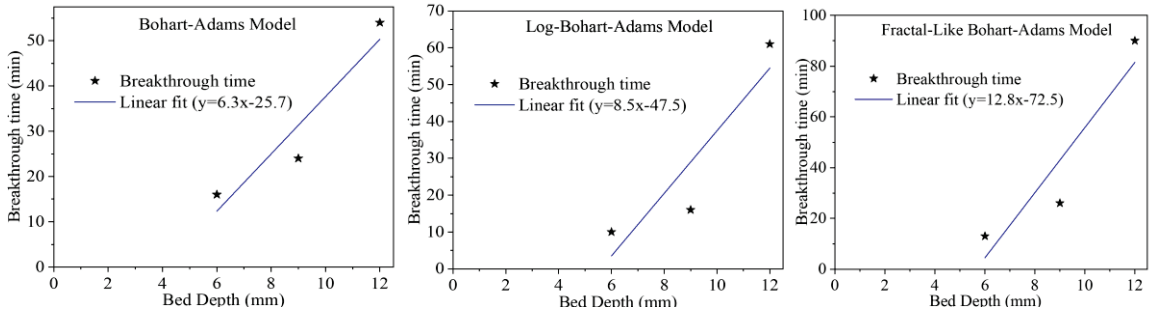

Figure 4.3: Bead Depth Service Time (BDST) plots for simplistic, log-modified, and fractal-like modified Bohart-Adams model using 10 mg L^{-1} concentration

4.3.3 Misconceptions

A troubling concern in this research area of removal of pollutants from water using fixed-bed columns is the misconception that the simple Bohart-Adams, Thomas, and Yoon-Nelson

models are different models. In such cases, researchers end up fitting these three models to the same data and comparing their fitting capabilities. Though studies have highlighted this issue (Chatterjee & Schiewer, 2011; Chu, 2010, 2020a; Lee et al., 2014; Pérez-Calderón et al., 2023), it continues to ail publications in this field as shown but not limited to the following recent publications sampled from google scholar (Agi et al., 2023; Medha et al., 2023; Vijuksungsith et al., 2023). Here we also voice a similar concern by showing that indeed these three simplified models are mathematically equivalent; the plots related to the three simplified models, their log-modified and fractal-like versions lead to superimposed curves with similar model parameters (Figure 4.4 and Table 4.2). Therefore, the simplified Bohart-Adams models can generate parameters related to the Thomas model: k_T and q_0 using Eqs. (4.28)&(4.29), and Yoon-Nelson model: k_{YN} and τ using Eqs. (4.30)&(4.31) (Chu, 2010; C. G. Lee et al., 2014). Likewise, their modified versions are also related similarly.

$$k_T = k_{BA} \tag{4.28}$$

$$q_0 = \frac{N_0 Z S}{1000m} \tag{4.29}$$

$$k_{YN} = k_{BA} C_0 \tag{4.30}$$

$$\tau = \frac{N_0 Z}{C_0 U} \tag{4.31}$$

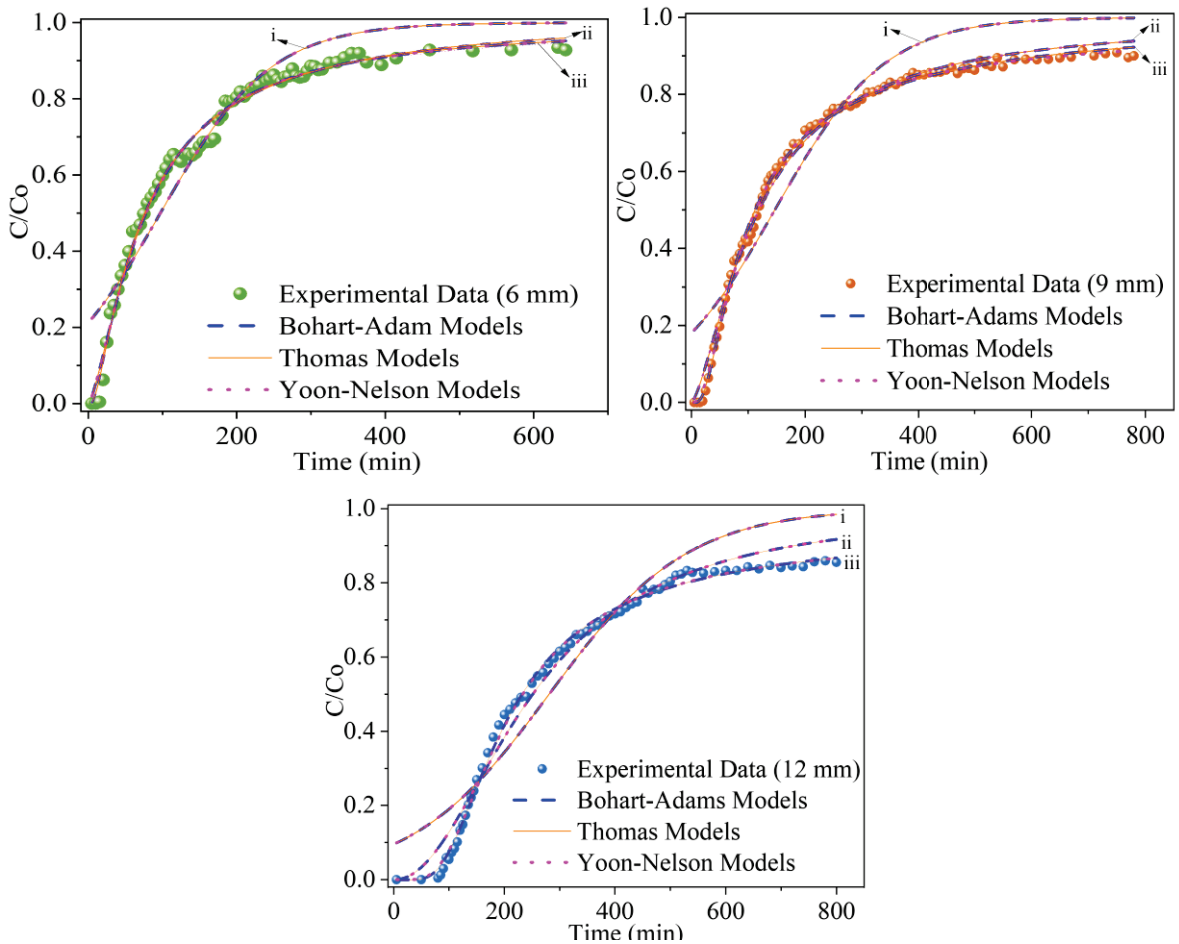

Figure 4.4: Comparison between Bohart-Adams, Thomas, and Yoon-Nelson models: (i) Simplistic models, (ii) log-modified models, and (iii) fractal-like models

Table 4.2: Parameters and statistical validation for simplistic Thomas and Yoon-Nelson models, log-modified Thomas and Yoon-Nelson models, and fractal-like Thomas and Yoon-Nelson models

Model	**Thomas**			**Log-Thomas**			**Fractal-like Thomas**		
Z (mm)	6	9	12	6	9	12	6	9	12
$R^2_{adj.}$	0.906	0.889	0.911	0.989	0.993	0.983	0.991	0.998	0.997
Reduced $\boldsymbol{\chi^2}(\times \mathbf{10^3})$	5.77	8.77	7.48	0.65	0.54	1.47	0.54	0.17	0.25
RMSE	0.075	0.093	0.085	0.025	0.023	0.037	0.023	0.013	0.016
BIC	-148	-127	-114	-313	-357	-224	-329	-453	-345
$\boldsymbol{k_T}$ *(L mg^{-1}min^{-1})*	0.0014	0.0010	0.0008	1.415	1.448	2.079	0.019*	0.031*	0.091*
h	-	-	-	-	-	-	0.55	0.66	0.84
$\boldsymbol{q_0}$ *(mg g^{-1})*	16.17	16.31	23.40	12.94	13.22	20.94	12.65	12.44	19.34
Model		Yoon-Nelson			Log-Yoon-Nelson			Fractal-like Yoon-Nelson	
Z (mm)	6	9	12	6	9	12	6	9	12
$R^2_{adj.}$	0.906	0.889	0.911	0.989	0.993	0.983	0.989	0.998	0.997
Reduced $\boldsymbol{\chi^2}(\times \mathbf{10^3})$	5.77	8.77	7.48	0.65	0.54	1.47	0.65	0.15	0.28
RMSE	0.075	0.093	0.085	0.025	0.023	0.037	0.025	0.012	0.016
BIC	-165	-144	-127	-331	-375	-240	-333	-480	-355
$\boldsymbol{k_{Y-N}}$ *(min^{-1})*	0.014	0.010	0.008	1.42	1.45	2.08	1.79*	5.36*	68.15*
h	-	-	-	-	-	-	1.05	1.26	1.63
$\boldsymbol{\tau}$ *(min)*	97	147	281	78	119	251	77	113	233

(* units for $k_{T,0}$= *L mg^{-1}min$^{-(1-h)}$,* and $k_{Y-N,0}$ = *min$^{-(1-h)}$*)

Another common misconception is the misuse of a version of Bohart-Adams equation often referred to as Adam-Boharts model (Eq. (4.32)), sometimes represented by its linearised version (Eq. (4.33)). Studies have reported the use of this equation to be incorrect (Chu, 2020a, 2020c; Hu & Zhang, 2020; Lee et al., 2014); in contrast to the converging logistic Bohart-Adams model (Eq. (4.1)), it is an exponential function that expresses a diverging type of model. We also show in the supporting information (Figure 4.5) that such a diverging model is unfit for use in modelling the whole breakthrough region and would only work in fitting the initial portion of the breakthrough curves. It is without a doubt that researchers who may unknowingly use this "Adam-Boharts" model, end up reporting poor correlation results (Gizaw et al., 2022; Oyekanmi et al., 2021; Pap et al., 2020; C. Xu et al., 2023; Yeo et al., 2023).

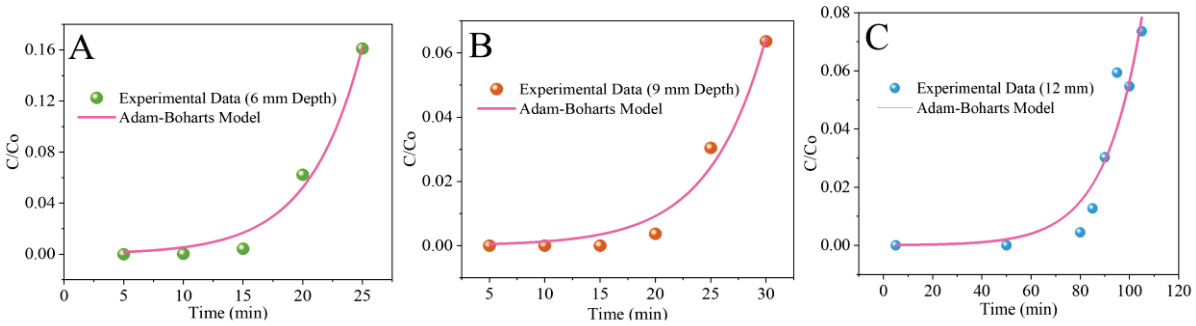

Figure 4.5: "Adam-Boharts" model fit for initial breakthrough data

$$\frac{C}{C_0} = \frac{1}{\exp\left(k_{BA}\frac{N_0 Z}{U} - k_{BA}C_o t\right)} \tag{4.32}$$

$$\ln\left(\frac{C}{C_0}\right) = k_{BA}\frac{N_0 Z}{U} - k_{BA}C_o t \tag{4.33}$$

There is also confusion whereby some studies use the BDST equation as an independent model to the extent of notating its rate coefficient differently e.g. k_{BDST}, k_{α} (Banza & Rutto, 2022; Chakraborty & Naskar, 2022; Mahmoud et al., 2022; H. Singh et al., 2022; J. Wang et al., 2022); in some cases, researchers even unknowingly compare the "BDST model" and Bohart-Adams model in the same work (Kulkarni et al., 2022; Szostak et al., 2022). It should be noted that the BDST equations (Eqs (4.5) - (4.7)) are simply rearranged and linearised versions of Bohart-Adams equations (Eqs (4.1), (4.2), and (4.3)) and should not be mistaken as independent models.

4.3.4 Modified dose-response model

It is worth noting here the similarity between the log-Bohart-Adams model ((4.2)), which when rewritten as Eq. (4.34) by Apiratikul and Chu (2021), looks similar to the modified dose-response model (Eq. (4.14)). Yan *et al.* derived this dose-response model by adopting the Thomas model to an equation used in modelling oxygen binding to haemoglobin by Hill (Hill, 1910; G. Yan et al., 2016). Comparing the two: log-Bohart-Adams and modified dose-response models were superimposed, they estimated equal parameter values, and both deviated from experimental data as the extent of tailing increased (Figure 4.6 and Table 3.1). Undoubtedly, the dose-response model will always be superior to Bohart-Adams, Thomas and Yoon-Nelson models in studies where combinations of these models are used to describe asymmetric breakthrough curves (Boutaleb et al., 2022; de Araújo et al., 2022; Qin et al., 2023; Shields et al., 2022). Yan built the model upon the Hill equation by retaining the empirical parameter (a_{Yan}) and dropping the rate constant (k_t) related to Thomas model. Since the log-Bohart-Adam model—or rather the equivalent log-Thomas model—introduces no new parameters and still contains the rate constant, it is preferable to the modified dose-response model (Apiratikul & Chu, 2021). BIC values for the modified dose-response model were slightly lower because the criterion penalises log-Bohart-Adams for having additional fitting parameters.

$$\frac{C}{C_0} = \frac{1}{1+it^{-d}} \tag{4.34}$$

$$\text{where } i = \left(\frac{N_0 L}{C_0 u}\right)^{k_{BA}};\ d = k_{BA} \tag{4.35}$$

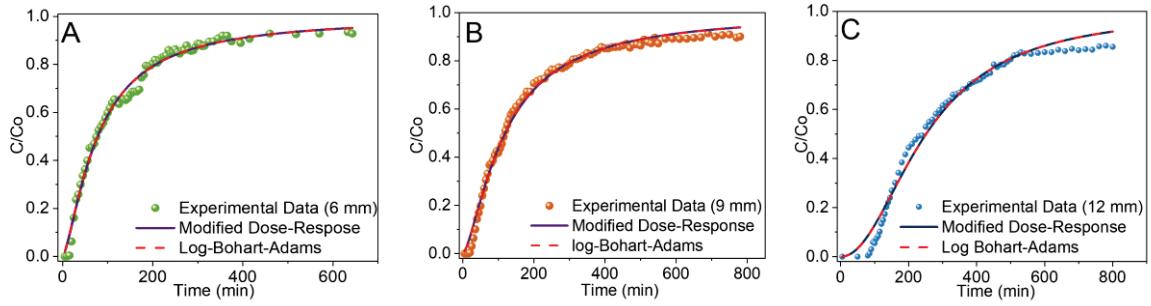

Figure 4.6: Comparison of fitting quality of modified dose-response model and log-Bohart-Adams models with varied bed depth

Table 4.3: Parameters obtained from the modified dose-response model

	Modified Dose-Response Model		
Bed depth (mm)	6	9	12
$\boldsymbol{BIC}$	-326	-370	-240
$\boldsymbol{a_{Yan}}$	1.415	1.448	2.079
$\boldsymbol{q_{Yan}(mg\ g^{-1})}$	12.94	13.21	20.94

4.3.5 Clarks model

Clarks model performed poorly in correlating the asymmetrical experimental breakthrough data ($R^2_{adj} < 0.92$) and deviated further from the experimental data with increased tailing (Fig. 4 and Table 3). This is because it is a logistic function designed by assuming an irreversible equilibrium in the adsorption of adsorbate molecules in a random homogeneous manner (Clark, 1987). The fractal-like Clark model outperformed the Clark model as validated by the higher adjusted coefficients of determination; lower RMSE and reduced chi-squared, and lower BIC values (Table 3). Treating the mass-transfer coefficient of the Clarks model as a time-dependent factor enabled the model to fit the breakthrough curves regardless of symmetry (Hu et al., 2020).

The values of A and r for the unmodified Clark model are noninfluential to the symmetry of the breakthrough curve; however, an increase in the value of A indicates a shift of the breakthrough curve towards the right-hand side, while an increase in r indicates a steeper curve as observed (Figure 4.7). The h parameter is better suited to tracking curve symmetry for the fractal-like model: $h = 0$ generates a symmetrical curve and as h deviates towards unity, the curve becomes more asymmetric (Hu et al., 2020).

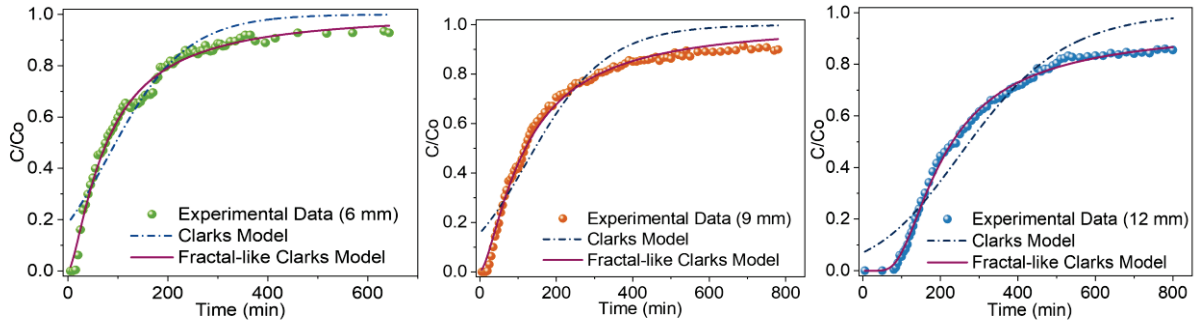

Figure 4.7: Clarks vs fractal-like Clarks model fitted to the adsorption data with varied bed depth

Table 4.4: Parameters and statistical analyses for Clarks and fractal-like Clarks model

	Clarks Model			**Fractal-like Clarks Model**		
Bed Depth (mm)	6	9	12	6	9	12
$R^2_{adj.}$	0.920	0.905	0.929	0.990	0.993	0.997
Reduced $\boldsymbol{\chi^2}$ ($\times$ $\mathbf{10^{-3}}$)	4.89	7.45	6.01	0.063	0.549	0.230
RMSE	0.069	0.085	0.076	0.024	0.023	0.015
BIC	-173	-153	-142	-326	-364	-364
A	1.312	1.524	2.773	5279	4009	0.008
r ($\boldsymbol{min^{-1}}$)	0.012	0.009	0.007	0.689	0.647	24.54
h	0	0	0	0.873	0.866	0.946

4.3.6 Probability distribution function models

The log-normal and log-Gompertz functions had the best correlations ($R^2_{adj} > 0.98, RMSE < 0.005$) to all breakthrough curves regardless of the shape (Figure 4.8 and Table 4.5). In contrast, their unmodified versions performed poorly to even the slightly asymmetrical 6 mm bed-depth curve: also reporting contradictory nonzero effluent concentrations at $t = 0$.

The Weibull function outperformed the normal and Gompertz fits ($R^2_{adj} > 0.97$ and $RMSE < 0.005$), but similarly the fit worsens as tailing becomes more pronounced. The goodness-of-fit based on the lower RMSE and adjusted coefficients of determination values (Table 4.5) were in the order Normal < Gompertz < Weibull < log-normal < log-Gompertz. It is worth noting that we purposely left out the BIC criterion when comparing the probability distribution function models because they all have the same number of fitting parameters.

The reason for this difference in the performance of the probability distribution functions is the type of inflection point for each model. The normal and Gompertz functions have a fixed inflection point while the log-normal, Weibull, and log-Gompertz functions have a floating inflection point capable of adjusting to the shape of the breakthrough curve regardless of symmetry (Chu, 2020b, 2021b; Chu & Hashim, 2022).

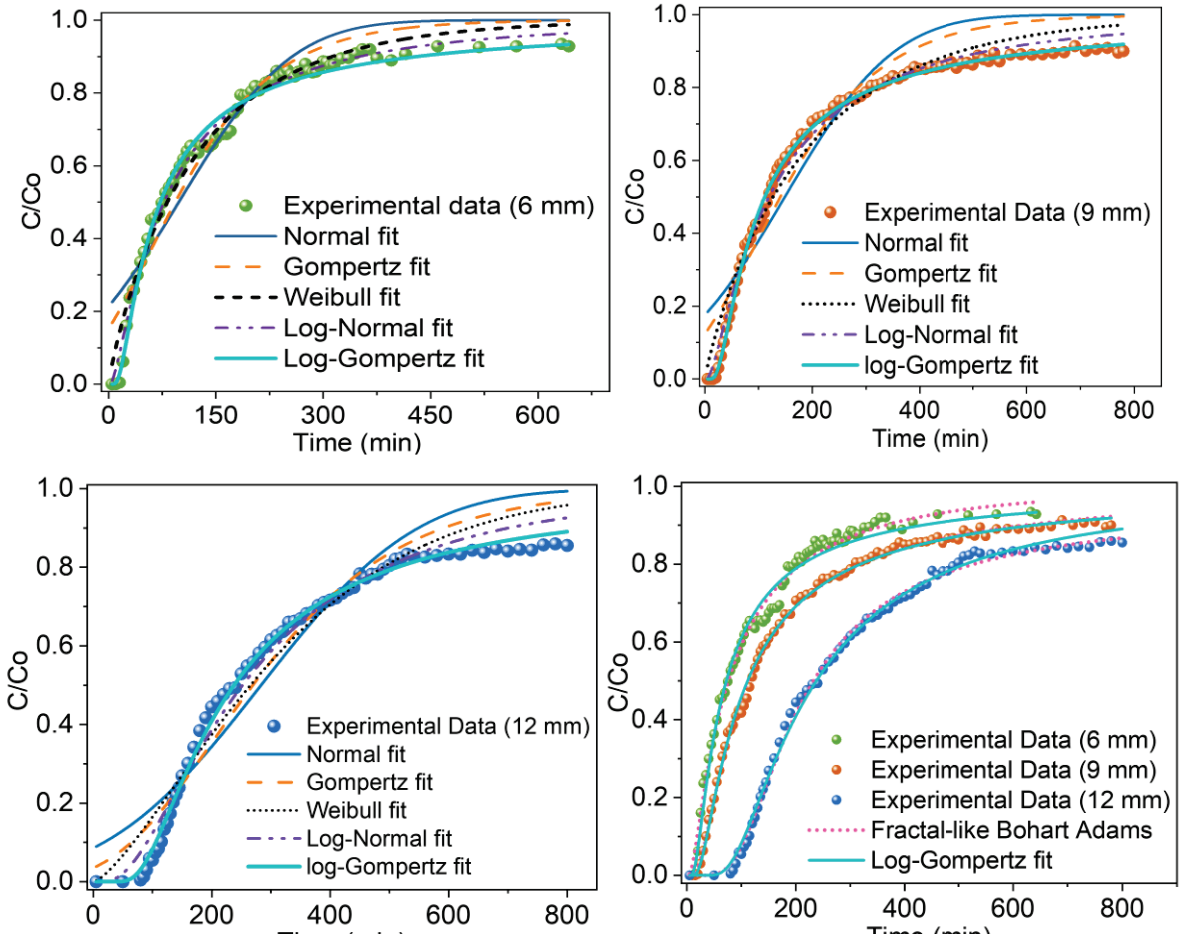

Figure 4.8: Comparison between various probability distribution function models

Mathematically, the position of an inflection point is determined by finding the time at which the second derivative of the respective equations equates to zero (Chu, 2021b). The second derivative (Eq. (4.36)) for the normal equation (Eq. (4.17)) has a solution $t = a_1$ when equated to zero. Substituting this t-term to Eq. (4.17) generates Eq. (4.37) showing an inflection point fixed midway of the generated sigmoidal curve.

$$\frac{\partial^2(C/C_0)}{\partial t^2} = \frac{(a_1 - t)\exp[(a_1 - t)^2/2b_1^2]}{b_1^3\sqrt{2\pi}} \tag{4.36}$$

$$\frac{C}{C_0} = \frac{1}{2} \tag{4.37}$$

In comparison, equating the second derivative equation (Eq. (4.38)) for the log-normal function (Eq. (4.18)) to zero gives the solution $\ln(t) = a_2 - b_2^2$. Substituting this function back to Eq. (4.18) gives Eq. (4.39) indicating a floating inflection point dependent on the value of b_2. The calculated inflection points were at $c/c_0 = 0.12, 0.12,$ and 0.21 for 6 mm, 9mm, and 12 mm plots, respectively. The tendency of these inflection points to move further from the midpoint

towards zero translates to the curve's ability to correlate asymmetrical breakthrough curves (Chu, 2021b). The increase in tailing pushed the inflection point towards the midway signifying the deviation of log-normal fit struggles in handling heavily tailed breakthrough curves. Chu and Hashim noticed a similar difficulty when comparing data from hydrogen sulphide gas removal using carbon filters (Chu & Hashim, 2022).

$$\frac{\partial^2(C/C_0)}{\partial t^2} = \frac{\left(a_2 - b_2^2 - \ln(t)\right)\exp\left[-(a_2 - \ln(t))^2/2b_2^2\right]}{b_1^3 t^2\sqrt{2\pi}} \quad (4.38)$$

$$\frac{C}{C_0} = \frac{1}{2}\left[1 - \mathrm{erf}\left(\frac{b_2}{\sqrt{2}}\right)\right] \quad (4.39)$$

Table 4.5: Probability distribution function parameters and the model's statistical validation

Model	Bed depth (mm)	a	b (min^{-1})	R^2_{adj}	RMSE
Normal	6	98.13	123.66	0.897	0.009
	9	148.77	159.83	0.879	0.011
	12	283.22	207.10	0.906	0.011
Gompertz	6	0.63	0.01	0.936	0.007
	9	0.74	0.01	0.925	0.009
	12	1.21	0.01	0.948	0.008
Weibull	6	123.42	0.90	0.979	0.004
	9	190.06	0.90	0.972	0.005
	12	346.11	1.38	0.956	0.007
Log-normal	6	4.35	1.18	0.991	0.003
	9	4.78	1.16	0.992	0.003
	12	5.53	0.80	0.983	0.005
Log-Gompertz	6	4.15	1.06	0.987	0.003
	9	4.72	1.08	0.998	0.001
	12	7.70	1.47	0.996	0.002

Though the Gompertz function performance was slightly better than the normal function, it was still a poor fit to all the breakthrough curves. Equating the second derivative of the Gompertz function (Eq. (4.40)) to zero gives $t = a_3/b_3$ for the t-term. Substituting this solution to Eq. (4.19) yields Eq. (4.41) denoting a fixed inflection point at $c/c_0 = 0.37$ (Chu, 2020b). This smaller inflection and its shift from the midpoint towards the origin explains the ability of the Gompertz function to fit slightly asymmetrical data and outperform the normal function. Hu et al., using a five-parameter Gompertz function also found the Gompertz function to be superior to the logistic function analogous to the Bohart-Adams model and normal function (Chu, 2020b; Hu et al., 2022).

$$\frac{\partial^2(C/C_0)}{\partial t^2} = b_3^2[\exp(a_3 - b_3 t) - 1]\exp[-\exp(a_3 - b_3 t) + a_3 - b_3] \quad (4.40)$$

$$\frac{C}{C_0} = \exp(-1) \tag{4.41}$$

The second derivative (Eq. (4.42)) of the log-Gompertz function (Eq. (4.20)) yields Eq. (4.43) for the t-term. Plugging this solution into Eq. (4.20) leads to Eq. (4.44) showing that the log-Gompertz's inflection varies with the b term. The inflection points were $c/c_0 = 0.14, 0.15, \text{and } 0.19$ for the 6 mm, 9 mm, and 12 mm bed-depth breakthrough curves. They are closer to the origin than to the midpoint value hence a better fit for the tailed asymmetrical data. Interestingly, log-normal inflection points for 6 mm and 9 mm bed depth are lower than those for log-Gompertz even though log-Gompertz has a much better fit. This is unexpected because the model with smaller inflection points should outperform the other. Overall, the log-Gompertz function performs exceptionally well regardless of the extent of tailing—just like the fractal-like Bohart-Adams model (Figure 4.8d). Juela *et al.* also showed the superiority of the log-Gompertz model to a mechanistic model in fitting asymmetric data from sulfamethoxazole adsorption onto sugarcane bagasse (Juela et al., 2021).

$$\frac{\partial^2(C/C_0)}{\partial t^2} = b_4 t^{-2(b_4+1)} \exp[a_4 - \exp(a_4)\, t^{-b}]\,[\exp(a_4)b_4 - (b_4+1)t^{b_4}] \tag{4.42}$$

$$ln(t) = \frac{a_4 + \ln[b_4/(b_4+1)]}{b_4} \tag{4.43}$$

$$\frac{C}{C_0} = \exp\left[-\left(\frac{b_4+1}{b_4}\right)\right] \tag{4.44}$$

Equating the second derivative (Eq. (4.45)) of the Weibull function (Eq. (4.21)) to zero gives Eq. (4.46) for the t-term. Substituting this to Eq. (4.21) yields Eq. (4.47) showing the dependency of the inflection point to the b-term, hence a floating inflection point (Chu, 2021a). The inflection points were $c/c_0 = -0.12, -0.11, \text{and } 0.24$ for the 6 mm, 9 mm, and 12 mm bed-depth breakthrough curves. The points tend to approach the midway as the fits deviate further from experimental data. The floating inflection points explain the Weibull function's capability of fitting fairly tailing data; a feature observed by Weibull himself (Weibull, 1951). Chu confirms this in fitting chromium adsorption onto olive stone particles and da Silva *et al* while investigating Fe^{2+} adsorption onto algae *L. calcareum* (Chu, 2021a; da Silva Almeida et al., 2021).

$$\frac{\partial^2(C/C_0)}{\partial t^2} = \frac{\exp[-(t/a_5)^{b_5}]b_5(t/a_5)^{b_5}[b_5 - 1 - b_5(t/a_5)^{b_5}]}{t^2} \tag{4.45}$$

$$t = a_5 \left(\frac{b_5 - 1}{b_5}\right)^{\frac{1}{b_5}} \quad (4.46)$$

$$\frac{C}{C_0} = 1 - \exp\left[\left(\frac{b_5 - 1}{b_5}\right)\right] \quad (4.47)$$

Theoretically, the Weibull function with the smallest inflection point values should be the best overall in simulating asymmetrical data when compared with log-normal and log-Gompertz functions. Experimentally, our observation suggests that no correlation can be made about the position of the inflection point with regards to goodness-of-fit when comparing different probability functions; a case similarly observed when comparing the inflection points belonging to log-normal and log-Gompertz functions. Nonetheless, the position of the inflection point is a good indicator of the goodness-of-fit when comparing the fitting capability of the same probability distribution function: the further the position of the inflection points from the midpoint towards the origin, the better the fit.

4.4 Conclusion

This chapter shows that the adsorption of bisphenol-A onto the surface and pores of villi-structured polyaniline was through a diffusion-limited process; consequently, the breakthrough curves were asymmetrically shaped from a tailing phenomenon whose extent increased with an increase in bed depth. High adsorbent surface coverage by the adsorbate could have created steric blocking which decreased the adsorption rate leading to the tailed breakthrough curves. The simple classical Bohart-Adams and Clark models failed to correlate these asymmetrical curves because they are based on assumptions of simple kinetics: a single time-independent rate factor lumping all mass transport mechanisms.

The modified simple models: log-Bohart-Adams, fractal-like-Bohart-Adams, and fractal-like-Clarks models, were better suited to simulate asymmetrical breakthrough curves. These models estimated more accurately saturation and breakthrough times, size of the mass transfer zone, critical bed depth of 5.65 mm, sorption capacity, rate coefficients, and time required for 50% breakthrough. The log-modified Bohart-Adams—shown to be equivalent to the modified dose-response model—was capable of handling tailing but only to some extent.

The fractal-like Bohart-Adams overcame the shortcoming of the log-Bohart-Adams model enabling the simulation of all breakthrough curves regardless of symmetry. Fractal-like Clark's model behaved similarly. The success of these fractal-like models was because they introduce a fractal-like component h which regards the mass coefficient as a time-independent factor. The value of h was an indicator of symmetry: $h = 0$ represented a symmetrical curve, while the deviation of h towards unity indicated a shift towards greater asymmetry.

The probability distribution functions with floating inflection points: log-Gompertz, log-normal, and Weibull functions were better suited to correlating asymmetrical breakthrough curves; however, the Weibull function was unable to fit the tailing data. The deviation of these floating inflection points from the midpoint, $C/C_0 = 0.5$, towards the origin signified the ability of the function to fit the breakthrough curve. However, there is a lack of evidence to show that the position of these inflection points could be used to compare goodness-of-fit between two distinct functions. The optimal fitting capabilities were log-Gompertz > log-normal >Weibull > Gompertz > Normal function. Though these probability distribution function models remain unused in process design for they lack fixed-bed variables, they can be used to accurately estimate breakthrough and saturation time.

We also highlighted modelling misconceptions and mistakes that are still being observed in the field of fixed-bed modelling: fitting the mathematical equivalent of simple Bohart-Adams, Thomas, and Yoon-Nelson models to the same data and comparing their fitting capabilities; use of an erroneous "Adam-Bohart model", which represents an exponential function rather than a logistic function; regarding bed-depth-service-time (BDST) equation as an independent model and using it for modelling work. We voice our concern together with other researchers who have observed a similar growing trend and recommend more stringent peer-review processes to address them. These mistakes only end up confusing unsuspecting researchers new to this field leading to inaccurate results or misinterpretations of data.

Chapter 5: A Trojan Horse Approach for the Synthesis of Scalable Cu-BDC Patterned Polyaniline/Cu-Carboxymethyl Cellulose Microbeads for the Degradation of Diclofenac and Sulfamethoxazole

5.1 Introduction

Hybrid porous materials known as metal-organic frameworks (MOFs) have been developed through the assembly of metal ions and organic linkers. These materials have shown great promise for a variety of applications in multiple fields, including adsorption (Ihsanullah, 2022), catalysis (Qian et al., 2021), gas storage (Y. Li et al., 2022), and drug delivery (Lawson et al., 2021). Among the vast array of MOFs, copper-containing MOF, Cu-BDC—where BDC^{2-} is 1,4-benzenedicarboxylate—is a promising material due to its exceptional stability, high surface area, and tuneable pore size (Shete et al., 2018).

Figure 5.1 illustrates the building block structure of the Cu-BDC framework, which includes two copper cations in a five-coordinate arrangement bridged together in a paddle-wheel configuration. These copper cations are coordinated to terephthalate ligands (BDC^{2-}) in a bridging bidentate manner (Zhan et al., 2019).

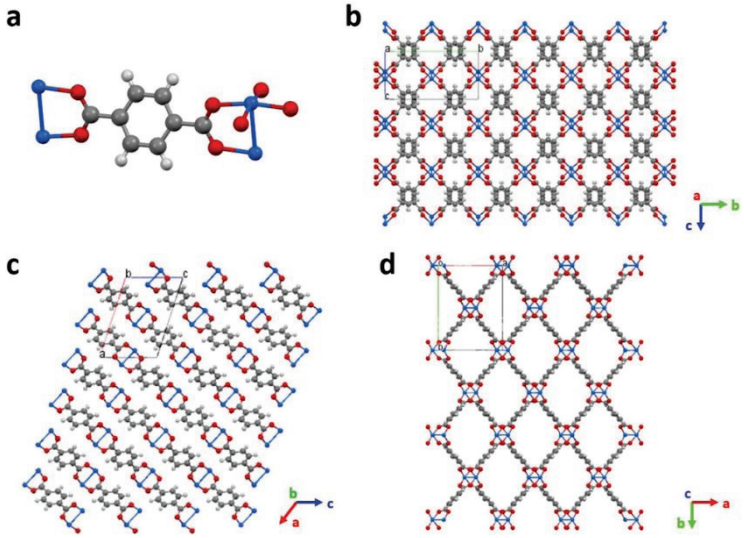

Figure 5.1: Showing paddle-wheel building block for Cu-BDC frameworks in different views. Copper, oxygen, carbon, and hydrogen atoms are shown in blue, red, grey, and white, respectively

However, conventional methods for synthesising Cu-BDC often require harsh reaction conditions, such as high temperatures and toxic solvents, which can limit their scalability and practical applications. To address these challenges, we propose a novel trojan-horse approach for synthesising Cu-BDC using an aqueous environment. In this approach, we utilised carboxymethyl cellulose (CMC), a biocompatible and environmentally friendly polymer, to

suspend the BDC linker, which was then dropped into a copper solution. This unique approach allows for the controlled release of BDC onto the interface between the copper solution and carboxymethyl cellulose surface, facilitating the formation of Cu-BDC crystals.

The utilisation of an aqueous environment and CMC as a carrier for BDC offers several advantages over traditional methods. Firstly, it eliminates the need for toxic organic solvents, reducing the environmental impact of the synthesis process. Moreover, it provides a controlled and gradual release of BDC, which can improve the homogeneity and reproducibility of Cu-BDC crystals. Additionally, the aqueous environment can promote the formation of high-quality Cu-BDC crystals with enhanced purity and crystallinity, as water can act as a template and modulator during the crystal growth process.

5.2 Methodology

5.2.1 Materials

Carboxymethyl cellulose (CMC, CAS 039-01335), N, N-Dimethylformamide (DMF, ≥99.5%), anhydrous copper (II) acetate (≥97%), and ethanol (≥99.5%)were purchased from Wako Chemicals. Aniline (≥99%)—distilled before use—and copper (II) nitrate trihydrate (≥99%) were purchased from Nacalai tesque. 1,4-benzenedicarboxylate (Terephthalic acid, $H_2BDC \geq$ 99%) was purchased from Tokyo Chemical Industry. Chloramphenicol (≥99%) was purchased from Sigma-Aldrich.

5.2.2 Synthesis of Cu-BDC/PANI/Cu-CMC microbeads

The microbeads were synthesised by first suspending 4 mmol of H_2BDC in a 2% w/v CMC solution prepared in deionised water. The resulting mixture was vigorously stirred for an hour to form a viscous milky suspension. Previously distilled aniline (4 mmol) was added to this solution and stirred for an additional hour. The mixture was placed in a syringe and added dropwise from a 1mm internal diameter nozzle to a 0.2M copper solution of either $Cu(CH_3COO)_2$ or $Cu(NO_3).3H_2O$ at a rate of 2 mL/min. The resulting beads were left in the respective solutions for 8 hrs to equilibrate at room temperature (25℃) and ensure a complete reaction. The beads were washed with deionised water, soaked in ethanol for 30 minutes, and then soaked in deionised water before being freeze-dried using an Eyela freeze drier (FD-1000, Japan). Microbeads prepared in the acetate solution were designated with an (a), while (n) was used for those prepared in the nitrate solution.

Control microbeads were also synthesised similarly: Cu-CMC was synthesised by only adding the 2% w/v CMC solution to the copper solutions; PANI/Cu-CMC microbeads were

synthesised by only adding 4 mmol of aniline to the 2% w/v CMC solution; Cu-BDC/Cu-CMC were synthesised by adding only 4 mmol of H_2BDC to the 2% w/v CMC solution. Cu-BDC nanoparticles were also prepared as per the literature (K. Huang et al., 2015) to confirm the effectiveness of our reagents and X-ray diffraction peaks.

5.2.3 Characterisation

The surfaces and cross-sections of the microbeads were examined by scanning electron microscopy (SEM). Samples mounted on carbon tape were coated with platinum using a magnetron sputter (MSP-1S, Japan) to avoid surface charging during analysis. The micrographs were obtained on a Hitachi scanning electron microscope (SU3500, Japan).

Functional groups were recorded using a Jasco Fourier Transmission Infrared spectrophotometer (FT/IR 4700, Japan) equipped with an Attenuated Total Reflectance (ATR) cell; the obtained spectra were from an average of 60 scans set at 2 cm^{-1} resolution in the range $4000 - 500\ cm^{-1}$ The cell was cleaned and dried between samples using isopropyl alcohol.

Wide-angled X-ray powder diffraction patterns of the polymers were obtained on an X-ray diffractometer (Rigaku ULTIMA IV, Japan) using Cu Kα radiation (λ = 1.5418Å). The data was collected between 5° and 70° angular range.

5.3 Results and Discussion

5.3.1 Characterisation of adsorbents

The microbeads were spherically shaped but differed in both colour and size (Figure 5.3 and Figure 5.2). The sky-blue coloured microbeads, typical of copper crosslinked carboxymethyl cellulose (Gholamali, 2020), change to a greenish colour with the introduction of polyaniline moiety, which is typical of the emeraldine form of polyaniline or polyaniline in acidic presence (Mota et al., 2019; Tanwar & Ho, 2015). It is worth noting that the pH of 0.2M copper (II) nitrate hexahydrate and copper acetate anhydrous solutions were determined to be 3.93 and 5.32 respectively. The Cu-BDC/CMC-Cu and Cu-BDC/PANI/CMC-Cu microbeads have duller blue and green colours due to an additional mix of deep-blue coloured Cu-BDC on the surface (Nejatbakhsh et al., 2022).

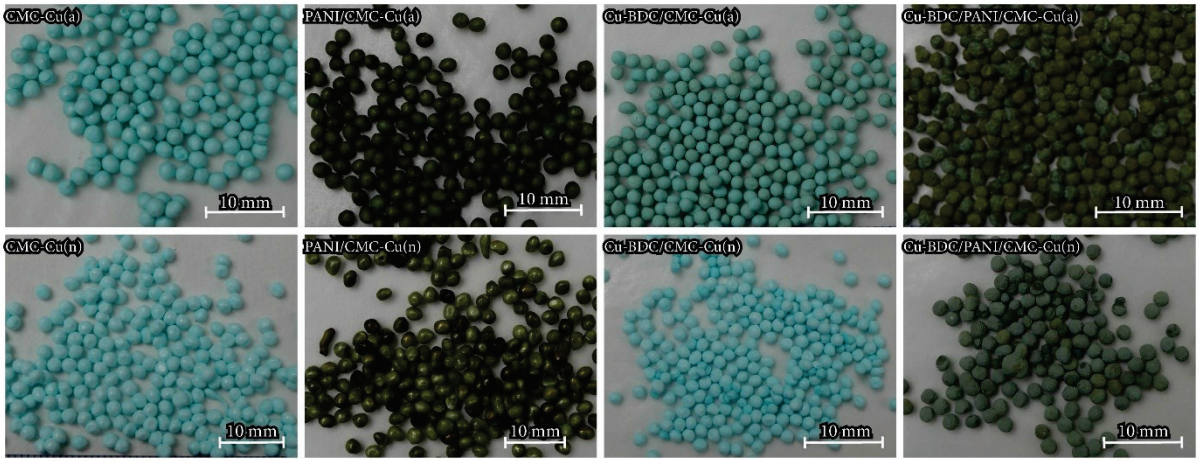

Figure 5.3: Photographs showing the acetate (a) and nitrate (n) copper sources prepared microbeads

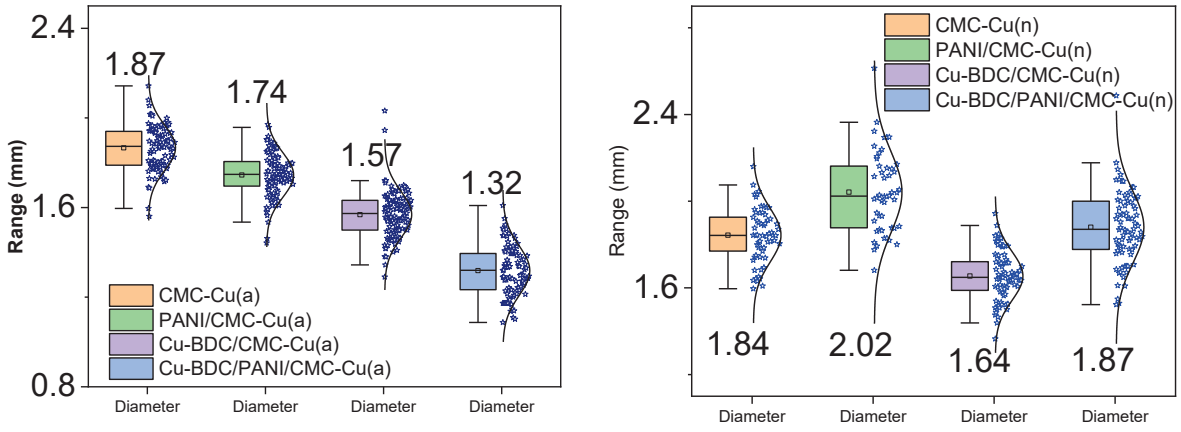

Figure 5.2: Boxplots with associated normal distribution plots showing the size distribution of the microbeads prepared from acetate (a) and nitrate (n) copper-ion sources.

The acetate-source prepared microbeads were smaller on average and more uniformly sized compared with the nitrate-source prepared microbeads (Figure 5.2); however, the average

diameters of all microbeads were significantly different as shown by the analysis of variance and Tukey's Honestly Significant Difference (HSD) for multiple comparisons performed at a 0.05 significant level (Appendix IV and Appendix V, ANOVA, *P=0.000*). This means that the additional components in the preparation of the microbeads and the copper ion source significantly affect the microbead sizes.

The FTIR spectra (Figure 5.4 and Figure 5.5) show that all microbeads have functional groups similar to the CMC backbone: broad bands from 3600 cm^{-1} to 1750 cm^{-1} from carboxylic $-OH$ stretching vibrations; bands at 2978 cm^{-1} and 2895 cm^{-1} from sp^3 $-CH$ symmetrical and asymmetrical stretching vibrations; strong sharp peaks at 1589 cm^{-1} and 1416 cm^{-1} from COO^- asymmetrical and symmetrical stretching vibration, however, these particular peaks shift to shorter wavelengths (hypsochromic shift) for the Cu-BDC complex indicating interaction in this functional group.

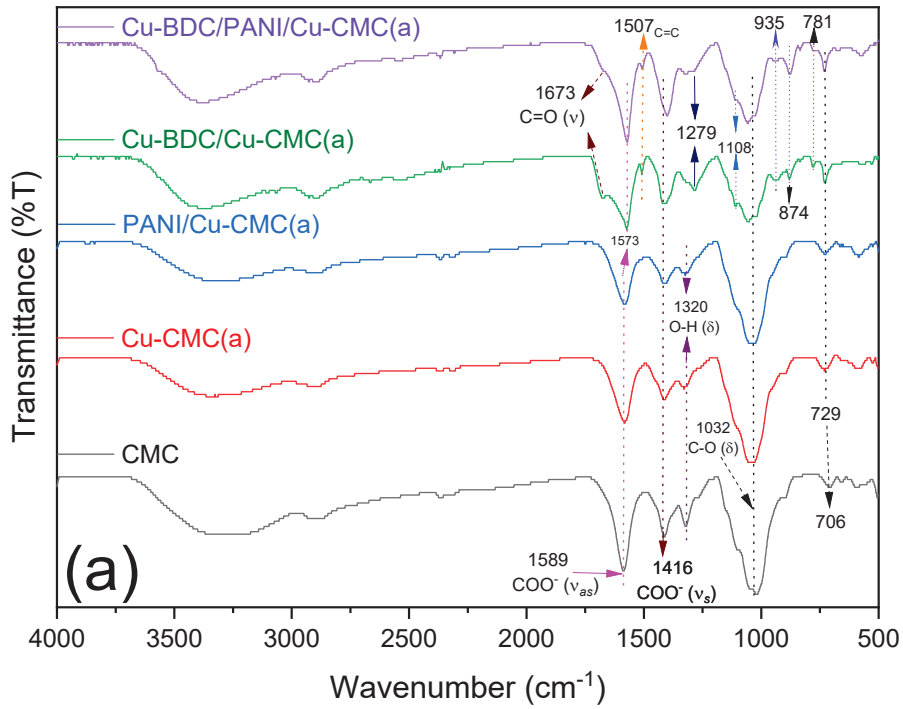

Figure 5.4: FTIR spectra for CMC and acetate prepared Cu-CMC(a), PANI/Cu-CMC(a), Cu-BDC/Cu-CMC(a), and Cu-BDC/PANI/Cu-BDC(a) microbeads

The band at 1032 cm^{-1} representative of an alkoxy $C-O$ bending vibration was also present in all prepared beads. There were bands only specific to the Cu-BDC beads: 1673 cm^{-1} and 1507 cm^{-1} attributed to stretching vibration of the carbonyl group present on H_2BDC and aromatic $C=C$ stretching vibration; 1279 cm^{-1} and 1108 cm^{-1} for acyl $C-O$ stretch present on H_2BDC and Cu-O-Cu stretching vibration (Sani et al., 2015); 953 cm^{-1}, 874 cm^{-1}, and 777 cm^{-1} all representing aromatic $C-H$ bending vibrations. The $-OH$ bending vibration peak at 1320 cm^{-}

[1] disappears—or reduces in intensity to be detected—on the Cu-BDC beads confirming the replacement of most of the −OH hydrogen by copper. There were unnoticeable differences between the spectra of microbeads prepared in acetate and nitrate showing irrelevance of counter anions of the copper salt towards the functional groups present.

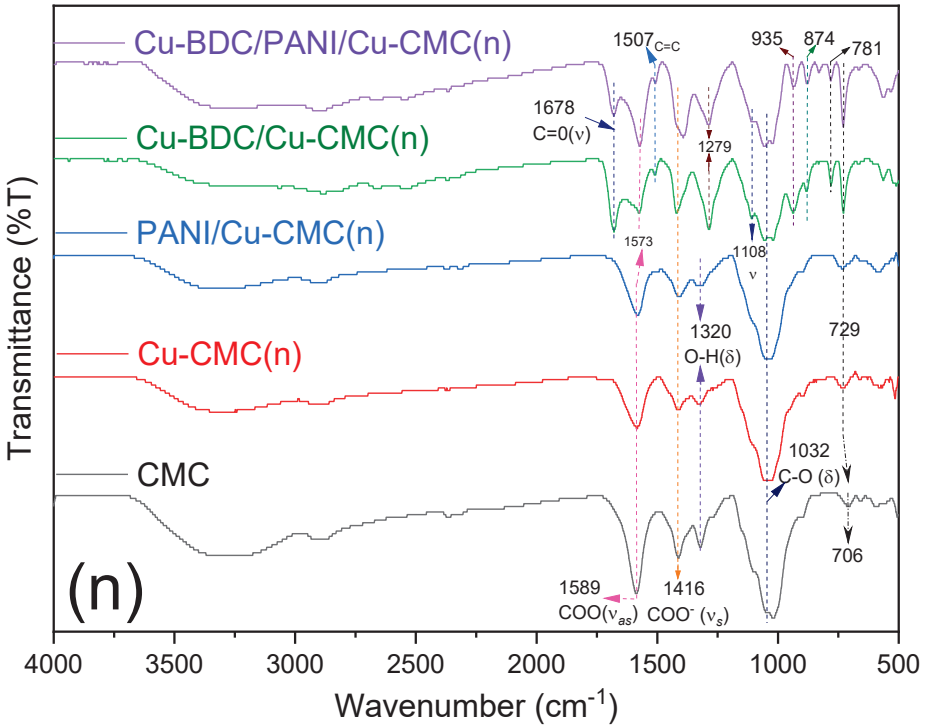

Figure 5.5: FTIR spectra for CMC and nitrate prepared Cu-CMC(n), PANI/Cu-CMC(n), Cu-BDC/Cu-CMC(n), and Cu-BDC/PANI/Cu-BDC(n) microbeads

It is worth noting that CMC and Cu-CMC FTIR spectra differed only in the bathochromic shift of the peak at 706 cm^{-1} to 729 cm^{-1} representing the loss of Na^{+} ions. The peaks related to PANI were masked by the strong CMC bands which were in a higher concentration than PANI.

The surface of the acetate-prepared microbeads (Figure 5.7) varied depending on the substance added during the reaction. Only the surface of the Cu-BDC/PANI/Cu-CMC(a) had sheet-like folds whose surface was patterned with 483.78±7.29 nanometre-sized Cu-BDC crystals (Figure 5.6 and Appendix VI). In contrast, these folds and crystals were not present on the surface of the Cu-BDC/Cu-CMC(a), neither were they present on the surface of PANI/Cu-CMC(a) microbeads suggesting that the interaction between the amine and H_2BDC molecules favoured the formation of the crystals. The Cu-BDC crystals on the PANI/Cu-CMC(a) microbead surface appear as well-defined, faceted structures with sharp edges indicative of their crystalline nature. The crystals are uniformly dispersed on the surface of the PANI/Cu-CMC(a) microbeads, forming a dense and regular array of crystals.

The cross-sections (Figure 5.9) of the acetate-ion source microbeads consisted of a dense network of interwoven fibres typical of metal-ion crosslinked CMC hydrogels (Maslamani et al., 2021). The resulting surface consists of a narrow porous monolithic structure. There were no observable Cu-BDC crystals on the internal structures of the Cu-BDC/PANI/Cu-CMC(a). Similarly, the cross sections of the H_2BDC encapsulated microbeads look similar to the ones that contained BDC, which indicates that the encapsulated H_2BDC molecules were not trapped

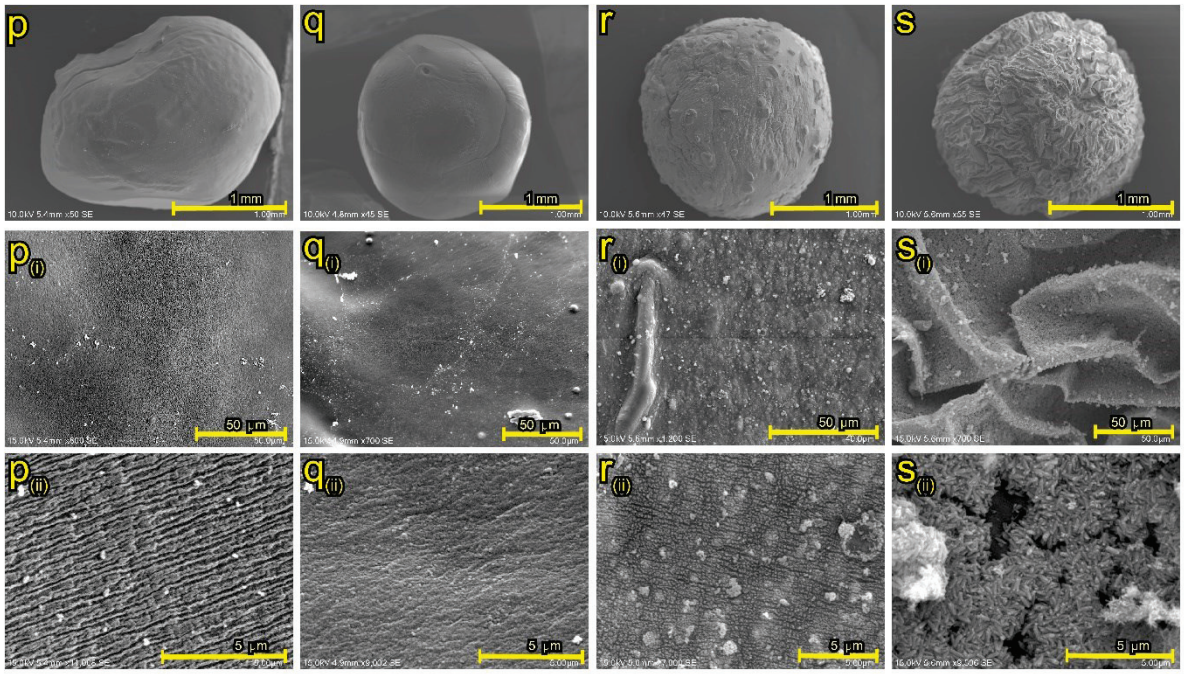

Figure 5.7: Surface SEM micrographs for acetate prepared Cu-CMC (p), PANI/CMC (q), Cu-BDC/CMC (r), and Cu-BDC/PANI/CMC (s) at various magnifications

in the resulting polymer matrix, but rather moved towards the surface reacting with surface available Cu^{2+} ions.

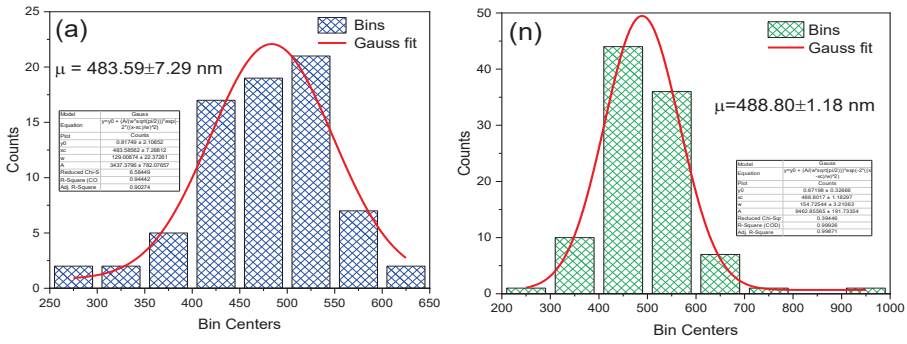

Figure 5.6: Size distribution of acetate prepared (a) and nitrate (n) prepared Cu-BDC on the surface of PANI/Cu-CMC microbeads

In contrast, the surface of the nitrate-ion source-prepared microbeads differed from the acetate-prepared ones: the folds on Cu-BDC/PANI/Cu-CMC(n) were smaller, brain-matter-like, and

their surface have 488.80±1.18 nm sized spherical protrusions (Appendix VI) of what we believe to be Cu-BDC structures rather than the rice-like crystals. It is evident that the amine functionality from polyaniline is crucial in the formation of these folds and Cu-BDC nanoparticles in a gyrification-like process.

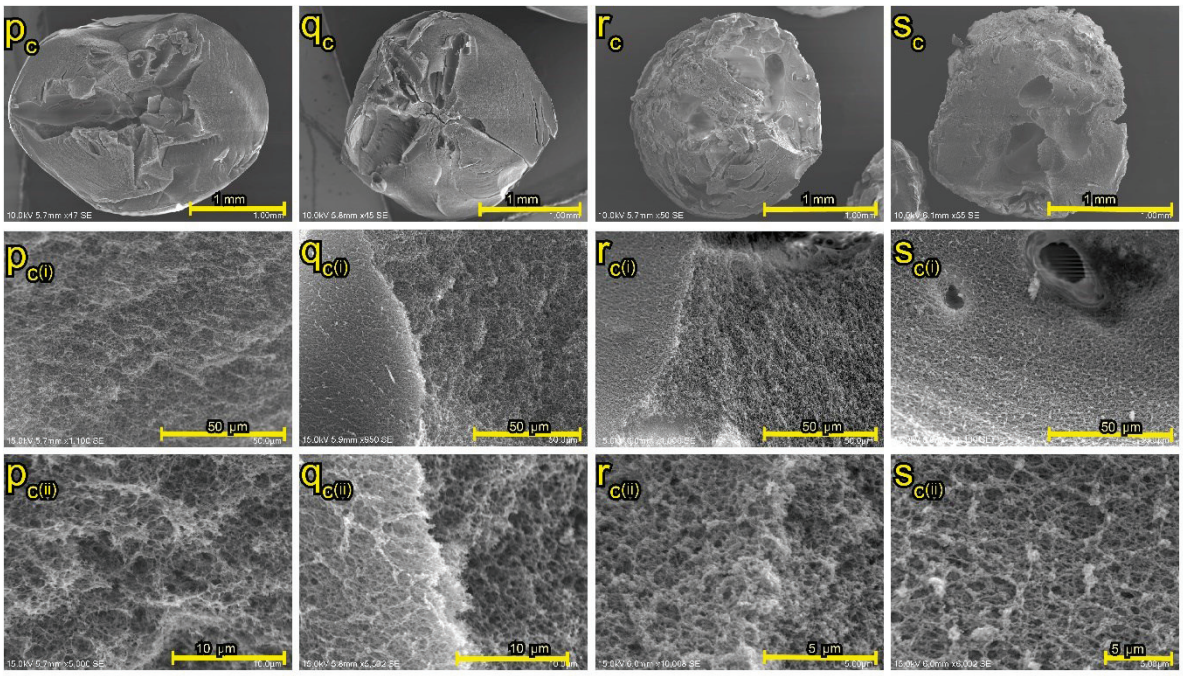

Figure 5.9: Cross-section SEM micrographs for acetate prepared Cu-CMC (p_c), PANI/CMC (q_c), Cu-BDC/CMC (r_c), and Cu-BDC/PANI/CMC (s_c) at various magnifications

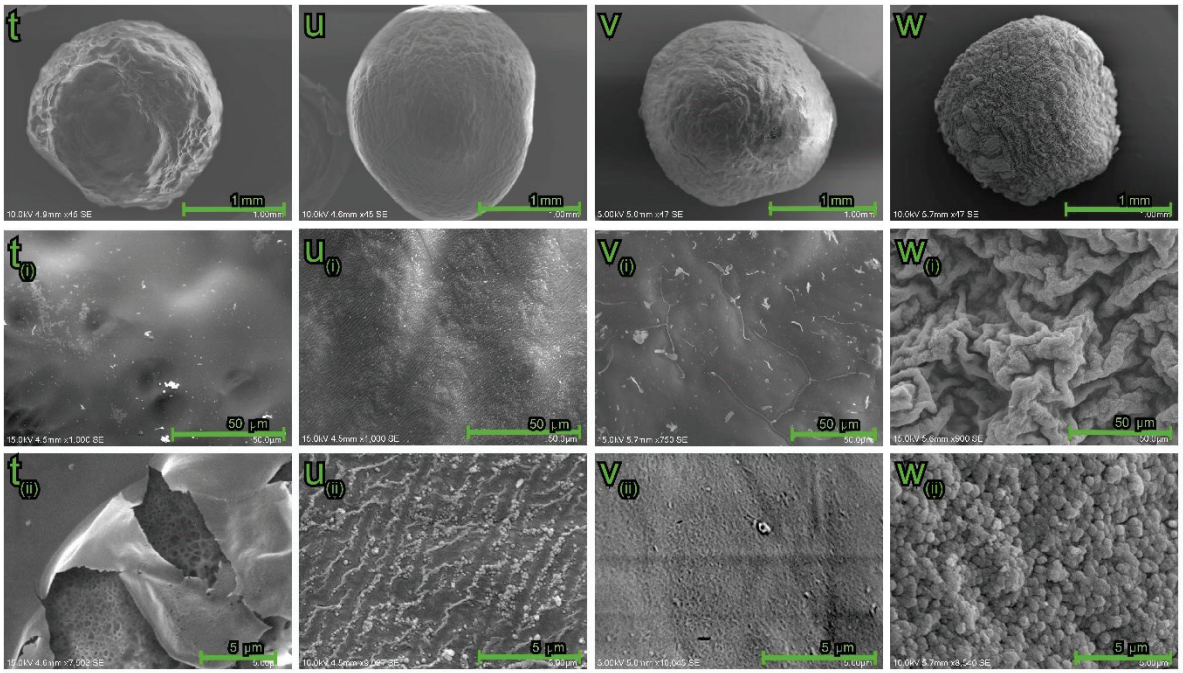

Figure 5.8: Surface SEM micrographs of nitrate prepared Cu-CMC (t_c), PANI/CMC (u_c), Cu-BDC/CMC (v_c), and Cu-BDC/PANI/CMC (w_c) at various magnifications

The cross-sections (Figure 5.10) from the nitrate-ion prepared differed from the acetate ones: there are larger closed-cell foam structures constructed from a densely interconnected network of Cu^{2+} crosslinked CMC. Low-conductivity gases trapped inside a structure lead to the formation of closed-cell foams (Gibson, 2003), implying that nitrate ions generated a nitrogen oxide gas during the reaction. Only the cross-section of the PANI/Cu-CMC(n) lacked the closed-cell foam structures, but instead consisted of layer-by-layer arranged sheets. There are oval-shaped urchin-like spherical particles towards the outer ends of the internal structures Cu-BDC/PANI/Cu-CMC beads (Figure 5.10 $W_{c(i)}$ and Appendix VII) likely to be the Cu-BDC surface protrusions. This confirms our hypothesis of the H_2BDC molecules moving towards the surface of the beads to replenish reacted molecules during the reaction.

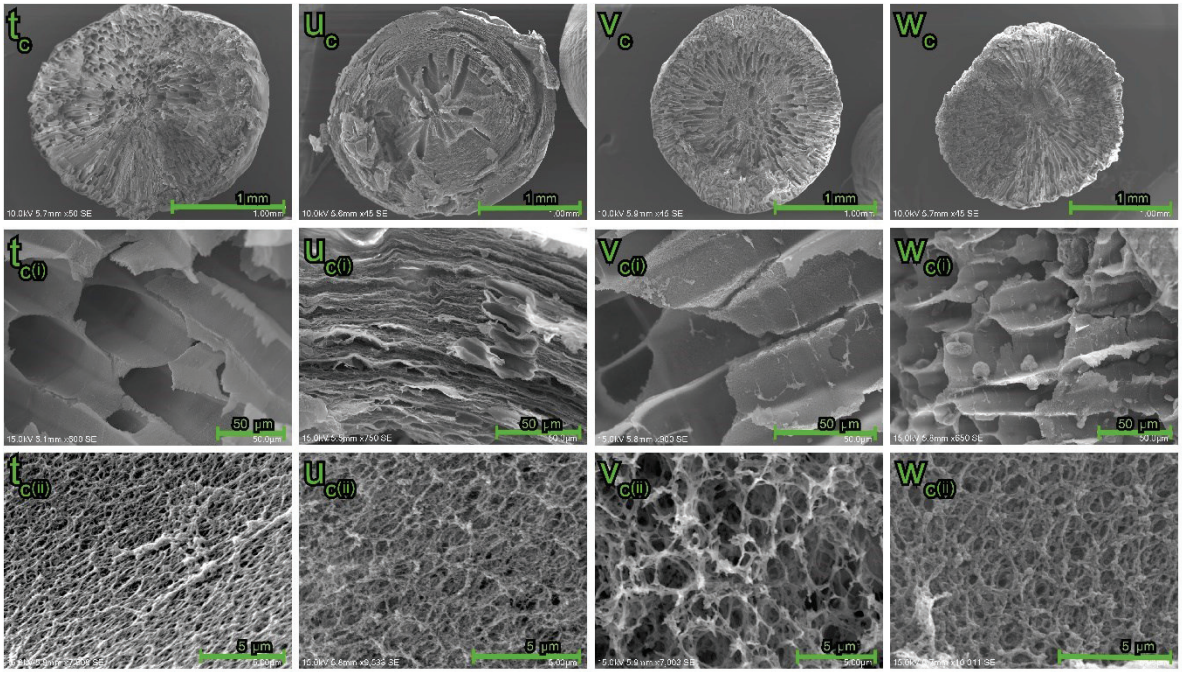

Figure 5.10: Cross-section SEM micrographs of nitrate prepared Cu-CMC (t), PANI/CMC (u), Cu-BDC/CMC (v), and Cu-BDC/PANI/CMC (w) at various magnifications

The Cu^{2+} ion source also influenced the XRD diffraction patterns of the microbeads (Figure 5.11). First, the low intensity at 6.2° was only present for the acetate anhydrous prepared Cu-CMC(a) beads while the peak at 20.2° characteristic of amorphous carboxymethyl cellulose polymeric structure was consistent for both ion sources (Maslamani et al., 2021; Zare-Akbari et al., 2016).

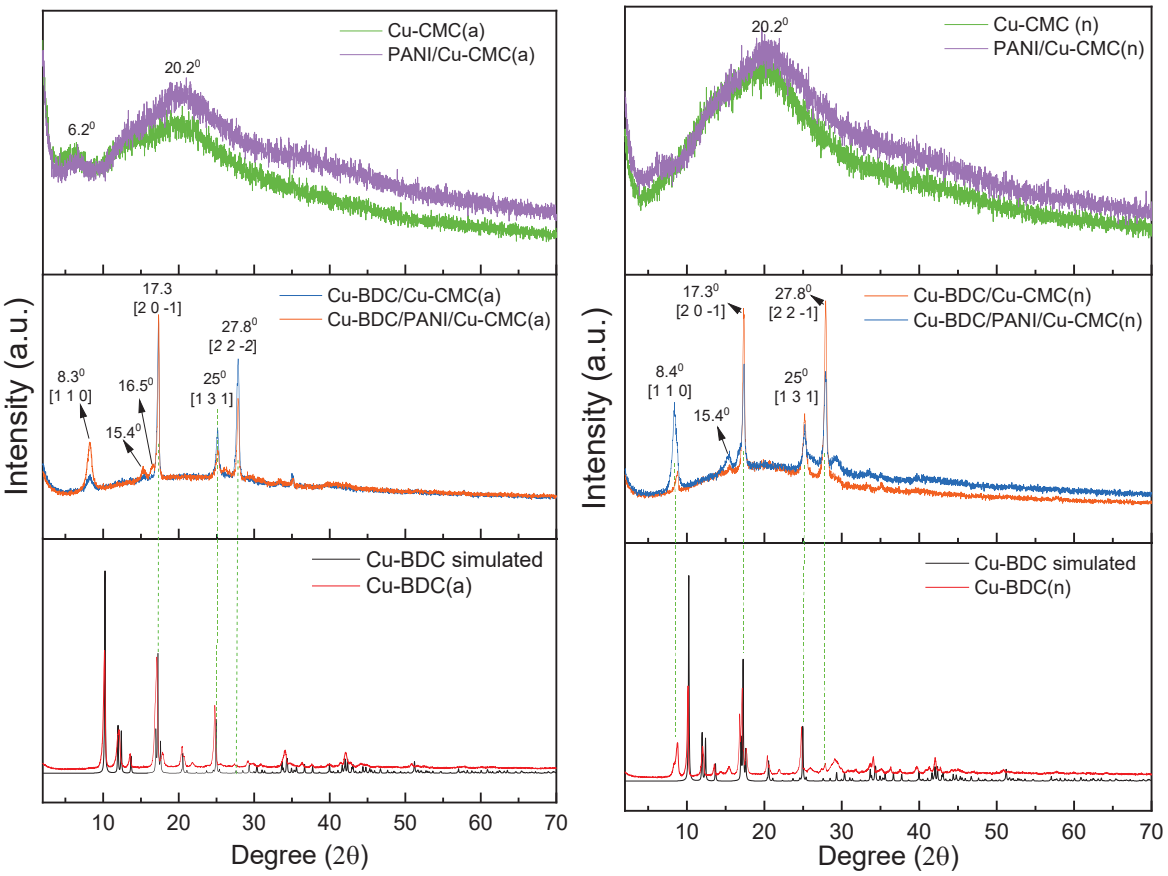

Figure 5.11: XRD diffraction peaks for acetate (a), and nitrate (n) prepared Cu-BDC/PANI/CMC adsorbents cross compared to simulated and prepared Cu-BDC, Cu-CMC, and PANI/CMC.

DMF-prepared Cu-BDC MOF matched with the experimental pattern of the simulated Cu-BDC (CCDC No. 687690) where all Bragg diffractions were detected hence showing that our reagents were well capable of producing the MOFs. In contrast, the nitrate and acetate anhydrous prepared Cu-BDC/CMC and Cu/BDC/PANI/CMC beads exhibited only the [2 0 -1], [1 3 1], and [2 2 -2] crystallographic planes that were aligned with the simulated diffraction pattern of Cu-BDC. This finding confirms the existence of a Cu-BDC layer on the surface of the microbeads with planes perpendicular to the stacking direction (Zhan et al., 2019). The choice of ion source did not have a major effect on the Cu-BDC/PANI/Cu-CMC diffraction peaks other than the low-intensity peak at 16.5° which can be associated with the presence of the crystalline rice-like nanoparticles for the acetate-prepared microbeads.

Lack of the presence of coordinated solvent molecules (DMF) led to bulk and distorted Cu-BDC molecules on the surface of the bead as indicated by the plane [1 1 0] shift to lower angles (Wu & Wang, 2019). This peak shift is characteristic of solvent-free preparation of Cu-BDC (Cheng et al., 2017), interference from the presence of other molecules in the structure,—CMC

and PANI in this case—and water molecules interacting with the Cu-BDC crystal structures (Song et al., 2019).

5.3.2 Degradation experiments

The photocatalytic degradation experiments show a change in the diclofenac and sulfamethoxazole UV/Vis spectra (Figure 5.12), which means that the microbeads were capable of degrading the two pharmaceutical solutions using direct sunlight—a renewable energy source. The longer the exposure time, the more the degraded products were generated. The acetate microbead was better suited owing to the larger spectra meaning a larger number of small molecules from the degradation. We expected this since the characterisation studies showed that these acetate beads had better evidence of the presence of Cu-BDC such as the Cu-BDC rice-like crystals.

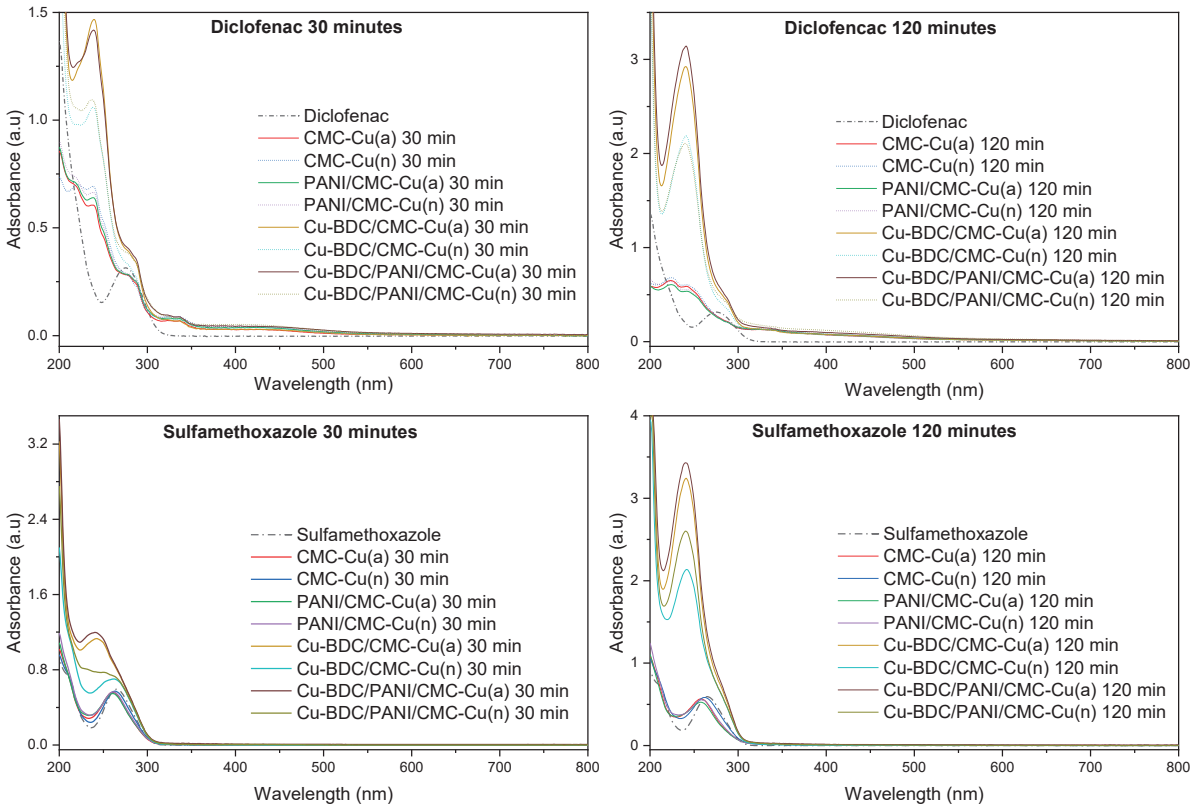

Figure 5.12: Photocatalytic degradation UV/Vis spectra for diclofenac and sulfamethoxazole solutions using the acetate (a) and nitrate (a) prepared microbeads

It is worth noting that our UV/Vis method was just for testing purposes and more work and better instruments need to be used for such degradation studies so that the degradation mechanism and degradation products can be studied in depth using LC-MS. However, the degradation of diclofenac and sulfamethoxazole have been studied and are shown in Figure

5.13 and Figure 5.14. These small molecules were responsible for the increase in UV adsorption in the regions between 200nm and 270nm.

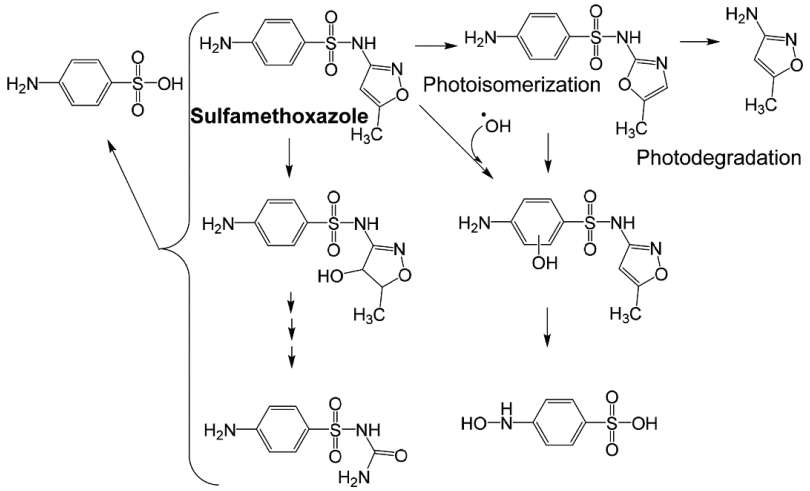

Figure 5.14: Photodegradation pathways of sulfamethoxazole showing degradation products (Trovó et al., 2009)

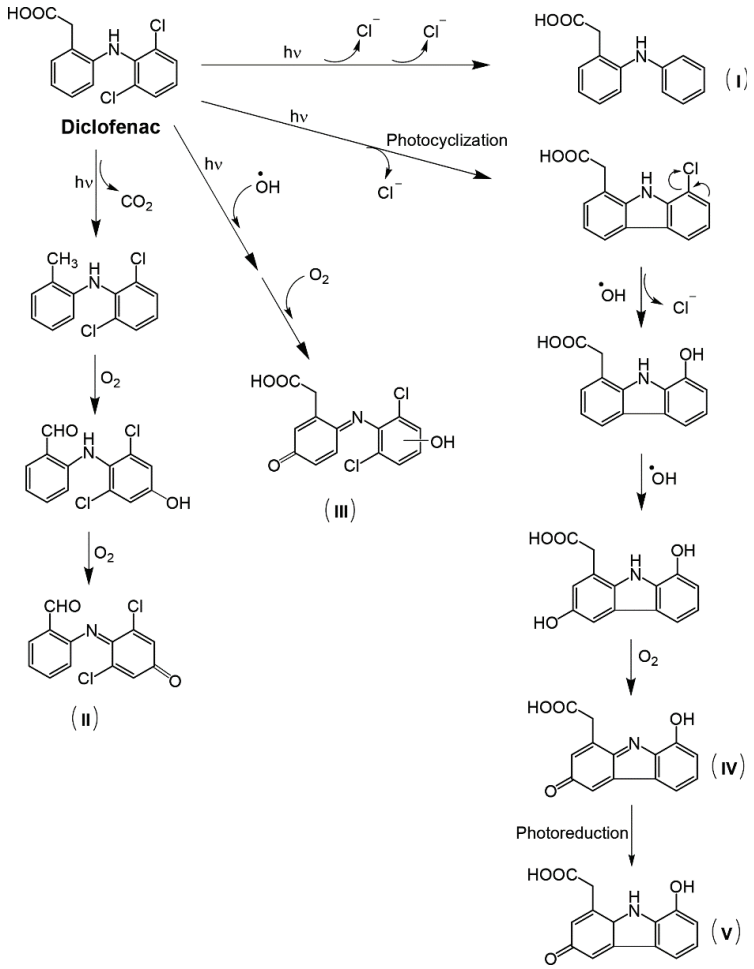

Figure 5.13: Photodegradation pathways of diclofenac showing degradation products (Salgado et al., 2013).

5.4 Conclusion

In this chapter, we have successfully demonstrated an innovative, scalable and environmentally friendly approach for synthesising Cu-BDC MOF microbeads. The beauty of this method is the ability to be conducted at room temperature using only water and ethanol as green solvents. During the synthesis process, we introduced simultaneous aniline oxidation, resulting in the formation of unique folds on the microbeads. These folds significantly increased the surface area of the microbeads, consequently enhancing their adsorption capacity.

The Cu-BDC microbeads produced through our method possess several advantageous characteristics. They are easy to handle and can be efficiently separated from the solution, making them a practical choice for industrial applications. Notably, our synthesis method eliminates the need for toxic solvents commonly used in traditional MOF synthesis. This not only reduces the environmental impact of the production process but also minimises potential health risks associated with the use of such solvents.

Furthermore, our research demonstrates the remarkable catalytic activity of these Cu-BDC microbeads. Specifically, they have been proven to effectively degrade diclofenac and sulfamethoxazole in less than 3 hours when exposed to direct sunlight. While further investigation is required to fully characterise and optimise the degradation products, our work highlights the potential for scalable synthesis of MOF-based macrostructures.

In summary, our findings offer a promising avenue for the development of sustainable and scalable methods for MOF synthesis. This method has wide-ranging applications, including the removal of emerging pollutants from water sources. Overall, our research contributes to the growing field of environmentally conscious materials synthesis and their potential to address pressing global challenges related to pollution and sustainability.

.

Chapter 6: Conclusion and Future Perspectives

Access to clean water is a global challenge, compounded by water pollution and emerging pollutants that lack regulations and are difficult to remove using conventional treatment methods. Finding sustainable solutions to balance the need for effective water pollution solutions and minimising environmental harm and resource inefficiencies is a complex problem that requires innovative approaches.

This study investigated the potential of design of experiment in reducing the number of experiments, which saves on cost, time and resources. We found it possible to include more categorical variables in a single design by utilising custom screening designs; also, we show that definitive screening designs can drastically reduce the number of experiments when dealing with more than five factors. Through this approach, we studied the adsorption potential of villi-structured polyaniline (VSPANI) and its composite with carboxymethyl cellulose (CMC/PANI) and dialdehyde carboxymethyl cellulose (DCMC)—at 35% aldehyde content (DCMC(A)/PANI) and 75% aldehyde content DCMC(B)/PANI)— as adsorbents for removing bisphenol-A (BPA) from water. Our study found that increasing the aldehyde content of the composites favoured adsorption, and VSPANI and DCMC(B)/PANI exhibited potential as adsorbents for BPA removal.

Furthermore, with a desire to evaluate the adsorption process taking place between VSPANI and bisphenol-A, we conducted a fixed-bed column study. Since the breakthrough curves were asymmetrical, we approached breakthrough curve modelling from a different angle. Our study analysed and compared the trend of how well log-modified, fractal-like modified, and probability distribution function models simulate asymmetric breakthrough curves with varied extents of tailing. We found that the log-Bohart-Adams and especially the fractal-like Clark and Bohart-Adams models perfectly fit the curves regardless of symmetry. The study also suggested that polyaniline-based materials needed further research to improve the mass transfer between adsorbent and adsorbate and improve the diffusion-limited process that led to excessive tailing.

We attempted to improve the performance of polyaniline by modifying it with a metal-organic framework: Cu-BDC. To keep the synthetic method sustainable and environmentally friendly, we approached the process through a trojan-horse approach. A CMC and aniline solution encapsulated our H_2BDC molecules allowing CU-BDC crystals to form on the surface of microbeads that show great potential for use in removing emerging pollutants.

Overall, this research provides insights into the development of sustainable and effective adsorbents and processes—optimisation, syntheses, and data analysis— for water treatment and highlights the importance of balancing the need for effective water pollution solutions with the imperative to minimise environmental harm and resource inefficiencies. Future research should focus on further investigating the performance of VSPANI and DCMC(B)/PANI in real-world scenarios and exploring other sustainable adsorption technologies to address emerging pollutants in water.

We recommend the following:

1. Real-World Testing and Application: Further research should involve field-scale or pilot-scale testing of the adsorption potential of VSPANI and DCMC(B)/PANI in real-world scenarios. Understanding their performance under practical conditions is crucial for assessing their viability as water treatment solutions.
2. Long-Term Efficiency and Regeneration Studies: Investigate the long-term efficiency and regeneration capacity of the developed adsorbents. Assess how well they can maintain their adsorption capacity over extended periods and whether they can be regenerated for multiple cycles, which is essential for sustainable water treatment systems.
3. Cost-Effectiveness Analysis: Conduct a comprehensive cost-effectiveness analysis to determine the economic feasibility of using the developed adsorbents and processes at a larger scale. Consider factors such as production costs, material availability, and operational expenses.
4. Environmental Impact Assessment: Assess the environmental impact of the adsorption and photocatalytic processes and materials developed in this study. Ensure that the sustainability goals are met by considering the life cycle analysis, energy consumption, and waste generation associated with these technologies.
5. Optimisation of Synthesis Methods: Continue research into optimising the synthesis methods for the adsorbents, such as VSPANI, DCMC(B)/PANI and Cu-BDC microbeads. Explore variations in synthesis parameters to enhance their performance, stability, and scalability.
6. Exploration of Other Sustainable Adsorption Technologies: Expand the scope of research to explore and develop other sustainable adsorption technologies aligned with polyaniline-based materials. Investigate the potential of different materials, such as carbon-based nanomaterials or natural adsorbents like activated carbon, for removing emerging pollutants.

7. Tailoring Adsorbents for Specific Pollutants: Tailor adsorbent materials for specific emerging pollutants commonly found in different regions or industries. This could involve modifying the adsorbent structure to target a broader range of contaminants effectively.
8. Integration of Adsorption Processes: Explore the integration of adsorption processes with other water treatment technologies, such as membrane filtration, coagulation, or advanced oxidation processes, to enhance overall treatment efficiency.
9. Regulatory Framework Development: Advocate for the development and implementation of regulatory frameworks that address emerging pollutants and set guidelines for the use of innovative water treatment technologies. Collaboration with regulatory agencies and policymakers is essential.
10. Public Awareness and Education: Raise public awareness about the importance of clean water and the challenges posed by emerging pollutants. Education and outreach efforts can contribute to responsible water use and pollution prevention.

In conclusion, our research represents a significant step towards developing sustainable and effective solutions for water pollution control. By following these recommendations and continuing to explore innovative approaches, we can work towards ensuring access to clean water while minimising the environmental impact and resource inefficiencies associated with water treatment processes.

Appendices

Appendix I: Table showing Custom design matrix table experimental and predicted data

Run	Coded Variables	Natural Variables					RE (%)		q_e(mg/g)	
	$x_1x_2x_3x_4x_5$	ξ_1	ξ_2	ξ_3	ξ_4	ξ_5	Exp	Pred	Exp	Pred
1	L1+ + + −	VSPANI	70	10	1.0	5	39.59	35.34	110.87	104.77
2	L1+ + − −	VSPANI	70	10	0.2	5	43.78	43.99	122.59	108.68
3	L2− − + −	CMC/PANI	5	3	1.0	5	4.62	5.30	0.92	-14.45
4	L2+ + − +	CMC/PANI	70	10	0.2	15	42.04	45.24	39.24	56.48
5	L3− + − −	DCMC(A)/PANI	5	10	0.2	5	24.13	26.51	4.83	8.11
6	L3+ − + +	DCMC(A)/PANI	70	3	1.0	15	42.37	45.48	39.54	35.34
7	L2+ − − −	CMC/PANI	70	3	0.2	5	14.73	12.84	41.25	51.13
8	L3+ − + −	DCMC(A)/PANI	70	3	1.0	5	13.67	14.92	38.28	47.93
9	L3− + − +	DCMC(A)/PANI	5	10	0.2	15	63.82	57.07	4.25	-4.48
10	L1− − − +	VSPANI	5	3	0.2	15	63.76	73.82	4.25	16.46
11	L4− + + −	DCMC(B)/PANI	5	10	1.0	5	34.75	41.93	6.95	22.21
12	L4− − − −	DCMC(B)/PANI	5	3	0.2	5	54.29	48.74	10.86	8.17
13	L1− − + +	VSPANI	5	3	1.0	15	71.18	65.17	4.75	12.55
14	L4+ − − +	DCMC(B)/PANI	70	3	0.2	15	79.85	78.20	74.52	57.25
15	L2− + + +	CMC/PANI	5	10	1.0	15	39.68	37.69	2.65	-9.10
16	L4+ + + +	DCMC(B)/PANI	70	10	1.0	15	71.35	71.38	66.59	71.29

(RE = removal efficiency, q_e = adsorption capacity, Exp = experimental, Pred = predicted)

Appendix II: Table showing DSD matrix table with the experimental and predicted data

Run	Coded Variables	Natural Variables						RE (%)		q_e (mg/g)	
	$x_1x_2x_3x_4x_5x_6$	ξ_1	ξ_2	ξ_3	ξ_4	ξ_5	ξ_6	Exp	Pred	Exp	Pred
1	L4 0 + + + +	DCMC(B)/PANI	45	10	1.00	15	20	63.92	63.24	38.35	37.85
2	L1− − + + 0	VSPANI	5	3.0	1.00	15	15	84.31	81.41	4.22	4.07
3	L4+ + − − 0	DCMC(B)/PANI	85	10	0.16	5	15	43.86	42.20	111.85	107.15
4	L1−0 − − +	VSPANI	5	6.5	0.16	5	20	54.03	57.68	10.81	11.51
5*	L1 0 0 0 0 0	VSPANI	45	6.5	0.58	10	15	69.08	66.92	46.63	45.26
6	L4− − + − +	DCMC(B)/PANI	5	3.0	1.00	5	20	60.78	57.68	12.16	11.51
7	L1+ + − + −	VSPANI	85	10	0.16	15	10	78.04	74.35	44.22	42.34
8	L1− + + 0 −	VSPANI	5	10	1.00	10	10	83.99	82.52	4.20	4.21
9	L1+ − 0 + +	VSPANI	85	3.0	0.58	15	20	58.20	62.49	65.96	70.33
10	L1− + − + +	VSPANI	5	10	0.16	15	20	79.63	79.73	5.31	5.28
11*	L4 0 0 0 0 0	DCMC(B)/PANI	45	6.5	0.58	10	15	60.20	66.92	40.64	45.26
12	L1 0 − − − −	VSPANI	45	3.0	0.16	5	10	49.61	45.72	44.65	41.85
13	L1 + 0 + + −	VSPANI	85	6.5	1.00	15	10	74.21	74.35	42.05	42.34
14	L4 − − − + −	DCMC(B)/PANI	5	3.0	0.16	15	10	79.04	81.76	2.63	2.70
15	L4+ − + − −	DCMC(B)/PANI	85	3.0	1.00	5	10	42.28	47.47	71.88	77.18
16	L4 + − − 0 +	DCMC(B)/PANI	85	3.0	0.16	10	20	63.93	60.83	108.69	100.26
17	L1+ + + − +	VSPANI	85	10	1.00	5	20	36.77	35.61	125.02	128.21
18	L4− + 0 − 0	DCMC(B)/PANI	5	10	0.58	5	10	58.71	59.71	5.87	5.89

*(RE = removal efficiency, q_e = adsorption capacity, Exp = experimental, Pred = predicted *centre runs)*

Appendix III: Figure showing villi-like structures on the surface of VSPANI

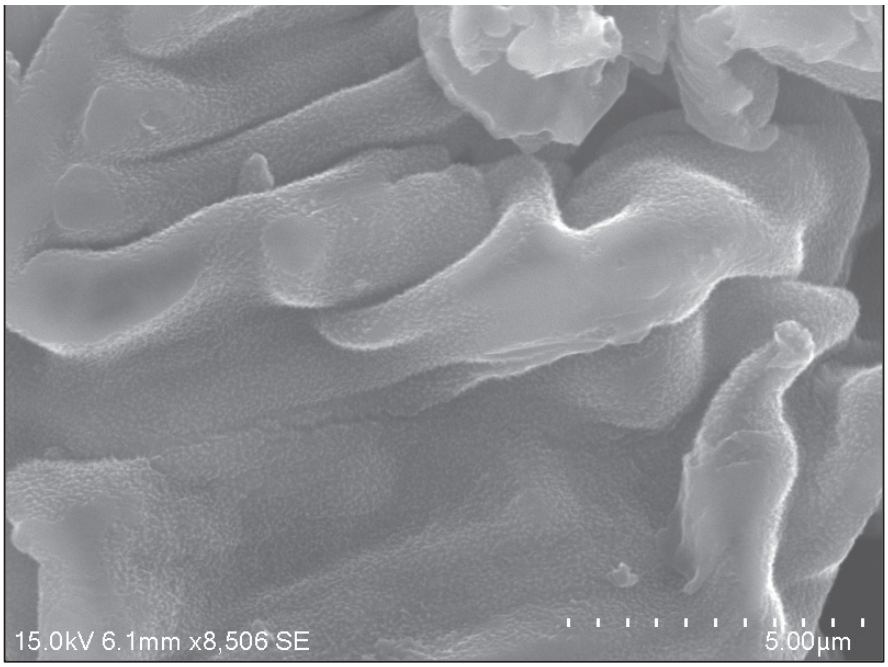

Appendix IV: Table Showing Analysis of Variance (ANOVA *P=0.05*) for the diameters of the prepared microbeads

	Sum of Squares	df	Mean Square	F	Sig.
Between Groups	16.771	7	2.396	147.201	.000
Within Groups	6.380	392	0.016		
Total	23.151	399			

df = degrees of freedom, sig. significant at 0.05

Appendix V: Table showing a Tukey HSD Post Hoc analysis from ANOVA of the prepared microbeads

Microbeads (I)	Microbeads (J)	Mean Difference (I-J)	Std. Error	Sig.	95% Confidence Interval	
					Lower Bound	Upper Bound
CMC-Cu(a)	PANI/CMC-Cu(a)	.10846*	.02552	.001	.0307	.1862
	Cu-BDC/CMC-Cu(a)	.28968*	.02552	.000	.2119	.3674
	Cu-BDC/PANI/CMC-Cu(a)	.51740*	.02552	.000	.4396	.5952
	CMC-Cu(n)	.01038	.02552	1.000	-.0674	.0881
	PANI/CMC-Cu(n)	-.18756*	.02552	.000	-.2653	-.1098
	Cu-BDC/CMC-Cu(n)	.22200*	.02552	.000	.1442	.2998
	Cu-BDC/PANI/CMC-Cu(n)	-.01100	.02552	1.000	-.0888	.0668
PANI/CMC-Cu(a)	CMC-Cu(a)	-.10846*	.02552	.001	-.1862	-.0307
	Cu-BDC/CMC-Cu(a)	.18122*	.02552	.000	.1035	.2590
	Cu-BDC/PANI/CMC-Cu(a)	.40894*	.02552	.000	.3312	.4867
	CMC-Cu(n)	-.09808*	.02552	.004	-.1758	-.0203
	PANI/CMC-Cu(n)	-.29602*	.02552	.000	-.3738	-.2183
	Cu-BDC/CMC-Cu(n)	.11354*	.02552	.000	.0358	.1913
	Cu-BDC/PANI/CMC-Cu(n)	-.11946*	.02552	.000	-.1972	-.0417
Cu-BDC/CMC-Cu(a)	CMC-Cu(a)	-.28968*	.02552	.000	-.3674	-.2119
	PANI/CMC-Cu(a)	-.18122*	.02552	.000	-.2590	-.1035
	Cu-BDC/PANI/CMC-Cu(a)	.22772*	.02552	.000	.1500	.3055
	CMC-Cu(n)	-.27930*	.02552	.000	-.3571	-.2015
	PANI/CMC-Cu(n)	-.47724*	.02552	.000	-.5550	-.3995
	Cu-BDC/CMC-Cu(n)	-.06768	.02552	.141	-.1454	.0101
	Cu-BDC/PANI/CMC-Cu(n)	-.30068*	.02552	.000	-.3784	-.2229
Cu-BDC/PANI/CMC-Cu(a)	CMC-Cu(a)	-.51740*	.02552	.000	-.5952	-.4396
	PANI/CMC-Cu(a)	-.40894*	.02552	.000	-.4867	-.3312
	Cu-BDC/CMC-Cu(a)	-.22772*	.02552	.000	-.3055	-.1500
	CMC-Cu(n)	-.50702*	.02552	.000	-.5848	-.4293
	PANI/CMC-Cu(n)	-.70496*	.02552	.000	-.7827	-.6272
	Cu-BDC/CMC-Cu(n)	-.29540*	.02552	.000	-.3732	-.2176
	Cu-BDC/PANI/CMC-Cu(n)	-.52840*	.02552	.000	-.6062	-.4506

CMC-Cu(n)	CMC-Cu(a)	-.01038	.02552	1.000	-.0881	.0674
	PANI/CMC-Cu(a)	.09808*	.02552	.004	.0203	.1758
	Cu-BDC/CMC-Cu(a)	.27930*	.02552	.000	.2015	.3571
	Cu-BDC/PANI/CMC-Cu(a)	.50702*	.02552	.000	.4293	.5848
	PANI/CMC-Cu(n)	-.19794*	.02552	.000	-.2757	-.1202
	Cu-BDC/CMC-Cu(n)	.21162*	.02552	.000	.1339	.2894
	Cu-BDC/PANI/CMC-Cu(n)	-.02138	.02552	.991	-.0991	.0564
PANI/CMC-Cu(n)	CMC-Cu(a)	.18756*	.02552	.000	.1098	.2653
	PANI/CMC-Cu(a)	.29602*	.02552	.000	.2183	.3738
	Cu-BDC/CMC-Cu(a)	.47724*	.02552	.000	.3995	.5550
	Cu-BDC/PANI/CMC-Cu(a)	.70496*	.02552	.000	.6272	.7827
	CMC-Cu(n)	.19794*	.02552	.000	.1202	.2757
	Cu-BDC/CMC-Cu(n)	.40956*	.02552	.000	.3318	.4873
	Cu-BDC/PANI/CMC-Cu(n)	.17656*	.02552	.000	.0988	.2543
Cu-BDC/CMC-Cu(n)	CMC-Cu(a)	-.22200*	.02552	.000	-.2998	-.1442
	PANI/CMC-Cu(a)	-.11354*	.02552	.000	-.1913	-.0358
	Cu-BDC/CMC-Cu(a)	.06768	.02552	.141	-.0101	.1454
	Cu-BDC/PANI/CMC-Cu(a)	.29540*	.02552	.000	.2176	.3732
	CMC-Cu(n)	-.21162*	.02552	.000	-.2894	-.1339
	PANI/CMC-Cu(n)	-.40956*	.02552	.000	-.4873	-.3318
	Cu-BDC/PANI/CMC-Cu(n)	-.23300*	.02552	.000	-.3108	-.1552
Cu-BDC/PANI/CMC-Cu(n)	CMC-Cu(a)	.01100	.02552	1.000	-.0668	.0888
	PANI/CMC-Cu(a)	.11946*	.02552	.000	.0417	.1972
	Cu-BDC/CMC-Cu(a)	.30068*	.02552	.000	.2229	.3784
	Cu-BDC/PANI/CMC-Cu(a)	.52840*	.02552	.000	.4506	.6062
	CMC-Cu(n)	.02138	.02552	.991	-.0564	.0991
	PANI/CMC-Cu(n)	-.17656*	.02552	.000	-.2543	-.0988
	Cu-BDC/CMC-Cu(n)	.23300*	.02552	.000	.1552	.3108

*. The mean difference is significant at the 0.05 level.

Appendix VI: Figure showing a close-up of the rice-like crystals on the surface of acetate-prepared microbeads (A) and spherical nanomaterials on nitrate-prepared microbeads (N).

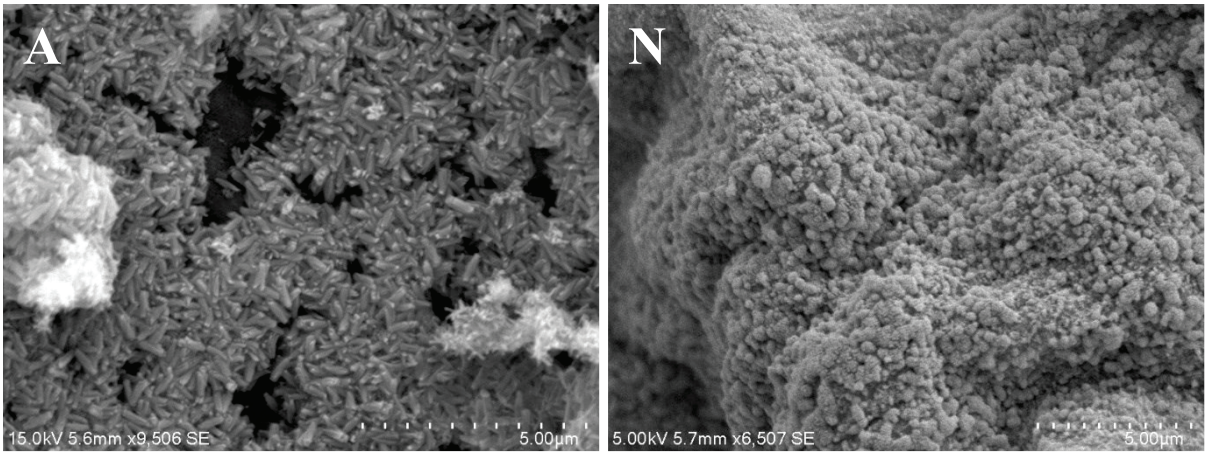

Appendix VII: Figure showing urchin-like spherical particles located inside the Cu-BDC/PANI/Cu-CMC(n) microbeads.

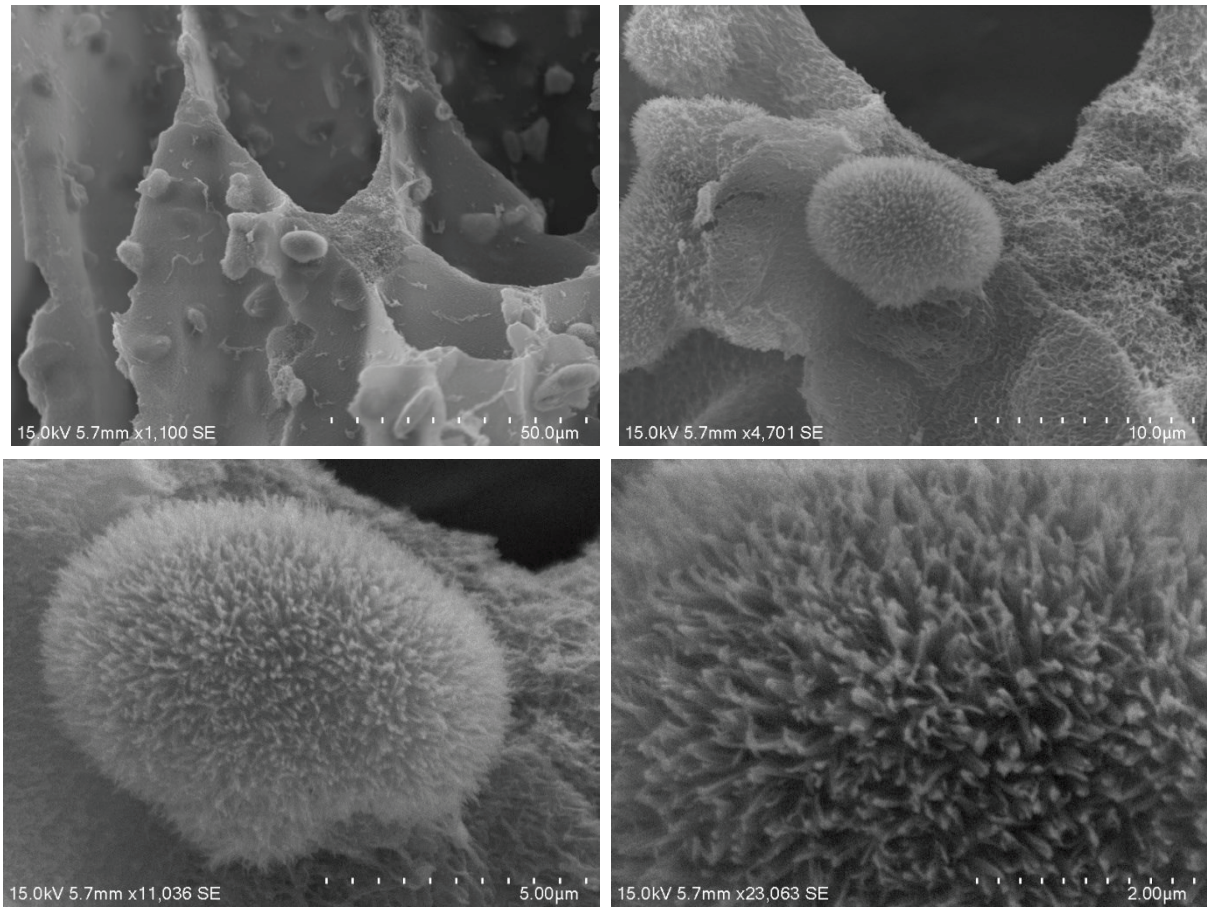

References

Acuña, V., Ginebreda, A., Mor, J. R., Petrovic, M., Sabater, S., Sumpter, J., & Barceló, D. (2015). Balancing the health benefits and environmental risks of pharmaceuticals: Diclofenac as an example. *Environment International*, *85*, 327–333. https://doi.org/10.1016/J.ENVINT.2015.09.023

Agi, A., Junin, R., Jaafar, M. Z., Majid, Z. A., Amin, N. A. S., Sidek, M. A., Yakasai, F., Zaini, M. A. A., Faizal, A. N. M., Gbadamosi, A., Sirajo, L., & Oseh, J. (2023). Dynamic stabilization of formation fines to enhance oil recovery of a medium permeability sandstone core at reservoir conditions. *Journal of Molecular Liquids*, *371*, 121107. https://doi.org/10.1016/j.molliq.2022.121107

Ahamad, A., Madhav, S., Singh, A. K., Kumar, A., & Singh, P. (2020). *Types of Water Pollutants: Conventional and Emerging*. 21–41. https://doi.org/10.1007/978-981-15-0671-0_3

Ahmed, M. J., & Hameed, B. H. (2018). Removal of emerging pharmaceutical contaminants by adsorption in a fixed-bed column: A review. *Ecotoxicology and Environmental Safety*, *149*, 257–266. https://doi.org/10.1016/J.ECOENV.2017.12.012

Ahmed, S. F., Mehejabin, F., Momtahin, A., Tasannum, N., Faria, N. T., Mofijur, M., Hoang, A. T., Vo, D. V. N., & Mahlia, T. M. I. (2022). Strategies to improve membrane performance in wastewater treatment. *Chemosphere*, *306*, 135527. https://doi.org/10.1016/J.CHEMOSPHERE.2022.135527

Ahmed, S., Khan, F. S. A., Mubarak, N. M., Khalid, M., Tan, Y. H., Mazari, S. A., Karri, R. R., & Abdullah, E. C. (2021). Emerging pollutants and their removal using visible-light responsive photocatalysis – A comprehensive review. *Journal of Environmental Chemical Engineering*, *9*(6), 106643. https://doi.org/10.1016/J.JECE.2021.106643

Albadarin, A. B., Mangwandi, C., Al-Muhtaseb, A. H., Walker, G. M., Allen, S. J., & Ahmad, M. N. M. (2012). Modelling and fixed bed column adsorption of Cr(VI) onto orthophosphoric acid-activated lignin. *Chinese Journal of Chemical Engineering*, *20*(3), 469–477. https://doi.org/10.1016/S1004-9541(11)60208-5

Al-Ghouti, M. A., & Da'ana, D. A. (2020). Guidelines for the use and interpretation of adsorption isotherm models: A review. *Journal of Hazardous Materials*, *393*, 122383. https://doi.org/10.1016/J.JHAZMAT.2020.122383

Al-Ghouti, M. A., Khraisheh, M. A. M., Ahmad, M. N., & Allen, S. J. (2007). Microcolumn studies of dye adsorption onto manganese oxides modified diatomite. *Journal of Hazardous Materials*, *146*(1–2), 316–327. https://doi.org/10.1016/J.JHAZMAT.2006.12.024

Ali, I. (2012). New generation adsorbents for water treatment. *Chemical Reviews*, *112*(10), 5073–5091. https://doi.org/10.1021/CR300133D/ASSET/IMAGES/CR300133D.SOCIAL.JPEG_V03

Ali, I., & Gupta, V. K. (2007a). Advances in water treatment by adsorption technology. *Nature Protocols 2007 1:6*, *1*(6), 2661–2667. https://doi.org/10.1038/nprot.2006.370

Ali, I., & Gupta, V. K. (2007b). Advances in water treatment by adsorption technology. *Nature Protocols*, *1*(6), 2661–2667. https://doi.org/10.1038/nprot.2006.370

Allouss, D., Essamlali, Y., Amadine, O., Chakir, A., & Zahouily, M. (2019). Response surface methodology for optimization of methylene blue adsorption onto carboxymethyl cellulose-based hydrogel beads: adsorption kinetics, isotherm, thermodynamics and reusability studies. *RSC Advances*, *9*(65), 37858–37869. https://doi.org/10.1039/C9RA06450H

Al-Maqdi, K. A., Elmerhi, N., Athamneh, K., Bilal, M., Alzamly, A., Ashraf, S. S., & Shah, I. (2021). Challenges and Recent Advances in Enzyme-Mediated Wastewater Remediation—A Review. *Nanomaterials 2021, Vol. 11, Page 3124*, *11*(11), 3124. https://doi.org/10.3390/NANO11113124

Alsharhan, A. S., & Rizk, Z. E. (2020). *Overview on Global Water Resources*. 17–61. https://doi.org/10.1007/978-3-030-31684-6_2

Amrita Nighojkar, Karl Zimmermann, Mohamed Ateia, Benoit Barbeau, Madjid Mohseni, Satheesh Krishnamurthy, Fuhar Dixit, & Balasubramanian Kandasubramanian. (2023). Application of neural network in metal adsorption using biomaterials (BMs): a review. *Environmental Science: Advances*, *2*(1), 11–38. https://doi.org/10.1039/D2VA00200K

Amundson, N. R. (1948). A note on the mathematics of adsorption in beds. *Journal of Physical and Colloid Chemistry*, *52*(7), 1153–1157. https://doi.org/10.1021/j150463a007

Anastas, P., & Eghbali, N. (2009). Green Chemistry: Principles and Practice. *Chemical Society Reviews*, *39*(1), 301–312. https://doi.org/10.1039/B918763B

Anisimov, Y. A., Evitts, R. W., Cree, D. E., & Wilson, L. D. (2021). Polyaniline/Biopolymer Composite Systems for Humidity Sensor Applications: A Review. *Polymers 2021, Vol. 13, Page 2722*, *13*(16), 2722. https://doi.org/10.3390/POLYM13162722

Anton, A. M., Frenzel, F., Yuan, J., Tress, M., & Kremer, F. (2020). Hydrogen bonding and charge transport in a protic polymerized ionic liquid. *Soft Matter*, *16*(26), 6091–6101. https://doi.org/10.1039/d0sm00337a

Apiratikul, R., & Chu, K. H. (2021). Improved fixed bed models for correlating asymmetric adsorption breakthrough curves. *Journal of Water Process Engineering*, *40*, 101810. https://doi.org/10.1016/j.jwpe.2020.101810

Asere, T. G., Mincke, S., Folens, K., vanden Bussche, F., Lapeire, L., Verbeken, K., van der Voort, P., Tessema, D. A., du Laing, G., & Stevens, C. v. (2019). Dialdehyde carboxymethyl cellulose cross-linked chitosan for the recovery of palladium and platinum from aqueous solution. *Reactive and Functional Polymers*, *141*, 145–154. https://doi.org/10.1016/J.REACTFUNCTPOLYM.2019.05.008

Asfaram, A., Ghaedi, M., Agarwal, S., Tyagi, I., & Gupta, V. K. (2015). Removal of basic dye Auramine-O by ZnS:Cu nanoparticles loaded on activated carbon: optimization of parameters using response surface methodology with central composite design. *RSC Advances*, *5*(24), 18438–18450. https://doi.org/10.1039/C4RA15637D

Azad, F. N., Ghaedi, M., Asfaram, A., Jamshidi, A., Hassani, G., Goudarzi, A., Azqhandi, M. H. A., & Ghaedi, A. (2016). Optimization of the process parameters for the adsorption of ternary dyes by Ni doped FeO(OH)-NWs–AC using response surface methodology and an artificial neural network. *RSC Advances*, *6*(24), 19768–19779. https://doi.org/10.1039/C5RA26036A

Balsamo, M., & Montagnaro, F. (2015). Fractal-like vermeulen kinetic equation for the description of diffusion-controlled adsorption dynamics. *Journal of Physical Chemistry C*, *119*(16), 8781–8785. https://doi.org/10.1021/acs.jpcc.5b01783

Banza, M., & Rutto, H. (2022). Continuous fixed-bed column study and adsorption modeling removal of Ni2+, Cu2+, Zn2+ and Cd2+ ions from synthetic acid mine drainage by nanocomposite cellulose hydrogel. *Journal of Environmental Science and Health, Part A*, *57*(2), 117–129. https://doi.org/10.1080/10934529.2022.2036552

Barbosa, M. O., Moreira, N. F. F., Ribeiro, A. R., Pereira, M. F. R., & Silva, A. M. T. (2016). Occurrence and removal of organic micropollutants: An overview of the watch list of EU Decision 2015/495. *Water Research*, *94*, 257–279. https://doi.org/10.1016/J.WATRES.2016.02.047

Basheer, A. A. (2018). New generation nano-adsorbents for the removal of emerging contaminants in water. *Journal of Molecular Liquids*, *261*, 583–593. https://doi.org/10.1016/J.MOLLIQ.2018.04.021

Bhandari, S. (2018). Polyaniline: Structure and Properties Relationship. In *Polyaniline Blends, Composites, and Nanocomposites* (pp. 23–60). Elsevier. https://doi.org/10.1016/B978-0-12-809551-5.00002-3

Boeva, Z. A., & Sergeyev, V. G. (2014). Polyaniline: Synthesis, properties, and application. *Polymer Science Series C 2014 56:1*, *56*(1), 144–153. https://doi.org/10.1134/S1811238214010032

Bohart, G. S., & Adams, E. Q. (1920). Some aspects of the behavior of charcoal with respect to chlorine. *Journal of the American Chemical Society*, *42*(3), 523–544. https://doi.org/10.1021/ja01448a018

Bolong, N., Ismail, A. F., Salim, M. R., & Matsuura, T. (2009). A review of the effects of emerging contaminants in wastewater and options for their removal. *Desalination*, *239*(1–3), 229–246. https://doi.org/10.1016/J.DESAL.2008.03.020

Boutaleb, Y., Zerdoum, R., Bensid, N., Abumousa, R. A., Hattab, Z., & Bououdina, M. (2022). Adsorption of Cr(VI) by Mesoporous Pomegranate Peel Biowaste from Synthetic Wastewater under Dynamic Mode. *Water 2022*, *14*(23), 3885. https://doi.org/10.3390/w14233885

Buser, H. R., Poiger, T., & Müller, M. D. (1998). Occurrence and Fate of the Pharmaceutical Drug Diclofenac in Surface Waters: Rapid Photodegradation in a Lake. *Environmental Science and Technology*, *32*(22), 3449–3456. https://doi.org/10.1021/ES980301X

Cai, Z. Y., Pei, L. Z., Pei, Y. Q., -, al, Xie, Y. K., Bleda-Martínez, M. J., Peng, C., Zhang, S., Budi, S., Juliana, A., Cahyana, U., Purwanto, A., Imaduddin, A., & Handoko, E. (2018). Preparation of high surface area and high conductivity polyaniline nanoparticles using chemical oxidation polymerization technique. *Journal of Physics: Conference Series*, *983*(1), 012162. https://doi.org/10.1088/1742-6596/983/1/012162

Chakraborty, A., & Naskar, M. K. (2022). Sol–gel synthesis of alumina gel@zeolite X nanocomposites for high performance water defluoridation: batch and column adsorption study. *Materials Advances*, *3*(23), 8544–8556. https://doi.org/10.1039/d2ma00392a

Chatterjee, A., & Schiewer, S. (2011). Biosorption of Cadmium(II) Ions by Citrus Peels in a Packed Bed Column: Effect of Process Parameters and Comparison of Different Breakthrough Curve Models. *Clean Soil Air Water*, *39*(9), 874–881. https://doi.org/10.1002/clen.201000482

Cheng, Y., Wang, X., Jia, C., Wang, Y., Zhai, L., Wang, Q., & Zhao, D. (2017). Ultrathin mixed matrix membranes containing two-dimensional metal-organic framework nanosheets for efficient CO2/CH4 separation. *Journal of Membrane Science*, *539*, 213–223. https://doi.org/10.1016/J.MEMSCI.2017.06.011

Chinnathambi, A., & Alahmadi, T. A. (2021). Facile synthesis of Fe3O4 anchored polyaniline intercalated graphene oxide as an effective adsorbent for the removal of hexavalent chromium and phosphate ions. *Chemosphere*, *272*, 129851. https://doi.org/10.1016/J.CHEMOSPHERE.2021.129851

Chu, K. H. (2004). Improved fixed bed models for metal biosorption. *Chemical Engineering Journal*, *97*(2–3), 233–239. https://doi.org/10.1016/s1385-8947(03)00214-6

Chu, K. H. (2010). Fixed bed sorption: setting the record straight on the Bohart-Adams and Thomas models. *Journal of Hazardous Materials*, *177*(1–3), 1006–1012. https://doi.org/10.1016/j.jhazmat.2010.01.019

Chu, K. H. (2020a). Breakthrough curve analysis by simplistic models of fixed bed adsorption: In defense of the century-old Bohart-Adams model. *Chemical Engineering Journal*, *380*, 122513. https://doi.org/10.1016/j.cej.2019.122513

Chu, K. H. (2020b). Fitting the Gompertz equation to asymmetric breakthrough curves. *Journal of Environmental Chemical Engineering*, *8*(3), 103713. https://doi.org/10.1016/j.jece.2020.103713

Chu, K. H. (2020c). Rebuttal to comment on "Breakthrough curve analysis by simplistic models of fixed bed adsorption: in defense of the century-old Bohart-Adams model." *Chemical Engineering Journal*, *398*, 125546. https://doi.org/10.1016/j.cej.2020.125546

Chu, K. H. (2021a). Fixed bed adsorption of chromium and the Weibull function. *Journal of Hazardous Materials Letters*, *2*, 100022. https://doi.org/10.1016/j.hazl.2021.100022

Chu, K. H. (2021b). Using Probability Distribution Functions to Correlate Breakthrough Curves of Water and air Contaminants. *Research Square*, *Preprint*((Version 1)). https://doi.org/10.21203/rs.3.rs-441731/v1

Chu, K. H. (2022). Fixed Bed Adsorption of Water Contaminants: A Cautionary Guide to Simple Analytical Models and Modeling Misconceptions. *Separation & Purification Review*. https://doi.org/10.1080/15422119.2022.2039196

Chu, K. H., & Hashim, M. A. (2022). Fixed bed adsorption of water and air contaminants: analysis of breakthrough curves using probability distribution functions. *Chemical Engineering Communications*. https://doi.org/10.1080/00986445.2022.2116325

Clark, R. M. (1987). Evaluating the Cost and Performance of Field-Scale Granular Activated Carbon Systems. *Environmental Science and Technology*, *21*(6), 573–580. https://doi.org/doi.org/10.1021/es00160a008

Cohen, J. (1990). Things I have learned (so far). *American Psychologist*, *45*(12), 1304–1312. https://doi.org/10.1037/0003-066X.45.12.1304

Commoner, B. (1972). *The closing circle; nature, man, and technology.* Bantam Books.

Cooney, D. O. (1991). The Importance Of Axial Dispersion In Liquid-Phase Fixed-Bed Adsorption Operations. *Chemical Engineering Communications*, *110*(1), 217–231. https://doi.org/10.1080/00986449108939951

Corrales, J., Kristofco, L. A., Baylor Steele, W., Yates, B. S., Breed, C. S., Spencer Williams, E., & Brooks, B. W. (2015). Global Assessment of Bisphenol A in the Environment: Review and Analysis of Its Occurrence and Bioaccumulation. *Dose-Response*, *13*(3), 1–29. https://doi.org/10.1177/1559325815598308

Cox, V. (2017). Design of Experiments. In *Translating Statistics to Make Decisions* (1st ed., pp. 1–31). Apress, Berkeley, CA. https://doi.org/10.1007/978-1-4842-2256-0_1

Crini, G., & Lichtfouse, E. (2019). Advantages and disadvantages of techniques used for wastewater treatment. *Environmental Chemistry Letters*, *17*(1), 145–155. https://doi.org/10.1007/S10311-018-0785-9/TABLES/1

Crittenden, J. C., Berrigan, J. K., & Hand, D. W. (1986). Design of Rapid Small-Scale Adsorption Tests for a Constant Diffusivity on JSTOR. *Water Pollution Control Federation*, *58*(4), 312–319. https://www.jstor.org/stable/25042907

Czitrom, V. (1999). One-factor-at-a-time versus designed experiments. *American Statistician*, *53*(2), 126–131. https://doi.org/10.1080/00031305.1999.10474445

da Silva Almeida, A. E., de Souza, G. R., Corrêa, F. V., e Silva, J. R. M., de Oliveira, L. F. C., & Freire, E. R. C. G. (2021). Iron removal by fixed-bed adsorption with thermochemically treated Lithothamnium calcareum algae. *Environmental Technology & Innovation*, *24*, 101888. https://doi.org/10.1016/j.eti.2021.101888

Dąbrowski, A. (2001). Adsorption — from theory to practice. *Advances in Colloid and Interface Science*, *93*(1–3), 135–224. https://doi.org/10.1016/S0001-8686(00)00082-8

Daughton, C. C. (2001). Pharmaceuticals and personal care products in the environment: Overarching issues and overview. *ACS Symposium Series*, *791*, 2–38. https://doi.org/10.1021/BK-2001-0791.CH001

de Aguiar, P. F., Bourguignon, B., Khots, M. S., Massart, D. L., & Phan-Than-Luu, R. (1995). D-optimal designs. *Chemometrics and Intelligent Laboratory Systems*, *30*(2), 199–210. https://doi.org/10.1016/0169-7439(94)00076-X

de Araújo, T. P., Quesada, H. B., dos Santos, D. F., da Silva Fonseca, B. C., Barbieri, J. Z., Bergamasco, R., & de Barros, M. A. S. D. (2022). Acetaminophen removal by calcium alginate/activated hydrochar composite beads: Batch and fixed-bed studies. *International Journal of Biological Macromolecules*, *203*, 553–562. https://doi.org/10.1016/j.ijbiomac.2022.01.177

Deng, Y., & Zhao, R. (2015). Advanced Oxidation Processes (AOPs) in Wastewater Treatment. *Current Pollution Reports*, *1*(3), 167–176. https://doi.org/10.1007/S40726-015-0015-Z/TABLES/2

Dichiara, A. B., Weinstein, S. J., & Rogers, R. E. (2015). On the Choice of Batch or Fixed Bed Adsorption Processes for Wastewater Treatment. *Industrial and Engineering Chemistry Research*, *54*(34), 8579–8586. https://doi.org/doi.org/10.1021/acs.iecr.5b02350

Dima, J. B., Ferrari, M., & Zaritzky, N. (2020). Mathematical Modeling of Fixed-Bed Columns Adsorption: Hexavalent Chromium onto Chitosan Flakes. *Industrial and Engineering Chemistry Research*, *59*(34), 15378–15386. https://doi.org/10.1021/acs.iecr.0c02004

Dougherty, S., Simpson, J. R., Hill, R. R., Pignatiello, J. J., & White, E. D. (2014). Augmentation of definitive screening designs (DSD+). *International Journal of*

Experimental Design and Process Optimisation, *4*(2), 91–115. https://doi.org/10.1504/IJEDPO.2014.066465

Durakovic, B. (2017). Design of experiments application, concepts, examples: State of the art. *Periodicals of Engineering and Natural Sciences*, *5*(3), 421–439. https://doi.org/10.21533/PEN.V5I3.145

Ekande, O. S., & Kumar, M. (2023). Antibiotics Removal via Novel N-Doped Carbon Derived from Carbonization of Different Forms of Polyaniline. *Journal of Hazardous, Toxic, and Radioactive Waste*, *27*(3), 04023010. https://doi.org/10.1061/JHTRBP.HZENG-1204

Ernest, M. V., Whitley, R. D., Ma, Z., & Wang, N. H. L. (1997). Effects of Mass Action Equilibria on Fixed-Bed Multicomponent Ion-Exchange Dynamics. *Industrial and Engineering Chemistry Research*, *36*(1), 212–226. https://doi.org/10.1021/ie960167u

Eskandari, E., Kosari, M., Davood Abadi Farahani, M. H., Khiavi, N. D., Saeedikhani, M., Katal, R., & Zarinejad, M. (2020). A review on polyaniline-based materials applications in heavy metals removal and catalytic processes. *Separation and Purification Technology*, *231*, 115901. https://doi.org/10.1016/J.SEPPUR.2019.115901

Fisher, J. B. (1980). R.A. Fisher and the Design of Experiments, 1922–1926. *The American Statistician*, *34*(1), 1–7. https://doi.org/10.1080/00031305.1980.10482701

Fisher, R. A., Box, J. F., & Fisher Box, J. (1980). R.A. Fisher and the Design of Experiments, 1922–1926. *The American Statistician*, *34*(1), 1–7. https://doi.org/10.1080/00031305.1980.10482701

Fonseca, L. M., Domingues, J. P., & Dima, A. M. (2020). Mapping the Sustainable Development Goals Relationships. *Sustainability 2020, Vol. 12, Page 3359*, *12*(8), 3359. https://doi.org/10.3390/SU12083359

Gadekar, M. R., & Ahammed, M. M. (2019). Modelling dye removal by adsorption onto water treatment residuals using combined response surface methodology-artificial neural network approach. *Journal of Environmental Management*, *231*, 241–248. https://doi.org/10.1016/J.JENVMAN.2018.10.017

Galligan, T. H., Mallord, J. W., Prakash, V. M., Bhusal, K. P., Alam, A. B. M. S., Anthony, F. M., Dave, R., Dube, A., Shastri, K., Kumar, Y., Prakash, N., Ranade, S., Shringarpure, R., Chapagain, D., Chaudhary, I. P., Joshi, A. B., Paudel, K., Kabir, T., Ahmed, S., … Green, R. E. (2021). Trends in the availability of the vulture-toxic drug, diclofenac, and other

NSAIDs in South Asia, as revealed by covert pharmacy surveys. *Bird Conservation International*, *31*(3), 337–353. https://doi.org/10.1017/S0959270920000477

Gao, H., Yang, B. J., Li, N., Feng, L. M., Shi, X. Y., Zhao, W. H., & Liu, S. J. (2015). Bisphenol A and Hormone-Associated Cancers: Current Progress and Perspectives. *Medicine*, *94*(1), e211. https://doi.org/10.1097/MD.0000000000000211

Gao, Y., Chen, C., Tan, X., Xu, H., & Zhu, K. (2016). Polyaniline-modified 3D-flower-like molybdenum disulfide composite for efficient adsorption/photocatalytic reduction of Cr(VI). *Journal of Colloid and Interface Science*, *476*, 62–70. https://doi.org/10.1016/J.JCIS.2016.05.022

Germain, J., Fréchet, J. M. J., & Svec, F. (2007). Hypercrosslinked polyanilines with nanoporous structure and high surface area: potential adsorbents for hydrogen storage. *Journal of Materials Chemistry*, *17*(47), 4989–4997. https://doi.org/10.1039/B711509A

Ghaedi, A. M., & Vafaei, A. (2017). Applications of artificial neural networks for adsorption removal of dyes from aqueous solution: A review. *Advances in Colloid and Interface Science*, *245*, 20–39. https://doi.org/10.1016/J.CIS.2017.04.015

Gholamali, I. (2020). Facile Preparation of Carboxymethyl Cellulose/Cu Bio-Nanocomposite Hydrogels for Controlled Release of Ibuprofen. *Regenerative Engineering and Translational Medicine*, *6*(2), 115–124. https://doi.org/10.1007/S40883-019-00133-2/SCHEMES/2

Gibson, L. J. (2003). Cellular Solids. *MRS Bulletin*, *28*(4), 270–274. https://doi.org/10.1557/MRS2003.79

Gizaw, A., Zewge, F., Chebude, Y., Mekonnen, A., & Tesfaye, M. (2022). Simultaneous nitrate and phosphate abatement using calcium silicate hydrate adsorbent: Fixed bed column adsorption study. *Surfaces and Interfaces*, *30*, 101961. https://doi.org/10.1016/j.surfin.2022.101961

Gogoi, A., Mazumder, P., Tyagi, V. K., Tushara Chaminda, G. G., An, A. K., & Kumar, M. (2018). Occurrence and fate of emerging contaminants in water environment: A review. *Groundwater for Sustainable Development*, *6*, 169–180. https://doi.org/10.1016/J.GSD.2017.12.009

Gokulakrishnan, S. A., Arthanareeswaran, G., László, Z., Veréb, G., Kertész, S., & Kweon, J. (2021). Recent development of photocatalytic nanomaterials in mixed matrix membrane

for emerging pollutants and fouling control, membrane cleaning process. *Chemosphere*, *281*, 130891. https://doi.org/10.1016/J.CHEMOSPHERE.2021.130891

Gomes, I. B., Maillard, J. Y., Simões, L. C., & Simões, M. (2020). Emerging contaminants affect the microbiome of water systems—strategies for their mitigation. *Npj Clean Water*, *3*(39), 1–11. https://doi.org/10.1038/s41545-020-00086-y

Gompertz, B. (1825). On the nature of the function expressive of the law of human mortality, and on a new mode of determining the value of life contingencies. *Philosophical Transactions of the Royal Society of London*, 513–583. https://doi.org/10.1098/rspl.1815.0271

González-López, M. E., Laureano-Anzaldo, C. M., Pérez-Fonseca, A. A., Arellano, M., & Robledo-Ortíz, J. R. (2021). A discussion on linear and non-linear forms of Thomas equation for fixed-bed adsorption column modeling. *Revista Mexicana de Ingeniería Química*, *20*(2), 875–884. https://doi.org/10.24275/rmiq/Fen2337

Goodman, S. N. (1999). Toward evidence-based medical statistics. 1: The P value fallacy. *Annals of Internal Medicine*, *130*(12), 995–1004. https://doi.org/10.7326/0003-4819-130-12-199906150-00008

Gorman, M. (1957). The evidence from infrared spectroscopy for hydrogen bonding: A case history of the correlation and interpretation of data. *Journal of Chemical Education*, *34*(6), 304–306. https://doi.org/10.1021/ed034p304

Green, R. E., Newton, I., Shultz, S., Cunningham, A. A., Gilbert, M., Pain, D. J., & Prakash, V. (2004). Diclofenac poisoning as a cause of vulture population declines across the Indian subcontinent. *Journal of Applied Ecology*, *41*(5), 793–800. https://doi.org/10.1111/J.0021-8901.2004.00954.X

Gusain, D., Dubey, S., Chandra Sharma, Y., & Bux, F. (2021). Impact of Initial Concentration, Adsorbent Dose, and Ionic Strength on Batch Adsorption of Metals and Anions and Elucidation of the Mechanism. In *Batch Adsorption Process of Metals and Anions for Remediation of Contaminated Water* (pp. 239–248). CRC Press. https://doi.org/10.1201/9781003006367-7

Hahladakis, J. N., Iacovidou, E., & Gerassimidou, S. (2023). An overview of the occurrence, fate, and human risks of the bisphenol-A present in plastic materials, components, and

products. *Integrated Environmental Assessment and Management*, *19*(1), 45–62. https://doi.org/10.1002/IEAM.4611

Harter, R. D. (1984). Curve-fit Errors in Langmuir Adsorption Maxima. *Soil Science Society of America Journal*, *48*(4), 749–752. https://doi.org/10.2136/sssaj1984.03615995004800040010x

Hawkins, D. M. (2004). The Problem of Overfitting. *Journal of Chemical Information and Computer Sciences*, *44*(1), 1–12. https://doi.org/10.1021/CI0342472/ASSET/CI0342472.FP.PNG_V03

Hernando, M. D., Mezcua, M., Fernández-Alba, A. R., & Barceló, D. (2006). Environmental risk assessment of pharmaceutical residues in wastewater effluents, surface waters and sediments. *Talanta*, *69*(2), 334–342. https://doi.org/10.1016/J.TALANTA.2005.09.037

Heydari, S., Saeedeh, ·, & Ahmadi, E. (2022). Fabrication and characterization of polymer based magnetic dialdehyde carboxymethyl cellulose/cysteine nanocomposites for methylene blue removal. *Polymer Bulletin*, *80*, 3857–3882. https://doi.org/10.1007/S00289-022-04210-5

Hill, A. V. (1910). The possible effects of the aggregation of the molecules of haemoglobin on its dissociation curves. *J. Physiol.*, *40*, 4–7. https://cir.nii.ac.jp/crid/1571417125479019264

Hlekelele, L., Nomadolo, N. E., Setshedi, K. Z., Mofokeng, L. E., Chetty, A., & Chauke, V. P. (2019). Synthesis and characterization of polyaniline, polypyrrole and zero-valent iron-based materials for the adsorptive and oxidative removal of bisphenol-A from aqueous solution. *RSC Advances*, *9*(25), 14531–14543. https://doi.org/10.1039/C9RA01666J

Hsini, A., Naciri, Y., Laabd, M., Bouziani, A., Navío, J. A., Puga, F., Boukherroub, R., Lakhmiri, R., & Albourine, A. (2021). Development of a novel PANI@WO3 hybrid composite and its application as a promising adsorbent for Cr(VI) ions removal. *Journal of Environmental Chemical Engineering*, *9*(5), 105885. https://doi.org/10.1016/J.JECE.2021.105885

Hu, Q., Liu, H., Zhang, Z., & Pei, X. (2020). Development of fractal-like Clark model in a fixed-bed column. *Separation and Purification Technology*, *251*, 117396. https://doi.org/10.1016/j.seppur.2020.117396

Hu, Q., Pang, S., Wang, D., Yang, Y., & Liu, H. (2021). Deeper Insights into the Bohart-Adams Model in a Fixed-Bed Column. *Journal of Physical Chemistry B*, *125*(30), 8494–8501. https://doi.org/10.1021/acs.jpcb.1c03378

Hu, Q., Wang, D., Pang, S., & Xu, L. (2022). Prediction of breakthrough curves for multicomponent adsorption in a fixed-bed column using logistic and Gompertz functions. *Arabian Journal of Chemistry*, *15*(9), 104034. https://doi.org/10.1016/j.arabjc.2022.104034

Hu, Q., Xie, Y., Feng, C., & Zhang, Z. (2019). Fractal-like kinetics of adsorption on heterogeneous surfaces in the fixed-bed column. *Chemical Engineering Journal*, *358*, 1471–1478. https://doi.org/10.1016/j.cej.2018.10.165

Hu, Q., & Zhang, Z. (2020). Comment on ″Low-cost chitosan-calcite adsorbent development for potential phosphate removal and recovery from wastewater effluent″. *Water Research*, *179*, 115728. https://doi.org/10.1016/j.watres.2020.115728

Huang, K., Xu, Y., Wang, L., & Wu, D. (2015). Heterogeneous catalytic wet peroxide oxidation of simulated phenol wastewater by copper metal–organic frameworks. *RSC Advances*, *5*(41), 32795–32803. https://doi.org/10.1039/C5RA01707F

Huang, M., Yan, W., Zhang, L., He, Z., Ma, J., Ding, Y., Ou, J., Chen, · Shenggui, Jiang, W., Dai, · Xiyi, Li, Z., & Wei, G. (2022). A Noval Cation–Anion Absorbent of Tannin-Dialdehyde Carboxymethyl Cellulose for Removal of Cr(VI) and Ni(II) from Aqueous Solutions with High Adsorption Capacity. *Journal of Polymers and the Environment*, *30*, 3495–3514. https://doi.org/10.1007/S10924-022-02451-z

Huesemann, M. H. (2001). Can pollution problems be effectively solved by environmental science and technology? An analysis of critical limitations. *Ecological Economics*, *37*(2), 271–287. https://doi.org/10.1016/S0921-8009(00)00283-4

Hwang, D. K., Song, D. M., & Im, S. S. (2018). Synthesis of Villi-Structured Polyaniline Sheets Using Organic Single Crystal Surface-Induced Polymerization. *ACS Omega*, *3*(4), 4181–4186. https://doi.org/10.1021/acsomega.7b01024

ICSU, & ISSC. (2015). *Review of the Sustainable Development Goals: The Science Perspective.* https://council.science/publications/review-of-targets-for-the-sustainable-development-goals-the-science-perspective-2015/

Ihsanullah, I. (2022). Applications of MOFs as adsorbents in water purification: Progress, challenges and outlook. *Current Opinion in Environmental Science & Health*, *26*, 100335. https://doi.org/10.1016/J.COESH.2022.100335

Jiang, X., Yang, Z., Peng, Y., Han, B., Li, Z., Li, X., & Liu, W. (2016). Preparation, characterization and feasibility study of dialdehyde carboxymethyl cellulose as a novel crosslinking reagent. *Carbohydrate Polymers*, *137*, 632–641. https://doi.org/10.1016/j.carbpol.2015.10.078

Jin, X., Talbot, J., & Wang, N. -H L. (1994). Analysis of steric hindrance effects on adsorption kinetics and equilibria. *AIChE Journal*, *40*(10), 1685–1696. https://doi.org/10.1002/aic.690401010

Johnson, M. E., & Jones, B. (2011). Classical design structure of orthogonal designs with six to eight factors and sixteen runs. *Quality and Reliability Engineering International*, *27*(1), 61–70. https://doi.org/10.1002/QRE.1170

Jones, B., & Nachtsheim, C. J. (2011a). A Class of Three-Level Designs for Definitive Screening in the Presence of Second-Order Effects. *Journal of Quality Technology*, *43*(1), 1–15. https://doi.org/10.1080/00224065.2011.11917841

Jones, B., & Nachtsheim, C. J. (2011b). A Class of Three-Level Designs for Definitive Screening in the Presence of Second-Order Effects. *Journal of Quality Technology*, *43*(1), 1–15. https://doi.org/10.1080/00224065.2011.11917841

Jones, B., & Nachtsheim, C. J. (2013). Definitive Screening Designs with Added Two-Level Categorical Factors*. *Journal of Quality Technology*, *45*(2), 121–129. https://doi.org/10.1080/00224065.2013.11917921

Jones, B., & Nachtsheim, C. J. (2017). Effective Design-Based Model Selection for Definitive Screening Designs. *Technometrics*, *59*(3), 319–329. https://doi.org/10.1080/00401706.2016.1234979

Juela, D., Vera, M., Cruzat, C., Alvarez, X., & Vanegas, E. (2021). Mathematical modeling and numerical simulation of sulfamethoxazole adsorption onto sugarcane bagasse in a fixed-bed column. *Chemosphere*, *280*, 130687. https://doi.org/10.1016/j.chemosphere.2021.130687

Kairigo, P., Ngumba, E., Sundberg, L. R., Gachanja, A., & Tuhkanen, T. (2020). Contamination of Surface Water and River Sediments by Antibiotic and Antiretroviral

Drug Cocktails in Low and Middle-Income Countries: Occurrence, Risk and Mitigation Strategies. *Water 2020, Vol. 12, Page 1376*, *12*(5), 1376. https://doi.org/10.3390/W12051376

Kantor, T. G. (1986). Use of diclofenac in analgesia. *The American Journal of Medicine*, *80*(4), 64–69. https://doi.org/10.1016/0002-9343(86)90083-5

Kecili, R., & Hussain, C. M. (2018). Mechanism of Adsorption on Nanomaterials. In C. M. Hussain (Ed.), *Nanomaterials in Chromatography: Current Trends in Chromatographic Research Technology and Techniques* (pp. 89–115). Elsevier. https://doi.org/10.1016/B978-0-12-812792-6.00004-2

Kim, J. J., Kumar, S., Kumar, V., Lee, Y. M., Kim, Y. S., & Kumar, V. (2019). Bisphenols as a Legacy Pollutant, and Their Effects on Organ Vulnerability. *International Journal of Environmental Research and Public Health 2020, Vol. 17, Page 112*, *17*(1), 112. https://doi.org/10.3390/IJERPH17010112

Kimani, P. K., Thiong'o, G. T., & Mwangi, J. K. (2016). Spatial and Seasonal Variation of Selected Water Quality Parameters in Chania River Catchment, Kenya. *Current Journal of Applied Science and Technology*, *18*(3), 1–16. https://doi.org/10.9734/BJAST/2016/30209

Kimani, P. K., Thiong'o, G. T., & Mwangi, J. K. (2020). Water quality as a plausible basis for payment for ecosystem services, the buyer's perspective: Chania River Catchment, Kiambu County, Kenya. *Sustainable Water Resources Management*, *6*(6), 1–11. https://doi.org/10.1007/S40899-020-00472-X/FIGURES/6

Kizildag, N., Ucar, N., Karacan, I., Onen, A., & Demirsoy, N. (2014). The effect of the dissolution process and the polyaniline content on the properties of polyacrylonitrile–polyaniline composite nanoweb. *Journal of Industrial Textiles*, *45*(6), 1548–1570. https://doi.org/10.1177/1528083714564636

Kruger, J. S., & Lewis-Beck, M. W. (2007). Goodness-of-fit: R-squared, SEE and 'best practice.' *The Political Methodologist*, *15*(1), 2–4.

Kulkarni, K., Bhogle, J., Kulkarni, R., & Bari, A. (2022). Investigation and Modeling of Fluoride Ion Adsorption on an Azospirillum Biofertilizer. *Chemical Engineering & Technology*, *45*(11), 2061–2070. https://doi.org/10.1002/ceat.202100549

Kvalheim, O. M., Grung, B., & Rajalahti, T. (2019). Number of components and prediction error in partial least squares regression determined by Monte Carlo resampling strategies. *Chemometrics and Intelligent Laboratory Systems*, *188*, 79–86. https://doi.org/10.1016/J.CHEMOLAB.2019.03.006

Larcher, S., & Yargeau, V. (2012). Biodegradation of sulfamethoxazole: Current knowledge and perspectives. *Applied Microbiology and Biotechnology*, *96*(2), 309–318. https://doi.org/10.1007/S00253-012-4326-3/TABLES/3

Lawson, H. D., Walton, S. P., & Chan, C. (2021). Metal-Organic Frameworks for Drug Delivery: A Design Perspective. *ACS Applied Materials and Interfaces*, *13*(6), 7004–7020. https://doi.org/10.1021/ACSAMI.1C01089/SUPPL_FILE/AM1C01089_SI_001.PDF

Lee, C. G., Kim, J. H., Kang, J. K., Kim, S. B., Park, S. J., Lee, S. H., & Choi, J. W. (2014). Comparative analysis of fixed-bed sorption models using phosphate breakthrough curves in slag filter media. *Desalination and Water Treatment*, *55*(7), 1795–1805. https://doi.org/10.1080/19443994.2014.930698

Lee, T. H. Y., Chuah, J., & Snyder, S. A. (2022). Occurrence of Emerging Contaminants in Southeast Asian Environments: Present Status, Challenges, and Future Prospects. *ACS ES&T Water*, *2*(6), 907–931. https://doi.org/10.1021/acsestwater.1c00453

Lendrem, D., Owen, M., & Godbert, S. (2001). DOE (Design of Experiments) in Development Chemistry: Potential Obstacles. *Organic Process Research and Development*, *5*(3), 324–327. https://doi.org/10.1021/OP000025I

Li, H., Wu, B., Mu, C., & Lin, W. (2011). Concomitant degradation in periodate oxidation of carboxymethyl cellulose. *Carbohydrate Polymers*, *84*(3), 881–886. https://doi.org/10.1016/j.carbpol.2010.12.026

Li, K., Liu, Q., Fang, F., Luo, R., Lu, Q., Zhou, W., Huo, S., Cheng, P., Liu, J., Addy, M., Chen, P., Chen, D., & Ruan, R. (2019). Microalgae-based wastewater treatment for nutrients recovery: A review. *Bioresource Technology*, *291*, 121934. https://doi.org/10.1016/J.BIORTECH.2019.121934

Li, Y., Wang, Y., Fan, W., & Sun, D. (2022). Flexible metal–organic frameworks for gas storage and separation. *Dalton Transactions*, *51*(12), 4608–4618. https://doi.org/10.1039/D1DT03842G

Liu, F. T., Neoh, K. G., Kang, E. T., Li, S., Han, H. S., & Tan, K. L. (1999). Effects of crosslinking on polyaniline films' doping behavior and degradation under weathering. *Polymer*, *40*(19), 5285–5296. https://doi.org/10.1016/S0032-3861(98)00758-7

Liu, J., Zhang, L., Lu, G., Jiang, R., Yan, Z., & Li, Y. (2021). Occurrence, toxicity and ecological risk of Bisphenol A analogues in aquatic environment – A review. *Ecotoxicology and Environmental Safety*, *208*, 111481. https://doi.org/10.1016/J.ECOENV.2020.111481

Lonappan, L., Brar, S. K., Das, R. K., Verma, M., & Surampalli, R. Y. (2016). Diclofenac and its transformation products: Environmental occurrence and toxicity - A review. *Environment International*, *96*, 127–138. https://doi.org/10.1016/J.ENVINT.2016.09.014

Lundstedt, T., Seifert, E., Abramo, L., Thelin, B., Nyström, Å., Pettersen, J., & Bergman, R. (1998). Experimental design and optimization. *Chemometrics and Intelligent Laboratory Systems*, *42*(1–2), 3–40. https://doi.org/10.1016/S0169-7439(98)00065-3

Ma, Z., Whitley, R. D., & Wang, N. H. L. (1996). Pore and surface diffusion in multicomponent adsorption and liquid chromatography systems. *AIChE Journal*, *42*(5), 1244–1262. https://doi.org/10.1002/aic.690420507

Madivoli, E. S., Kareru, P. G., Makhanu, D. S., Wandera, K. S., Maina, E. G., Wanakai, S. I., & Kimani, P. K. (2020). Synthesis of spherical titanium dioxide microspheres and its application to degrade rifampicin. *Environmental Nanotechnology, Monitoring & Management*, *14*, 100327. https://doi.org/10.1016/J.ENMM.2020.100327

Mahmoud, A. E. D., Franke, M., & Braeutigam, P. (2022). Experimental and modeling of fixed-bed column study for phenolic compounds removal by graphite oxide. *Journal of Water Process Engineering*, *49*, 103085. https://doi.org/https://doi.org/10.1016/j.jwpe.2022.103085

M'Arimi, M. M., Mecha, C. A., Kiprop, A. K., & Ramkat, R. (2020). Recent trends in applications of advanced oxidation processes (AOPs) in bioenergy production: Review. *Renewable and Sustainable Energy Reviews*, *121*, 109669. https://doi.org/10.1016/J.RSER.2019.109669

Maslamani, N., Khan, S. B., Danish, E. Y., Bakhsh, E. M., Zakeeruddin, S. M., & Asiri, A. M. (2021). Carboxymethyl cellulose nanocomposite beads as super-efficient catalyst for the

reduction of organic and inorganic pollutants. *International Journal of Biological Macromolecules*, *167*, 101–116. https://doi.org/10.1016/J.IJBIOMAC.2020.11.074

McBain, James. W. (1909). The mechanism of the adsorption ("sorption") of hydrogen by carbon. *The London, Edinburgh, and Dublin Philosophical Magazine and Journal of Science*, *18*(108), 916–935. https://doi.org/10.1080/14786441208636769

Medha, I., Chandra, S., Bhattacharya, J., Samal, B., & Vanapalli, R. K. (2023). Development of Rice Straw-derived Biochar-Bentonite Composite and its Application for in situ Sequestration of Ammonium and Phosphate Ions in the Degraded Mine Soil. *Environmental Management 2023*, 1–22. https://doi.org/10.1007/s00267-022-01775-9

Megha, R., Ravikiran, Y. T., Kotresh, S., Vijaya Kumari, S. C., Raj Prakash, H. G., & Thomas, S. (2018). Carboxymethyl cellulose: an efficient material in enhancing alternating current conductivity of HCl doped polyaniline. *Cellulose*, *25*(2), 1147–1158. https://doi.org/10.1007/S10570-017-1610-5/TABLES/2

Mehta, D., Mazumdar, S., & Singh, S. K. (2015). Magnetic adsorbents for the treatment of water/wastewater—A review. *Journal of Water Process Engineering*, *7*, 244–265. https://doi.org/10.1016/J.JWPE.2015.07.001

Mitra, M., Kulsi, C., Chatterjee, K., Kargupta, K., Ganguly, S., Banerjee, D., & Goswami, S. (2015). Reduced graphene oxide-polyaniline composites—synthesis, characterization and optimization for thermoelectric applications. *RSC Advances*, *5*(39), 31039–31048. https://doi.org/10.1039/C5RA01794G

Montgomery, D. C. (2019). *Design and Analysis of Experiments* (10th edition). Wiley. https://www.wiley.com/en-us/Design+and+Analysis+of+Experiments%2C+10th+Edition-p-9781119492443

Moraes, S. R., & Motheo, A. J. (2006). PAni-CMC: Preparation, Characterization and Application to Corrosion Protection. *Molecular Crystals and Liquid Crystals*, *448*(1), 261/[863]-267/[869]. https://doi.org/10.1080/15421400500403341

Morin-Crini, N., Lichtfouse, E., Liu, G., Balaram, V., Ribeiro, A. R. L., Lu, Z., Stock, F., Carmona, E., Teixeira, M. R., Picos-Corrales, L. A., Moreno-Piraján, J. C., Giraldo, L., Li, C., Pandey, A., Hocquet, D., Torri, G., & Crini, G. (2022). Worldwide cases of water pollution by emerging contaminants: a review. *Environmental Chemistry Letters 2022 20:4*, *20*(4), 2311–2338. https://doi.org/10.1007/S10311-022-01447-4

Mota, M. L., Carrillo, A., Verdugo, A. J., Olivas, A., Guerrero, J. M., De la Cruz, E. C., & Ramírez, N. N. (2019). Synthesis and Novel Purification Process of PANI and PANI/AgNPs Composite. *Molecules 2019, Vol. 24, Page 1621*, *24*(8), 1621. https://doi.org/10.3390/MOLECULES24081621

Nasar, A., & Mashkoor, F. (2019). Application of polyaniline-based adsorbents for dye removal from water and wastewater—a review. *Environmental Science and Pollution Research 2019 26:6*, *26*(6), 5333–5356. https://doi.org/10.1007/S11356-018-3990-Y

Nejatbakhsh, S., Aghdasinia, H., Ebrahimi Farshchi, M., Azimi, B., & Karimi, A. (2022). Adsorptive Desulfurization of Liquid Hydrocarbons Utilizing Granular Cu/Cr-BDC@γ-Al2O3Bimetal-Organic Frameworks. *Industrial and Engineering Chemistry Research*, *61*(32), 11617–11627. https://doi.org/10.1021/ACS.IECR.2C01491/SUPPL_FILE/IE2C01491_SI_001.PDF

Nguyen, N. T. T., Nguyen, L. M., Nguyen, T. T. T., Liew, R. K., Nguyen, D. T. C., & Tran, T. Van. (2022). Recent advances on botanical biosynthesis of nanoparticles for catalytic, water treatment and agricultural applications: A review. *Science of The Total Environment*, *827*, 154160. https://doi.org/10.1016/J.SCITOTENV.2022.154160

Nijhawan, A., Butler, E. C., & Sabatini, D. A. (2020). Fluoride Adsorption on Porous Hydroxyapatite Ceramic Filters: A Study of Kinetics. *Environmental Engineering Science*, *37*(6), 409–416. https://doi.org/10.1089/ees.2019.0392

Olad, A., Bastanian, M., Aber, S., & Zebhi, H. (2021). Ion-crosslinked carboxymethyl cellulose/polyaniline bio-conducting interpenetrated polymer network: preparation, characterization and application for an efficient removal of Cr(VI) from aqueous solution. *Iranian Polymer Journal (English Edition)*, *30*(2), 105–119. https://doi.org/10.1007/S13726-020-00877-7/FIGURES/8

Osborne, J. (2019). Improving your data transformations: Applying the Box-Cox transformation. *Practical Assessment, Research, and Evaluation*, *15*(12), 1–9. https://doi.org/https://doi.org/10.7275/qbpc-gk17

Ouis, D., el Kebir, A., Moulefera, I., Sabantina, L., & Abdelghani, B. (2022). Synthesis, Characterization and Adsorption of Bisphenol A Using Novel Hybrid Materiel Produced from PANI Matrix Reinforced by Kieselguhr. *Journal of Inorganic and Organometallic Polymers and Materials*, *32*(3), 1092–1102. https://doi.org/10.1007/S10904-021-02151-6/TABLES/6

Oyekanmi, A. A., Alshammari, M. B., Mohamad Ibrahim, M. N., Hanafiah, M. M., Elnaggar, A. Y., Ahmad, A., Oyediran, A. T., Rosli, M. A., Setapar, S. H. M., Daud, N. N. N., & Hussein, E. E. (2021). Highly Effective Cow Bone Based Biocomposite for the Sequestration of Organic Pollutant Parameter from Palm Oil Mill Effluent in a Fixed Bed Column Adsorption System. *Polymers 2022*, *14*(1), 86. https://doi.org/10.3390/polym14010086

Pap, S., Kirk, C., Bremner, B., Turk Sekulic, M., Shearer, L., Gibb, S. W., & Taggart, M. A. (2020). Low-cost chitosan-calcite adsorbent development for potential phosphate removal and recovery from wastewater effluent. *Water Research*, *173*, 115573. https://doi.org/10.1016/j.watres.2020.115573

Park, J. M., & Jhung, S. H. (2021). Remarkable adsorbent for removal of bisphenol A and S from water: Porous carbon derived from melamine/polyaniline. *Chemosphere*, *268*, 129342. https://doi.org/10.1016/J.CHEMOSPHERE.2020.129342

Parris, K. (2011). Impact of Agriculture on Water Pollution in OECD Countries: Recent Trends and Future Prospects. *Https://Doi.Org/10.1080/07900627.2010.531898*, *27*(1), 33–52. https://doi.org/10.1080/07900627.2010.531898

Patel, H. (2019). Fixed-bed column adsorption study: a comprehensive review. *Applied Water Science 2019 9:3*, *9*(3), 1–17. https://doi.org/10.1007/S13201-019-0927-7

Patel, H., & In, C. (2021). Comparison of batch and fixed bed column adsorption: a critical review. *International Journal of Environmental Science and Technology 2021 19:10*, *19*(10), 10409–10426. https://doi.org/10.1007/s13762-021-03492-y

Peng, H., Ma, G., Ying, W., Wang, A., Huang, H., & Lei, Z. (2012). In situ synthesis of polyaniline/sodium carboxymethyl cellulose nanorods for high-performance redox supercapacitors. *Journal of Power Sources*, *211*, 40–45. https://doi.org/10.1016/j.jpowsour.2012.03.074

Pérez-Calderón, J., Santos, M. V., & Zaritzky, N. (2023). Experimental study and modelling of an azo colorant dynamic adsorption onto functional cross-linked chitosan/ ceramic particles in a fixed bed column. *The Canadian Journal of Chemical Engineering*. https://doi.org/10.1002/cjce.24852

Pesqueira, J. F. J. R., Pereira, M. F. R., & Silva, A. M. T. (2020). Environmental impact assessment of advanced urban wastewater treatment technologies for the removal of

priority substances and contaminants of emerging concern: A review. *Journal of Cleaner Production*, *261*, 121078. https://doi.org/10.1016/J.JCLEPRO.2020.121078

Petrie, B., Barden, R., & Kasprzyk-Hordern, B. (2015). A review on emerging contaminants in wastewaters and the environment: Current knowledge, understudied areas and recommendations for future monitoring. *Water Research*, *72*, 3–27. https://doi.org/10.1016/J.WATRES.2014.08.053

Plattard, N., Dupuis, A., Migeot, V., Haddad, S., & Venisse, N. (2021). An overview of the literature on emerging pollutants: Chlorinated derivatives of Bisphenol A (ClxBPA). *Environment International*, *153*, 106547. https://doi.org/10.1016/J.ENVINT.2021.106547

Qian, Y., Zhang, F., & Pang, H. (2021). A Review of MOFs and Their Composites-Based Photocatalysts: Synthesis and Applications. *Advanced Functional Materials*, *31*(37), 2104231. https://doi.org/10.1002/ADFM.202104231

Qili, H. (2019). *Modifications of Breakthrough Models for Fixed-bed Column and Insights into Physical Meanings of Corresponding Parameters* [PhD]. University of Tsukuba.

Qin, Y., Zhou, C., Yu, S., Pang, H., Guo, J., Wei, J., Wang, L., Xing, Y., An, Y., & Zhou, Z. (2023). Optimization of a compact on-site stormwater runoff treatment system: Process performance and reactor design. *Chemosphere*, *315*, 137767. https://doi.org/10.1016/j.chemosphere.2023.137767

Qiu, H., Lv, L., Pan, B. C., Zhang, Q. J., Zhang, W. M., & Zhang, Q. X. (2009). Critical review in adsorption kinetic models. *Journal of Zhejiang University: Science A*, *10*(5), 716–724. https://doi.org/10.1631/JZUS.A0820524/METRICS

Rasmussen, S. C. (2018). Early history of conductive organic polymers. In *Conductive Polymers* (1st ed., pp. 1–22). CRC Press. https://doi.org/10.1201/9781315119007-1

Rathi, B. S., & Kumar, P. S. (2021). Application of adsorption process for effective removal of emerging contaminants from water and wastewater. *Environmental Pollution*, *280*, 116995. https://doi.org/10.1016/J.ENVPOL.2021.116995

Richardson, S. D. (2010). Environmental mass spectrometry: Emerging contaminants and current issues. *Analytical Chemistry*, *82*(12), 4742–4774. https://doi.org/10.1021/AC101102D/ASSET/AC101102D.FP.PNG_V03

Rizzo, L., Malato, S., Antakyali, D., Beretsou, V. G., Đolić, M. B., Gernjak, W., Heath, E., Ivancev-Tumbas, I., Karaolia, P., Lado Ribeiro, A. R., Mascolo, G., McArdell, C. S., Schaar, H., Silva, A. M. T., & Fatta-Kassinos, D. (2019). Consolidated vs new advanced treatment methods for the removal of contaminants of emerging concern from urban wastewater. *Science of The Total Environment*, *655*, 986–1008. https://doi.org/10.1016/J.SCITOTENV.2018.11.265

Rodriguez-Narvaez, O. M., Peralta-Hernandez, J. M., Goonetilleke, A., & Bandala, E. R. (2017). Treatment technologies for emerging contaminants in water: A review. *Chemical Engineering Journal*, *323*, 361–380. https://doi.org/10.1016/J.CEJ.2017.04.106

Rout, P. R., Zhang, T. C., Bhunia, P., & Surampalli, R. Y. (2021). Treatment technologies for emerging contaminants in wastewater treatment plants: A review. *Science of The Total Environment*, *753*, 141990. https://doi.org/10.1016/J.SCITOTENV.2020.141990

Rovani, S., Santos, J. J., Guilhen, S. N., Corio, P., & Fungaro, D. A. (2020). Fast, efficient and clean adsorption of bisphenol-A using renewable mesoporous silica nanoparticles from sugarcane waste ash. *RSC Advances*, *10*(46), 27706–27712. https://doi.org/10.1039/D0RA05198E

Roveri, V., Guimarães, L. L., Toma, W., & Correia, A. T. (2022). Occurrence, ecological risk assessment and prioritization of pharmaceuticals and abuse drugs in estuarine waters along the São Paulo coast, Brazil. *Environmental Science and Pollution Research*, *29*(59), 89712–89726. https://doi.org/10.1007/S11356-022-21945-W/TABLES/4

Saatci, A. M., & Oulman, C. S. (1980). The Bed Depth Service Time Design Method for Deep Bed Filtration. *Journal - American Water Works Association*, *72*(9), 524–528. https://doi.org/10.1002/j.1551-8833.1980.tb04571.x

Sachs, J. D., Schmidt-Traub, G., Mazzucato, M., Messner, D., Nakicenovic, N., & Rockström, J. (2019). Six Transformations to achieve the Sustainable Development Goals. *Nature Sustainability 2019 2:9*, *2*(9), 805–814. https://doi.org/10.1038/s41893-019-0352-9

Salgado, R., Pereira, V. J., Carvalho, G., Soeiro, R., Gaffney, V., Almeida, C., Cardoso, V. V., Ferreira, E., Benoliel, M. J., Ternes, T. A., Oehmen, A., Reis, M. A. M., & Noronha, J. P. (2013). Photodegradation kinetics and transformation products of ketoprofen, diclofenac and atenolol in pure water and treated wastewater. *Journal of Hazardous Materials*, *244–245*, 516–527. https://doi.org/10.1016/J.JHAZMAT.2012.10.039

Sallmann, A. R. (1986). The history of diclofenac. *The American Journal of Medicine*, *80*(4), 29–33. https://doi.org/10.1016/0002-9343(86)90076-8

Samadi, A., Xie, M., Li, J., Shon, H., Zheng, C., & Zhao, S. (2021a). Polyaniline-based adsorbents for aqueous pollutants removal: A review. *Chemical Engineering Journal*, *418*, 129425. https://doi.org/10.1016/J.CEJ.2021.129425

Samadi, A., Xie, M., Li, J., Shon, H., Zheng, C., & Zhao, S. (2021b). Polyaniline-based adsorbents for aqueous pollutants removal: A review. *Chemical Engineering Journal*, *418*, 129425. https://doi.org/10.1016/J.CEJ.2021.129425

Samadi, A., Xie, M., Li, J., Shon, H., Zheng, C., & Zhao, S. (2021c). Polyaniline-based adsorbents for aqueous pollutants removal: A review. *Chemical Engineering Journal*, *418*, 129425. https://doi.org/10.1016/j.cej.2021.129425

Sambaza, S. S., Maity, A., & Pillay, K. (2020). Polyaniline-coated TiO2 nanorods for photocatalytic degradation of bisphenol A in water. *ACS Omega*, *5*(46), 29642–29656. https://doi.org/10.1021/ACSOMEGA.0C00628/ASSET/IMAGES/ACSOMEGA.0C00628.SOCIAL.JPEG_V03

Sani, N. A. A., Lau, W. J., & Ismail, A. F. (2015). Polyphenylsulfone-based solvent resistant nanofiltration (SRNF) membrane incorporated with copper-1,3,5-benzenetricarboxylate (Cu-BTC) nanoparticles for methanol separation. *RSC Advances*, *5*(17), 13000–13010. https://doi.org/10.1039/C4RA14284E

Sanusi, I. O., Olutona, G. O., Wawata, I. G., & Onohuean, H. (2023). Occurrence, environmental impact and fate of pharmaceuticals in groundwater and surface water: a critical review. *Environmental Science and Pollution Research 2023 30:39*, *30*(39), 90595–90614. https://doi.org/10.1007/S11356-023-28802-4

Saquib, S., Yadav, A. K., & Prajapati, K. B. (2021). Emerging pollutants in water and human health. In *Contamination of Water: Health Risk Assessment and Treatment Strategies* (pp. 285–299). Academic Press. https://doi.org/10.1016/B978-0-12-824058-8.00008-6

SAS Institute Inc. (2017). *JMP® 13 Design of Experiments Guide* (2nd edition).

Schideman, L. C., Mariñas, B. J., Snoeyink, V. L., & Campos, C. (2006). Three-Component Competitive Adsorption Model for Fixed-Bed and Moving-Bed Granular Activated Carbon Adsorbers. Part I. Model Development. *Environmental Science and Technology*, *40*(21), 6805–6811. https://doi.org/10.1021/ES060590M

Schwarz, G. (1978). “Estimating the Dimension of a Model.” *The Annals of Statistics*, *6*(2), 461–464. https://doi.org/10.1214/aos/1176344136

Sethi, S., Kaith, B. S., Kaur, M., Sharma, N., & Khullar, S. (2020). A hydrogel based on dialdehyde carboxymethyl cellulose–gelatin and its utilization as a bio adsorbent. *Journal of Chemical Sciences*, *132*(1), 1–16. https://doi.org/10.1007/S12039-019-1700-z

Shete, M., Kumar, P., Bachman, J. E., Ma, X., Smith, Z. P., Xu, W., Mkhoyan, K. A., Long, J. R., & Tsapatsis, M. (2018). On the direct synthesis of Cu(BDC) MOF nanosheets and their performance in mixed matrix membranes. *Journal of Membrane Science*, *549*, 312–320. https://doi.org/10.1016/J.MEMSCI.2017.12.002

Shields, V., Robshaw, T. J., Porter, C. P., Amphlett, J., Hides, A., Bruce, R., Cordiner, J., & Ogden, M. D. (2022). Gold Recovery from Simulant Mine Tailings Using Chelating Ion Exchange Resins with Thiosulfate-Thiourea Lixiviant. *Available at SSRN*. https://doi.org/10.2139/ssrn.4116256

Singh, H., Raj, S., Rathour, R. K. S., & Bhattacharya, J. (2022). Bimetallic Fe/Al-MOF for the adsorptive removal of multiple dyes: optimization and modeling of batch and hybrid adsorbent-river sand column study and its application in textile industry wastewater. *Environmental Science and Pollution Research*, *29*(37), 56249–56264. https://doi.org/10.1007/s11356-022-19686-x

Singh, N. B., Nagpal, G., Agrawal, S., & Rachna. (2018). Water purification by using Adsorbents: A Review. *Environmental Technology & Innovation*, *11*, 187–240. https://doi.org/10.1016/J.ETI.2018.05.006

Smith, K., Zhang, X., & Hofmann, R. (2012). Assessment of alternate characterization tests for prediction of taste and odour control by granular activated carbon. *Water Supply*, *12*(4), 531–539. https://doi.org/10.2166/ws.2012.026

Song, P., Natale, G., Wang, J., Bond, T., Hejazi, H., de la Hoz Siegler, H., Gates, I., Lu, Q., Song, P., Natale, G., Wang, J., Hejazi, H., Siegler, H. H., Gates, I., Lu, Q., & Bond, T. (2019). 2D and 3D Metal–Organic Framework at the Oil/Water Interface: A Case Study of Copper Benzenedicarboxylate. *Advanced Materials Interfaces*, *6*(2), 1801139. https://doi.org/10.1002/ADMI.201801139

Sophia A., C., & Lima, E. C. (2018). Removal of emerging contaminants from the environment by adsorption. *Ecotoxicology and Environmental Safety*, *150*, 1–17. https://doi.org/10.1016/J.ECOENV.2017.12.026

Stejskal, J., Kratochvíl, P., & Radhakrishnan, N. (1993). Polyaniline dispersions 2. UV-Vis absorption spectra. *Synthetic Metals*, *61*(3), 225–231. https://doi.org/10.1016/0379-6779(93)91266-5

Straub, J. O., Hoffmann-, F., & Roche, L. (2016). Aquatic environmental risk assessment for human use of the old antibiotic sulfamethoxazole in Europe. *Environmental Toxicology and Chemistry*, *35*(4), 767–779. https://doi.org/10.1002/ETC.2945

Sullivan, G. M., & Feinn, R. (2012). Using Effect Size—or Why the P Value Is Not Enough. *Journal of Graduate Medical Education*, *4*(3), 279–282. https://doi.org/10.4300/JGME-D-12-00156.1

Szostak, K., Hodacka, G., Długosz, O., Pulit-Prociak, J., & Banach, M. (2022). Sorption of Mercury in Batch and Fixed-Bed Column System on Hydrochar Obtained from Apple Pomace. *Processes 2022*, *10*(10), 2114. https://doi.org/10.3390/pr10102114

Tang, Y., Yin, M., Yang, W., Li, H., Zhong, Y., Mo, L., Liang, Y., Ma, X., & Sun, X. (2019). Emerging pollutants in water environment: Occurrence, monitoring, fate, and risk assessment. *Water Environment Research*, *91*(10), 984–991. https://doi.org/10.1002/WER.1163

Tanwar, S., & Ho, J. A. A. (2015). Green Synthesis of Novel Polyaniline Nanofibers: Application in pH Sensing. *Molecules 2015, Vol. 20, Pages 18585-18596*, *20*(10), 18585–18596. https://doi.org/10.3390/MOLECULES201018585

Taoufik, N., Elmchaouri, A., El Mahmoudi, S., Korili, S. A., & Gil, A. (2021). Comparative analysis study by response surface methodology and artificial neural network on salicylic acid adsorption optimization using activated carbon. *Environmental Nanotechnology, Monitoring & Management*, *15*, 100448. https://doi.org/10.1016/J.ENMM.2021.100448

Tarafdar, A., Sirohi, R., Balakumaran, P. A., Reshmy, R., Madhavan, A., Sindhu, R., Binod, P., Kumar, Y., Kumar, D., & Sim, S. J. (2022). The hazardous threat of Bisphenol A: Toxicity, detection and remediation. *Journal of Hazardous Materials*, *423*, 127097. https://doi.org/10.1016/J.JHAZMAT.2021.127097

Thomas, H. C. (1944). Heterogeneous Ion Exchange in a Flowing System. *Journal of the American Chemical Society*, *66*(10), 1664–1666. https://doi.org/doi.org/10.1021/ja01238a017

Tran, H. D., D'Arcy, J. M., Wang, Y., Beltramo, P. J., Strong, V. A., & Kaner, R. B. (2011). The oxidation of aniline to produce "polyaniline": a process yielding many different nanoscale structures. *Journal of Materials Chemistry*, *21*(11), 3534–3550. https://doi.org/10.1039/C0JM02699A

Trovó, A. G., Nogueira, R. F. P., Agüera, A., Sirtori, C., & Fernández-Alba, A. R. (2009). Photodegradation of sulfamethoxazole in various aqueous media: Persistence, toxicity and photoproducts assessment. *Chemosphere*, *77*(10), 1292–1298. https://doi.org/10.1016/J.CHEMOSPHERE.2009.09.065

Tyssedal, J. (2008). Plackett–Burman Designs. In F. Ruggeri, R. S. Kenett, & F. W. Faltin (Eds.), *Encyclopedia of Statistics in Quality and Reliability*. John Wiley & Sons, Ltd. https://doi.org/10.1002/9780470061572.EQR020

Uy, M., & Telford, J. K. (2009). Optimization by design of experiment techniques. *2009 IEEE Aerospace Conference Proceedings*, 1–10. https://doi.org/10.1109/AERO.2009.4839625

Vieno, N., & Sillanpää, M. (2014). Fate of diclofenac in municipal wastewater treatment plant — A review. *Environment International*, *69*, 28–39. https://doi.org/10.1016/J.ENVINT.2014.03.021

Vijuksungsith, P., Satapanajaru, T., Chokejaroenrat, C., Jarusutthirak, C., Sakulthaew, C., Kambhu, A., Yoo-iam, M., & Boonprasert, R. (2023). Removal and reuse of phosphorus from aquaculture water using activated carbon-based CaO2 nanoparticles. *Environmental Technology & Innovation*, *29*, 102990. https://doi.org/10.1016/j.eti.2022.102990

Waleng, N. J., & Nomngongo, P. N. (2022). Occurrence of pharmaceuticals in the environmental waters: African and Asian perspectives. *Environmental Chemistry and Ecotoxicology*, *4*, 50–66. https://doi.org/10.1016/J.ENCECO.2021.11.002

Wan, M. (1992). Absorption spectra of thin folm of polyaniline. *Journal of Polymer Science Part A: Polymer Chemistry*, *30*(4), 543–549. https://doi.org/10.1038/108311a0

Wang, J., & Chen, H. (2020). Catalytic ozonation for water and wastewater treatment: Recent advances and perspective. *Science of The Total Environment*, *704*, 135249. https://doi.org/10.1016/J.SCITOTENV.2019.135249

Wang, J., Li, M., Feng, Y., Liu, Y., & Liu, J. (2022). Efficient capture of radioactive iodine by Ag-attached silica gel and its kinetics. *Nuclear Materials and Energy*, *33*, 101270. https://doi.org/10.1016/j.nme.2022.101270

Wang, L., Shi, C., Pan, L., Zhang, X., & Zou, J. J. (2020). Rational design, synthesis, adsorption principles and applications of metal oxide adsorbents: a review. *Nanoscale*, *12*(8), 4790–4815. https://doi.org/10.1039/C9NR09274A

Wang, W., Wang, X., Xing, J., Gong, Q., Wang, H., Wang, J., Chen, Z., Ai, Y., & Wang, X. (2019). Multi-heteroatom doped graphene-like carbon nanospheres with 3D inverse opal structure: a promising bisphenol-A remediation material. *Environmental Science: Nano*, *6*(3), 809–819. https://doi.org/10.1039/C8EN01196F

Wang, Z., Han, J. J., Zhang, N., Sun, D. D., & Han, T. (2019). Synthesis of polyaniline/graphene composite and its application in zinc-rechargeable batteries. *Journal of Solid State Electrochemistry*, *23*(12), 3373–3382. https://doi.org/10.1007/S10008-019-04435-x

Weibull, W. (1951). A Statistical Distribution Function of Wide Applicability. *Journal of Applied Mechanics*, *18*(3), 293–297. https://doi.org/10.1115/1.4010337

Wilkinson, J., Hooda, P. S., Barker, J., Barton, S., & Swinden, J. (2017). Occurrence, fate and transformation of emerging contaminants in water: An overarching review of the field. *Environmental Pollution*, *231*, 954–970. https://doi.org/10.1016/J.ENVPOL.2017.08.032

Witten, B., & Reid, E. E. (1950). p-AMINOTETRAPHENYLMETHANE. *Organic Syntheses*, *30*, 5. https://doi.org/10.15227/ORGSYN.030.0005

World Health Organization (WHO), & United Nations Children's Education Fund (UNICEF). (2000). *Global Water Supply and Sanitation Assessment 2000 Report*. World Health Organization.

Wu, Y. J., & Wang, C. Y. (2019). Insight into the Catalytic Effects of Open Metal Sites in Metal-Organic Frameworks on Hydride Dehydrogenation via Nanoconfinement. *ACS Sustainable Chemistry and Engineering*, *7*(19), 16013–16025. https://doi.org/10.1021/ACSSUSCHEMENG.9B02606/SUPPL_FILE/SC9B02606_SI_001.PDF

WWAP (United Nations World Water Assessment Program). (2015). *The United Nations World Water Development Report 2015*. https://unesdoc.unesco.org/ark:/48223/pf0000231823

Xu, C., Feng, Y., Li, H., Yang, Y., Jiang, S., Wu, R., Ma, R., & Xue, Z. (2023). Adsorption of phosphorus from eutrophic seawater using microbial modified attapulgite - cleaner production, remove behavior, mechanism and cost-benefit analysis. *Chemical Engineering Journal*, *458*, 141404. https://doi.org/10.1016/j.cej.2023.141404

Xu, Z., Cai, J. G., & Pan, B. C. (2013). Mathematically modeling fixed-bed adsorption in aqueous systems. *Journal of Zhejiang University: Science A*, *14*(3), 155–176. https://doi.org/10.1631/JZUS.A1300029/FIGURES/5

Yadav, A., Bagotia, N., Sharma, A. K., & Kumar, S. (2021). Simultaneous adsorptive removal of conventional and emerging contaminants in multi-component systems for wastewater remediation: A critical review. *Science of The Total Environment*, *799*, 149500. https://doi.org/10.1016/J.SCITOTENV.2021.149500

Yadav, A., Kumar, H., Sharma, R., & Kumari, R. (2021). Influence of polyaniline on the photocatalytic properties of metal nanocomposites: A review. *Colloid and Interface Science Communications*, *40*, 100339. https://doi.org/10.1016/J.COLCOM.2020.100339

Yamazaki, E., Yamashita, N., Taniyasu, S., Lam, J., Lam, P. K. S., Moon, H. B., Jeong, Y., Kannan, P., Achyuthan, H., Munuswamy, N., & Kannan, K. (2015). Bisphenol A and other bisphenol analogues including BPS and BPF in surface water samples from Japan, China, Korea and India. *Ecotoxicology and Environmental Safety*, *122*, 565–572. https://doi.org/10.1016/J.ECOENV.2015.09.029

Yan, G., Viraraghavan, T., & Chen, M. (2016). A New Model for Heavy Metal Removal in a Biosorption Column. *Adsorption Science & Technology*, *19*(1), 25–43. https://doi.org/10.1260/0263617011493953

Yan, Z., Yang, H., Dong, H., Ma, B., Sun, H., Pan, T., Jiang, R., Zhou, R., Shen, J., Liu, J., & Lu, G. (2018). Occurrence and ecological risk assessment of organic micropollutants in the lower reaches of the Yangtze River, China: A case study of water diversion. *Environmental Pollution*, *239*, 223–232. https://doi.org/10.1016/J.ENVPOL.2018.04.023

Yang, Y., Zhang, X., Jiang, J., Han, J., Li, W., Li, X., Yee Leung, K. M., Snyder, S. A., & Alvarez, P. J. J. (2022). Which Micropollutants in Water Environments Deserve More

Attention Globally? *Environmental Science and Technology*, *56*(1), 13–29. https://doi.org/10.1021/ACS.EST.1C04250/SUPPL_FILE/ES1C04250_SI_002.XLSX

Yates, F., & Fisher, J. B. (1979). The Life of a Scientist. *Journal of the Royal Statistical Society Series A: Statistics in Society*, *142*(4), 504–506. https://doi.org/10.2307/2982557

Yavuz, A. G., Uygun, A., & Bhethanabotla, V. R. (2009). Substituted polyaniline/chitosan composites: Synthesis and characterization. *Carbohydrate Polymers*, *75*(3), 448–453. https://doi.org/10.1016/j.carbpol.2008.08.005

Yeo, K. F. H., Dong, Y., Xue, T., Yang, Y., Chen, Z., Han, L., Zhang, N., Mawignon, F. J., Kolani, K., & Wang, W. (2023). Fixed-bed column method for removing arsenate from groundwater using aluminium-modified kapok fibres. *Journal of Porous Materials*, *1*, 1–12. https://doi.org/10.1007/s10934-022-01420-0

Yoon, Y. H., & Nelson, J. H. (1984). Application of Gas Adsorption Kinetics I. A Theoretical Model for Respirator Cartridge Service Life. *American Industrial Hygiene Association Journal*, *45*(8), 509–516. https://doi.org/10.1080/15298668491400197

Zaborowska, M., Wyszkowska, J., Borowik, A., & Kucharski, J. (2021). Bisphenol a—a dangerous pollutant distorting the biological properties of soil. *International Journal of Molecular Sciences*, *22*(23), 12753. https://doi.org/10.3390/IJMS222312753/S1

Zare-Akbari, Z., Farhadnejad, H., Furughi-Nia, B., Abedin, S., Yadollahi, M., & Khorsand-Ghayeni, M. (2016). PH-sensitive bionanocomposite hydrogel beads based on carboxymethyl cellulose/ZnO nanoparticle as drug carrier. *International Journal of Biological Macromolecules*, *93*, 1317–1327. https://doi.org/10.1016/J.IJBIOMAC.2016.09.110

Zeeshan, M., Shah, J., Jan, M. R., & Iqbal, M. (2021). Removal of Bisphenol-A from Aqueous Samples Using Graphene Oxide Assimilated Magnetic Silica Polyaniline Composite. *Journal of Inorganic and Organometallic Polymers and Materials*, *31*(5), 2073–2082. https://doi.org/10.1007/S10904-021-01937-Y/TABLES/4

Zhan, G., Fan, L., Zhao, F., Huang, Z., Chen, B., Yang, X., & Zhou, S. feng. (2019). Fabrication of Ultrathin 2D Cu-BDC Nanosheets and the Derived Integrated MOF Nanocomposites. *Advanced Functional Materials*, *29*(9), 1806720. https://doi.org/10.1002/ADFM.201806720

Zhang, Y., Liu, J., Zhang, Y., Liu, J., & Duan, Y. (2017). Facile synthesis of hierarchical nanocomposites of aligned polyaniline nanorods on reduced graphene oxide nanosheets for microwave absorbing materials. *RSC Advances*, *7*(85), 54031–54038. https://doi.org/10.1039/c7ra08794b

Zheng, H., Hou, Y., Li, S., Ma, J., Nan, J., & Li, T. (2022). Recent advances in the application of metal organic frameworks using in advanced oxidation progresses for pollutants degradation. *Chinese Chemical Letters*, *33*(12), 5013–5022. https://doi.org/10.1016/J.CCLET.2022.01.048

Zhou, Q., Wang, Y., Xiao, J., & Fan, H. (2016). Adsorption and removal of bisphenol A, α-naphthol and β-naphthol from aqueous solution by Fe3O4@polyaniline core–shell nanomaterials. *Synthetic Metals*, *212*, 113–122. https://doi.org/10.1016/J.SYNTHMET.2015.12.008

Zhou, Q., Wang, Y., Xiao, J., & Fan, H. (2017). Fabrication and characterisation of magnetic graphene oxide incorporated Fe3O4@polyaniline for the removal of bisphenol A, t-octyl-phenol, and α-naphthol from water. *Scientific Reports 2017 7:1*, *7*(1), 1–11. https://doi.org/10.1038/s41598-017-11831-8

Zimmerman, J. B., Anastas, P. T., Erythropel, H. C., & Leitner, W. (2020). Designing for a green chemistry future. *Science*, *367*(6476), 397–400. https://doi.org/10.1126/SCIENCE.AAY3060/ASSET/8997170C-4499-4F22-A12F-B46943929ED6/ASSETS/GRAPHIC/367_397_F3.JPEG